

(12)

ADA036451

Final Technical Report  
for the Period 6-1-75 to 9-30-76

Materials Sciences Research

Contract Number F44620-75-C-0090

ARPA Order No. 2982

Program Code No. 5D10

DDC  
RECEIVED  
MAR 7 1977  
RLL:VLE

Contractor: Purdue Research Foundation

Sponsored by  
Advanced Research Projects Agency

Principal Investigator: R. J. Schwartz (317)749-2467

Program Managers: P. G. Winchell (317)494-8629 (Task I)  
R. G. Squires (317)749-2489 (Task II)  
R. L. Gunshor (317)493-9488 (Task III)

Effective Date of Contract: 6-1-75

Contract Expiration Date: 9-30-76

Amount of Contract: \$ 225,000

Approved for public release;  
distribution unlimited.

REPORT DOCUMENTATION PAGE		READ INSTRUCTIONS BEFORE COMPLETING FORM
1. REPORT NUMBER AFOSR - TR - 77 - 0095	2. GOVT ACCESSION NO.	3. RECIPIENT'S CATALOG NUMBER
4. TITLE (and Subtitle) MATERIALS SCIENCES RESEARCH,	5. TYPE OF REPORT & PERIOD COVERED 6-1-75 to FINAL 9-30-76	
6. PERFORMING ORG. REPORT NUMBER	8. CONTRACT OR GRANT NUMBER(s) F44620-75-C-0090 New	
7. AUTHOR(s) R. J. Schwartz RJ	10. PROGRAM ELEMENT, PROJECT, TASK AREA & WORK UNIT NUMBERS 61102F ARPA00NE	
9. PERFORMING ORGANIZATION NAME AND ADDRESS Purdue University Dept of Electrical Engineering Lafayette, Indiana 47907	12. REPORT DATE 1976	
11. CONTROLLING OFFICE NAME AND ADDRESS AFOSR/NE Bolling AFB DC 20332	13. NUMBER OF PAGES 160	
14. MONITORING AGENCY NAME & ADDRESS (if different from Controlling Office) Final rept. 1 Jan 75 - 30 Sep 76	15. SECURITY CLASS. (of this report) UNCL	
16. DISTRIBUTION STATEMENT (of this Report) Approved for public release; distribution unlimited.		
17. DISTRIBUTION STATEMENT (of the abstract entered in Block 20, if different from Report) F44620-75-C-0090, WARPA/ORDER-2982		
18. SUPPLEMENTARY NOTES AFOSR/ TR-77-0095		
19. KEY WORDS (Continue on reverse side if necessary and identify by block number)		
20. ABSTRACT (Continue on reverse side if necessary and identify by block number) This final report covers work in three areas. In the area of modulated micro-structures hardened steel, the final result was a sample which had a strength of 270 ksi and a fracture toughness of 60 ksi(in) <sup>1/2</sup> . These properties were obtained with a 50% soft layer and a special 0.28% C alloy (Ni, Co, C, Mo, V). In the area of catalytic properties of surface sites, work is reported on the subjects of CO and NO reactions on chromia supported on silica, hydrocarbon synthesis over bimetallic clusters, characterization of surfaces by ESCA, and electrode reaction studies. The topic of imaging through the use (CONT.)		

DD FORM 1 JAN 73 1473

EDITION OF 1 NOV 65 IS OBSOLETE

UNCLASSIFIED

SECURITY CLASSIFICATION OF THIS PAGE (When Data Entered)

408124

4B



1 - 97 - 111

of surface acoustic waves was addressed by considering three different types of devices: a separate media configuration employing high-resistivity silicon wafer and a lithium niobate substrate, a monolithic device employing the silicon and lithium niobate, and a separate media configuration where the silicon continuum is replaced by a pn diode array. In the course of research on the monolithic devices, a technique was developed for achieving a tremendous enhancement in photon detection sensitivity by using a pulsed bias supply.

Accession for	Write Section	<input checked="" type="checkbox"/>
NTIS	Both Section	<input type="checkbox"/>
Disc		
Unpublished		
Justification		
BY	DISTRIBUTION/AVAILABILITY CODES	
Dist.	ATL, and/or SPECIAL	
		A

## TABLE OF CONTENTS

<u>TASK I</u>	<u>Development of a Modulated-Microstructure Heat Treatable Steel</u>	
Summary . . . . .		2
I. Introduction . . . . .		3
II. The Design Rationale . . . . .		5
III. The Model System . . . . .		12
1. Experimental Details . . . . .		13
2. Experimental Results and Discussion . . . . .		26
3. Conclusions . . . . .		60
IV. The High Strength System . . . . .		64
1. The Alloys and Heat Treatment . . . . .		65
2. Microstructure of the Complexes . . . . .		67
3. Mechanical Properties . . . . .		74
4. Conclusions . . . . .		94
V. Acknowledgements . . . . .		96
VI. References . . . . .		97
<u>TASK II</u>	<u>Catalytic Properties of Surface Sites on Metals and Metal Oxides and Their Characterization by X-Ray Photoelectron Spectroscopy</u>	
Summary . . . . .		99
I. Introduction . . . . .		107
II. Catalytic Studies . . . . .		108
1. Objective . . . . .		108
2. Background and Technical Need . . . . .		109
3. Accomplishments . . . . .		112

4.	Results in the Last Three Months . . . . .	121
5.	References . . . . .	123
II.	Characterization of Surface States by ESCA . . . . .	124
1.	Objective . . . . .	124
2.	Background and Technical Need . . . . .	125
3.	Accomplishments (6/1/75-6/30/76) . . . . .	127
4.	Accomplishments (6/30/76-9/30/76) . . . . .	134
5.	References . . . . .	136
III.	Electrode Reaction Studies: Role of Surface Oxides on Cathode Surfaces . . . . .	137
1.	Summary of Results . . . . .	137
2.	Experimental Approach . . . . .	137
3.	Results . . . . .	138
4.	Recent Results on Electrode Reaction Studies . . . . .	143
5.	Literature Cited . . . . .	144
<u>TASK III ACOUSTIC SURFACE WAVE DEVICES FOR VISIBLE AND INFRARED IMAGING</u>		
	Summary . . . . .	146
	Introduction . . . . .	148
I.	Summary of Performance Characteristics of Surface Acoustic Wave Optical Image Scanning Devices . . . . .	149
1.	Sensitivity . . . . .	149
2.	Resolution . . . . .	150
3.	Spectral Response . . . . .	152
4.	Imaging with Diode Arrays . . . . .	152
II.	Research Program . . . . .	154
1.	Second Harmonic Generation for Optical Imaging . . . . .	154
2.	Convolution Imaging in a ZnO-SiO <sub>2</sub> -Si SAW Device . . . . .	156
3.	The ZnO-SiO <sub>2</sub> -Si Structure, An Electrical Analysis . . . . .	158

4. Growth and Evaluation of Zinc Oxide Films . . . . .	158
5. Optical Image Scanning with a pn Diode Array . . . . .	159



TASK I

DEVELOPMENT OF A MODULATED-  
MICROSTRUCTURE HEAT TREATABLE STEEL

Program Manager: P. G. Winchell (317)494-8629

## SUMMARY

Purpose: To design and develop a modulated microstructure hardened steel consisting of alternating hard and soft layers such that the steel has a strength of 400 ksi (28 GPa) and a fracture toughness of  $150\sqrt{\text{in}}$  ( $150 \text{ GPa}\sqrt{\text{m}}$ ). The complex is to be heat treatable, i.e., it can be softened for machining and hardened for maximum properties.

Conclusions: A special 0.28%C alloy (Ni Co C Mo V) was designed and developed to have the same carbon potential as a high speed tool steel (later selected as M4), which contains 1.35%C. The latter hardened to about 870 KHN while the former hardened to 330 KHN. The complex with the best properties was one with about .50% soft layer. It had a strength of 270 ksi (1.8 GPa) and a fracture toughness of  $60\sqrt{\text{in}}$  ( $65 \text{ GPa}\sqrt{\text{m}}$ ). These are substantially below the design levels and the main problem is in developing sufficient strength in the hard layer. (The hard-layer, high-speed steel originally intended for the project turned out to be too brittle for use.) The toughness probably could be increased somewhat by a further increase in the thickness of the layers. The complex was heat treatable as required, and the achievement of the properties attained was due to the design of an easily parted interface between the soft and hard layers. This interface allowed the ductility of the soft layer to effectively contribute to the fracture toughness of the complex, but it did not stop cracking at the interface effectively enough so that compositions richer than 50% hard layer could achieve high strength.

## I. INTRODUCTION

This project has been the design and development of a heat treatable, modulated microstructure, (laminated) alloy steel complex. The complex was to be machinable and hardenable and was to retain adequate toughness in the hardened condition. Each complex consisted of alternating layers of soft and hard alloy steels. The complexes were manufactured by hot rolling stacks of steel sheets. The design and development of the complexes involved manipulation of such variables as: the compositions and properties of the constituent alloys, the nature of the interface between them, the relative amount of the softer layers and the modulation distance, i.e., the thickness of the soft and hard layers. These variables were adjusted to optimize the strength and fracture toughness of the complex.

The basic concept upon which the complexes were designed is that the alloying of each steel can be adjusted so that soft alloy can be presented for testing as soft unstable austenite or as various austenite-martensite mixtures while the simultaneously heat-treated hard alloy is completely hardened. In the soft layer some of the unstable austenite will transform to martensite during testing and "work harden" the soft layer. The soft layer deformation is designed to impede crack propagation and to contribute to the energy required for a fracture to propagate. Fracture toughness (due to the deformation and strength of the soft layer) and strength (contributed by both the soft and hard layers) are the basic goals of the design.

To implement this design commercial steels were selected for the hard layer and the soft layer was specially produced. The soft layer was adjusted in composition so that it would be presented at room temperature as unstable austenite by the heat treatment required to harden the hard layer.

Subsequent sub-ambient cooling to form some martensite and low-temperature tempering treatments were then used to optimize the soft layer properties without altering the hard layer. A lower carbon level in the soft layer was desirable but the two layers were required to have the same chemical potential of carbon. This latter requirement was instituted so that carbon diffusion would not change the layer compositions during required preliminary heat treatment. By appropriate alloying the  $M_s$  of the soft layer was placed slightly below room temperature and the carbon content of the soft layer was maintained in the medium carbon range.

Two series of complexes were tested. The first involved AISI O1 tool steel (so called nondeforming oil hardening tool steel) as the hard layer. This was matched with a soft layer alloy containing 0.38%C, 25%Ni, and 6%Co. This latter steel is referred to as PS2. The complexes so produced were used as a model of the system to be developed later because the thermochemical treatments were short and results could be obtained fairly rapidly. Following the developmental work on this alloy by Dr. W. Y. C. Chen, as a second series was studied by Dr. Daniel Ng using for a hard layer one of two high-speed tool steels REX 71\* -- a special high carbon, very high hardness steel and AISI M4, which is a similar alloy somewhat lower in hardness. The first of these was matched by alloy PS4, a carbon-nickel-cobalt alloy steel of slightly different composition than the PS2. A change from REX 71 to M4, which compromised the hardness of the hard layer was necessitated by the low observed fracture strengths of the REX 71 layers in complexes tested in tension. The majority of the work reported on the so called high-strength complexes is on the M4/PS4 system.

---

\* Trademark of Crucible Steel Corp.



The design target of 400 ksi (2750 MPa) at a fracture toughness of  $150 \text{ ksi}\sqrt{\text{in}}$  ( $165 \text{ MPa}\sqrt{\text{m}}$ ) was never achieved largely because the REX 71 high hardness layer did not supply a strength corresponding to its indentation hardness. In spite of this failure to obtain the design goals, design rational described below did appear to correlate the results of mechanical property tests on both the 01/PS2 and the M4/PS4 complexes. This rational should provide a basis for some future development of such materials.

## II. THE DESIGN RATIONALE

In this section the variation of fracture toughness and tensile strength with the various design parameters is considered and methods of optimizing toughness at high strength are described. Loading in uniaxial tension along an axis in the plane of the interfaces and the propagation of cracks in a direction normal to the tensile axis and also normal to the interface plane are considered first. Then fracture toughness for a fracture plane perpendicular to both the tensile axis and the interface normal is considered. The first two processes are thought to be essential aspects of tensile strength and the latter is the important fracture toughness in the so-called divider orientation.

According to the law of mixture, the strength ( $\sigma$ ) of the complex is governed by that of the hard ( $\sigma_H$ ) and soft ( $\sigma_S$ ) layers and by the fraction of the soft layer ( $f_S$ ) as follows:

$$\sigma = \sigma_H f_H + \sigma_S f_S \quad (2.1)$$

Since  $f_H + f_S = 1$ , the above equation can be rewritten as

$$\frac{\sigma}{\sigma_H} = (1-f_S) + f_S \frac{\sigma_S}{\sigma_H} \geq 1 - f_S \quad (2.2)$$

With the specimen under tension  $\sigma$ , consider an elliptical crack of

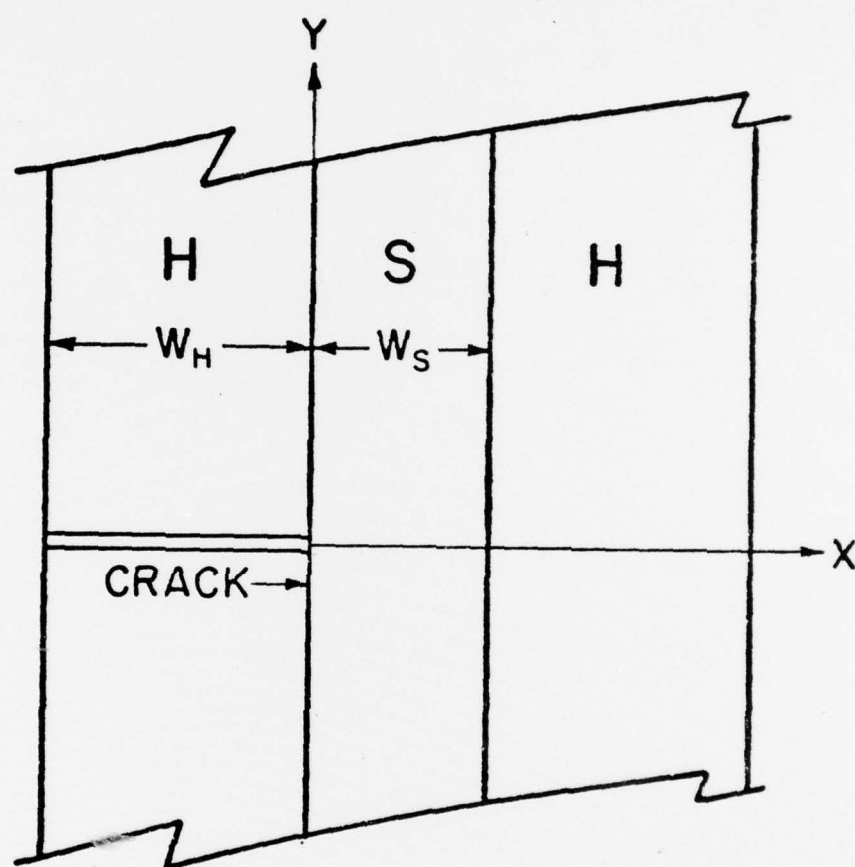


Fig. 1. A Schematic Drawing Showing a Crack Developed Across a Hard Layer.

length  $w_H$  across a hard layer parallel to the modulation direction x-axis. (Fig. 1). The stress  $\sigma_{yy}$  at  $(x,0)$  will be the sum of tension stress and the stress which arises due to the nearby crack<sup>(1)</sup> i.e.,

$$\sigma_{yy} = \sigma + \frac{\sigma \sqrt{w_H}}{\sqrt{4x}} \quad (2.3)$$

If the crack is not permitted to jump across the soft layer to induce fracture on the next hard layer, the stress  $\sigma_{yy}$  at  $(w_S, 0)$  has to be smaller than or equal to the strength of the hard layer ( $\sigma_H$ ), i.e.,

$$\sigma + \frac{\sigma \sqrt{w_H}}{\sqrt{4w_S}} \leq \sigma_H \quad (2.4)$$

using relations  $f_S = w_S/(w_H + w_S)$  and  $1 - f_S = w_H/(w_H + w_S)$ , we have

$$\frac{\sigma}{\sigma_H} \leq \frac{1}{1 + \sqrt{\frac{1-f_S}{4f_S}}} \quad (2.5)$$

Fig. 2 shows the relation of  $\frac{\sigma}{\sigma_H}$  to  $f_S$  for both Equations (2) and (5). The minimum strength available is indicated by the dotted line. As the strength of the soft layer,  $\sigma_S$  increases, the available strength according to the law of mixture increases. The complex of interest must be contained in a region below the stress sufficient for cracks to jump across the soft layer and above the minimum stress expected, i.e., the region with the inward pointing arrows.

In such a complex a maximum fracture toughness is desired. The fracture toughness can be estimated from the adsorption of energy,  $\sigma_S \epsilon_S$ , of the soft layers during the propagation of the crack. Here  $\epsilon_S$  is the fracture strain in the soft layer under plain strain conditions. Let us assume that the soft layer can deform without restraint to a depth of

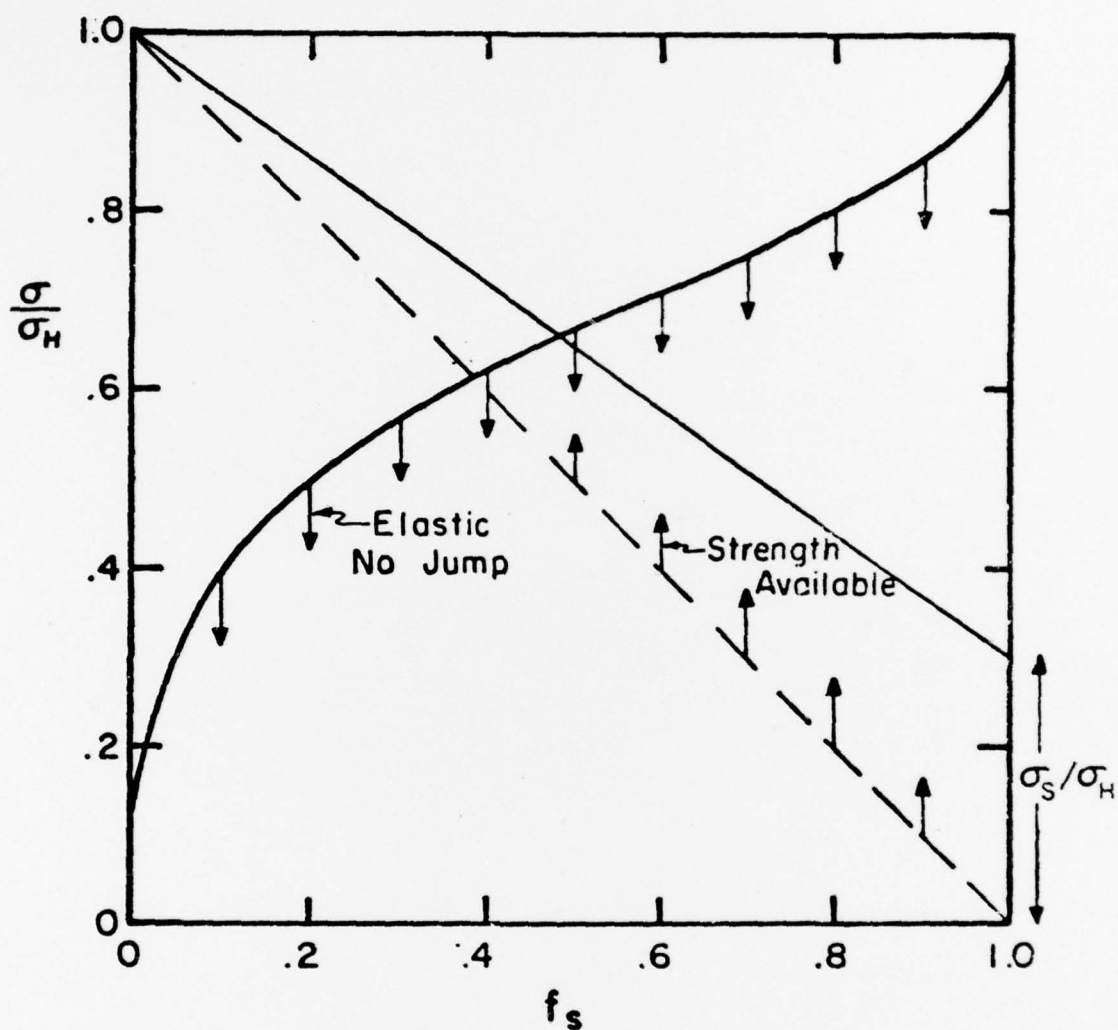


Fig. 2. The Relations of  $\sigma/\sigma_H$  to  $f_s$  for Equations (2) and (5). The alloy complexes of interest are contained in a region below the stress sufficient for cracks to jump across the soft layer and above the minimum stress expected; i.e., the region with the inward pointing arrows.



$\alpha w_s$  ( $\alpha \sim 1$ , see Fig. 3). The amount of work per unit area of fraction of soft layer,  $G_s$  is  $G_s = \sigma_s \epsilon_s \alpha 2 w_s$ . Allowing a small work per unit area of fraction of the hard layer  $G_H$ , for the complex containing independently deforming hard and soft layers,  $G = (1-f_s) G_H + f_s G_s$  or since  $G \frac{E}{1-\nu^2} = K_{IC}^2$  (where  $E$  and  $\nu$  are Young's modulus and Poisson's ratio for both layers)

$$K_{IC}^2 = (1-f_s) K_H^2 + f_s^2 \lambda^2 \alpha \sigma_s \epsilon_s E / (1-\nu^2) \quad (2.6)$$

If the first term on the right hand side can be neglected (or independently evaluated, and submitted for the equation), then  $K_{IC}$  (or  $\sqrt{K_{IC}^2 - (1-f_s) K_H^2}$ ) is seen to be proportional to  $f_s$  and  $\lambda^{1/2}$ . The proportionality to  $\lambda^{1/2}$  is dependent on the constancy of  $\alpha$  with varying  $\lambda$  and is not solidly based. The proportionality constant has  $\sqrt{\sigma_s \epsilon_s}$  as the most important material parameter. The variation of this for several alloy steels has been determined by Clausing (1970) who studied plane strain tensile behavior. His results are recorded in Fig. 4 and they indicate that broad maximum in this parameter may exist at strength levels of about 150 ksi (1000 MPa).

Actual composites obeying the above relations must have soft layers which are easily debonded from their neighbors. The deformation of each soft layer must be associated with debonding at the soft-layer/hard-layer interface. Should this interface be too tightly bonded, a triaxial tensile stress component will develop and the fracture strain in the soft layer will be greatly reduced. One of the considerations in the design and manufacture of all the complexes whose properties are reported below has been the attainment of low interface bonding.

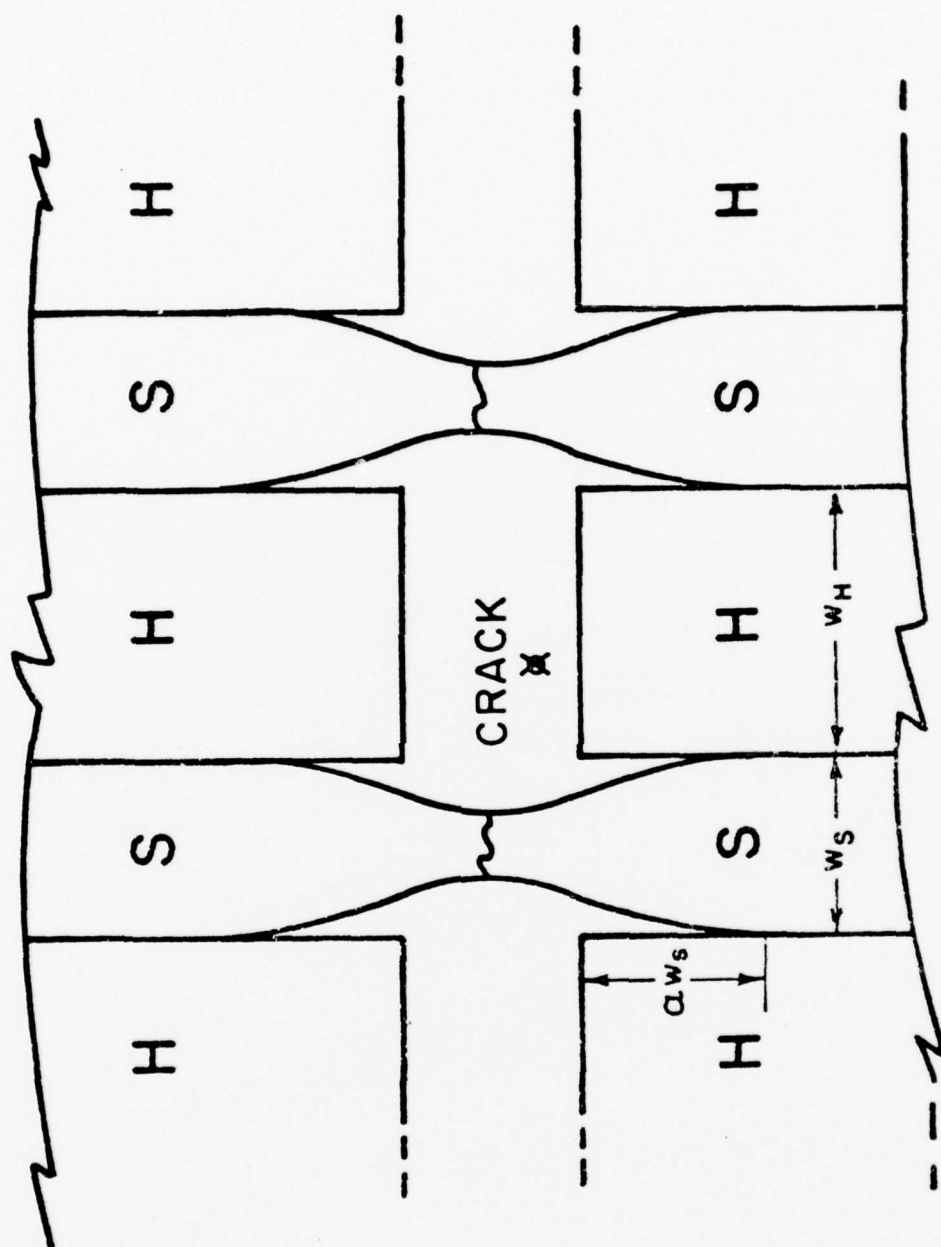
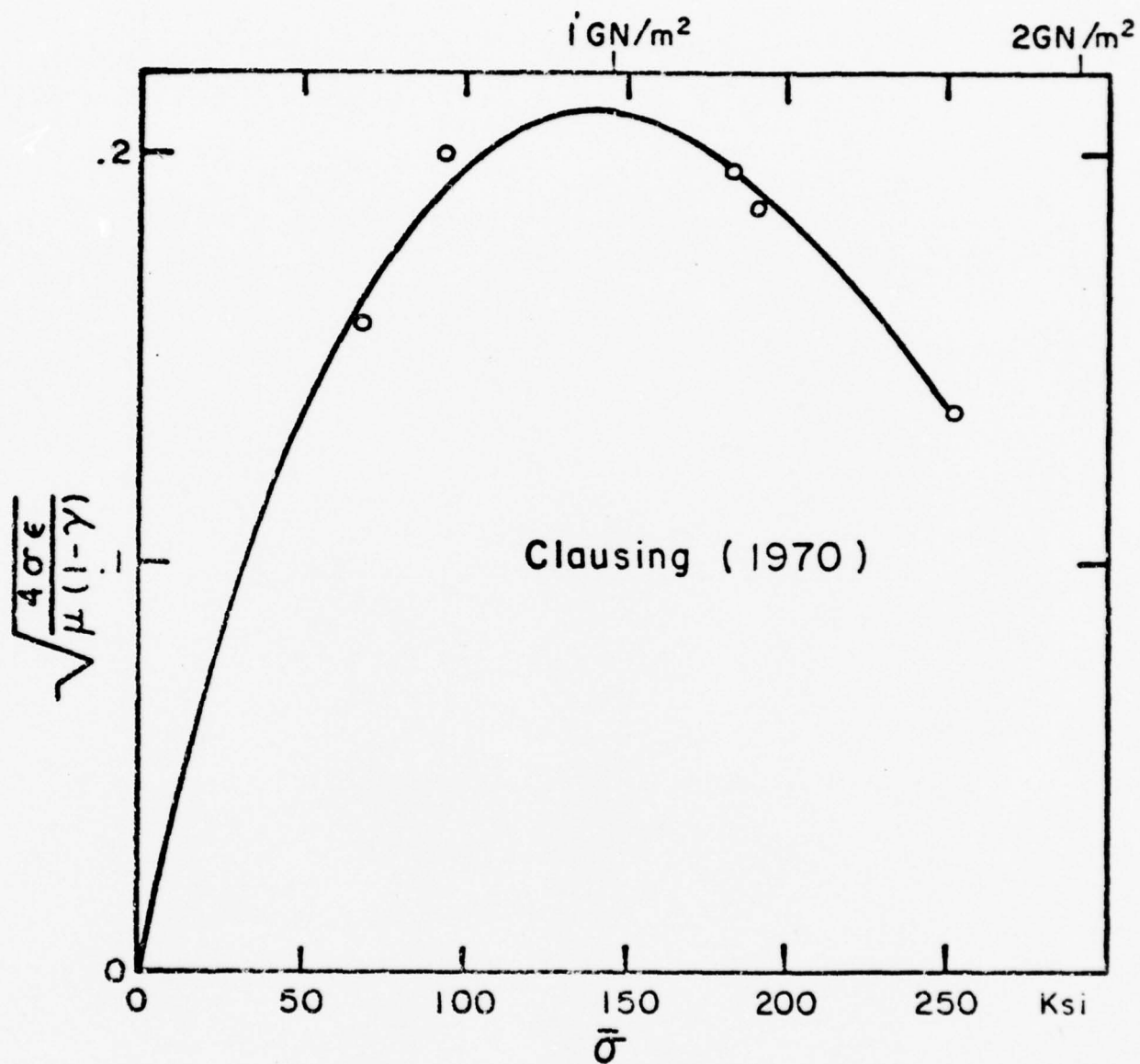


Fig. 3. A Model for Fracture Toughness Calculation.



4.  $\sqrt{\frac{4\sigma\epsilon}{\mu(1-\nu)}}$  as a Function of the Strength of the Soft Layer. Data from Clausing (1970).  $\mu$  is the shear modulus and  $\nu$  is Poisson's ratio.

### III. THE MODEL SYSTEM

In the model system the hard layer is AISI type 01 tool steel because of its low cost, commercial availability, and ease of heat treatment. To match 01 steel, a Purdue soft layer alloy (PS2) was designed based on the following criteria: (a) reasonably high ductility, (b) strength of about 150 ksi (1.0 GN/m<sup>2</sup>), (c) carbon potential equal to that of the hard layer, (d) heat treatment compatible with that of the hard layer. In order to meet these criteria an iron-nickel-cobalt-carbon alloy was selected with  $M_s = 0^\circ\text{C}$ . The composition shown for PS2 in Table I meets these requirements. It is compatible in carbon potential<sup>(3,4)</sup> and heat treatment with 01 steel and it may be subzero quenched to produce martensite at any stage in the treatment. Such subzero quenching has little effect on the 01 steel. The retained austenite can transform during deformation and fracture<sup>(5,6)</sup> to increase fracture toughness.

The compositions for both hard and soft alloy steels are shown in Table I.

TABLE I. COMPOSITION OF MODEL SYSTEM. (wt.%)

Material	Elements							
	C	Mn	Cr	W	V	Ni	Co	Fe
AISI type 01*	.90%	1.20%	.50%	.50%	.20%	0	0	Balance
PS2**	.38%					25.2%	6%	Balance

\* Compositions are nominal

\*\* Compositions are as-charged values. Actual carbon content may be .02% lower.



### 3.1 Experimental Details

#### 3.1.1 Soft Layer Alloy Fabrication.

The Purdue soft layer alloy PS2 was manufactured at the crystal growing facility at Purdue University<sup>(7)</sup>. The metallic elemental charge of the right composition for PS2 alloy was placed in a 99.8% alumina crucible and induction heated in vacuum. After the charge was melted down, a partial pressure of CO was admitted to the system and the carbon was added into melt. The introduction of CO gas was to prevent loss of carbon in reacting with the crucible. When the temperature of the melt was stabilized, the casting followed and the RF power was turned off. The system was pumped out and the fused silica draw tube was lowered into the melt. The system was pressurized with Ar gas while the draw tube was being pumped on to remove any gas that might be generated by the hot metal. The melt was sucked up in the draw tube until it contacted a chill, made of plain carbon steel. Solidification of the alloy was complete in a very short time after the draw; thus, segregation and inhomogeneous microstructure were avoided.

The solid rod product was then cut into pieces of proper sizes and enclosed in preoxidized, sealed stainless steel tubes for hot rolling to the desired sheet thickness. The sheets were removed from their stainless envelopes before further processing.

#### 3.1.2 Manufacturing of Alloy Complexes.

Sheets of 01 steel and PS2 were cut to the proper dimension 1" wide and up to 4" long) and cleaned in an ultrasonic cleaner.

In several complexes the component sheets were preoxidized in air at 600°C for a specified time of 3 hours or less. A sealed stainless steel container was used to prevent oxidation of the sample at high temperature during the rolling process. A schematic drawing in Fig. 5 shows the dimension and configuration of the container and samples. The container consisted of two stainless steel flats (A, F), two pieces of 4-5/8" x 1/4" x 1/4" (B, D) and two pieces of 1" x 1/4" x 1/4" (C, E) stainless steel. The pieces of A, B, C, D, and F were Heliarc welded together (Fig. 5[b]) first. After alternating sheets of hard and soft alloys were inserted in the container, piece E was welded onto it. The interior of the stainless steel container was preoxidized at 950°C for a period of 15 min. so that after rolling the stainless steel would not stick to the sample.

The capsules containing samples were heated to 1150°C prior to rolling. Typical heating time was about 10 min. prior to rolling and typical reduction per pass was 0.1". Fig. 6 shows the approximate heating and rolling program for each sample. After rolling, the stainless steel container was removed by sawing off the edges and forcing a chisel between the sample and the stainless steel.

Every as-rolled sample, was cut to pieces of ~ 4.125" long and ~ 1/2" wide for tensile testing specimens and two 1" x 1/4". Every as-rolled sample was annealed at 675°C for 1 hour and then cut to pieces 4" long and 1" wide for machining to tensile specimen specification (Fig. 7).

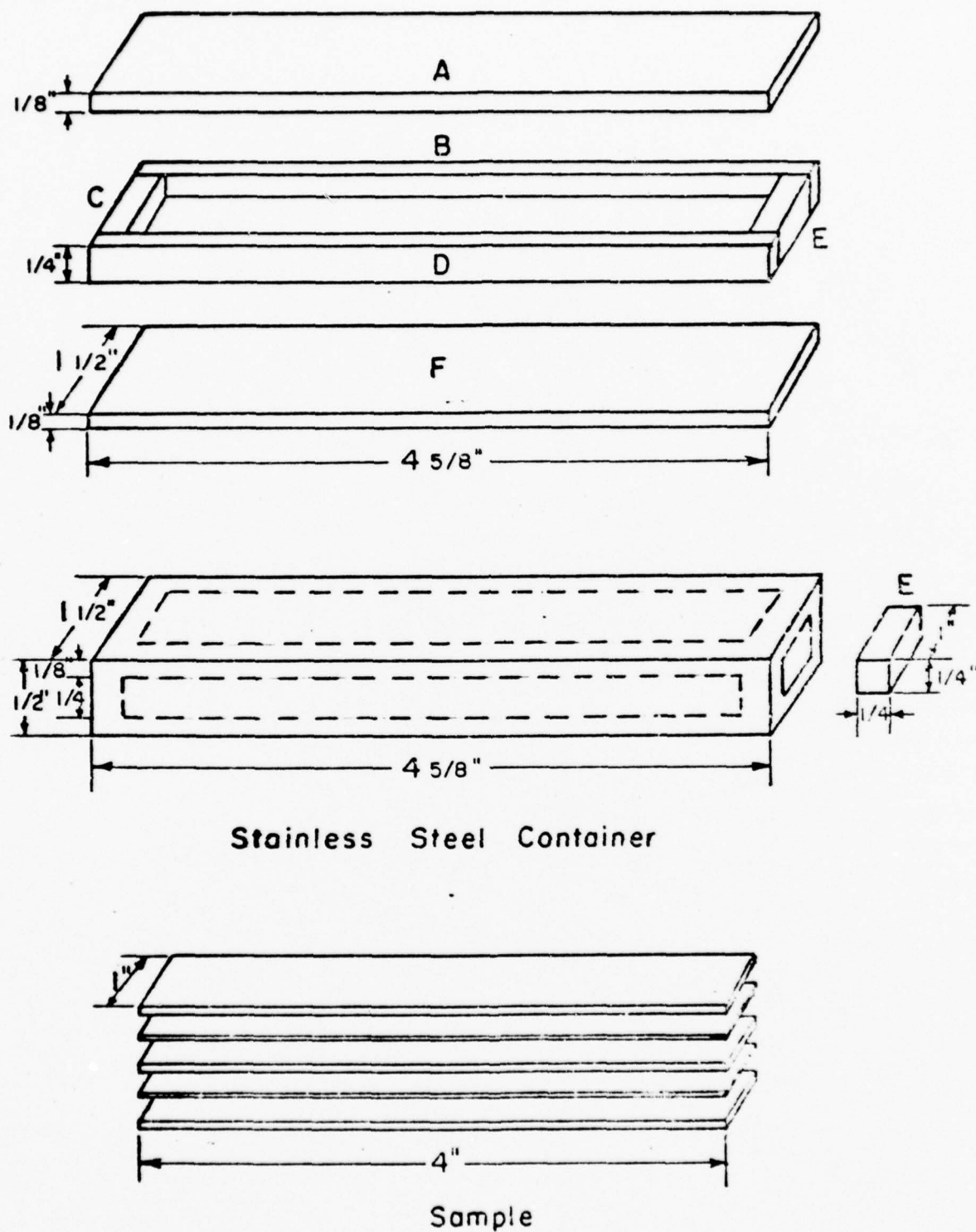


Fig. 5. Stainless Steel Container and Sample Geometry.

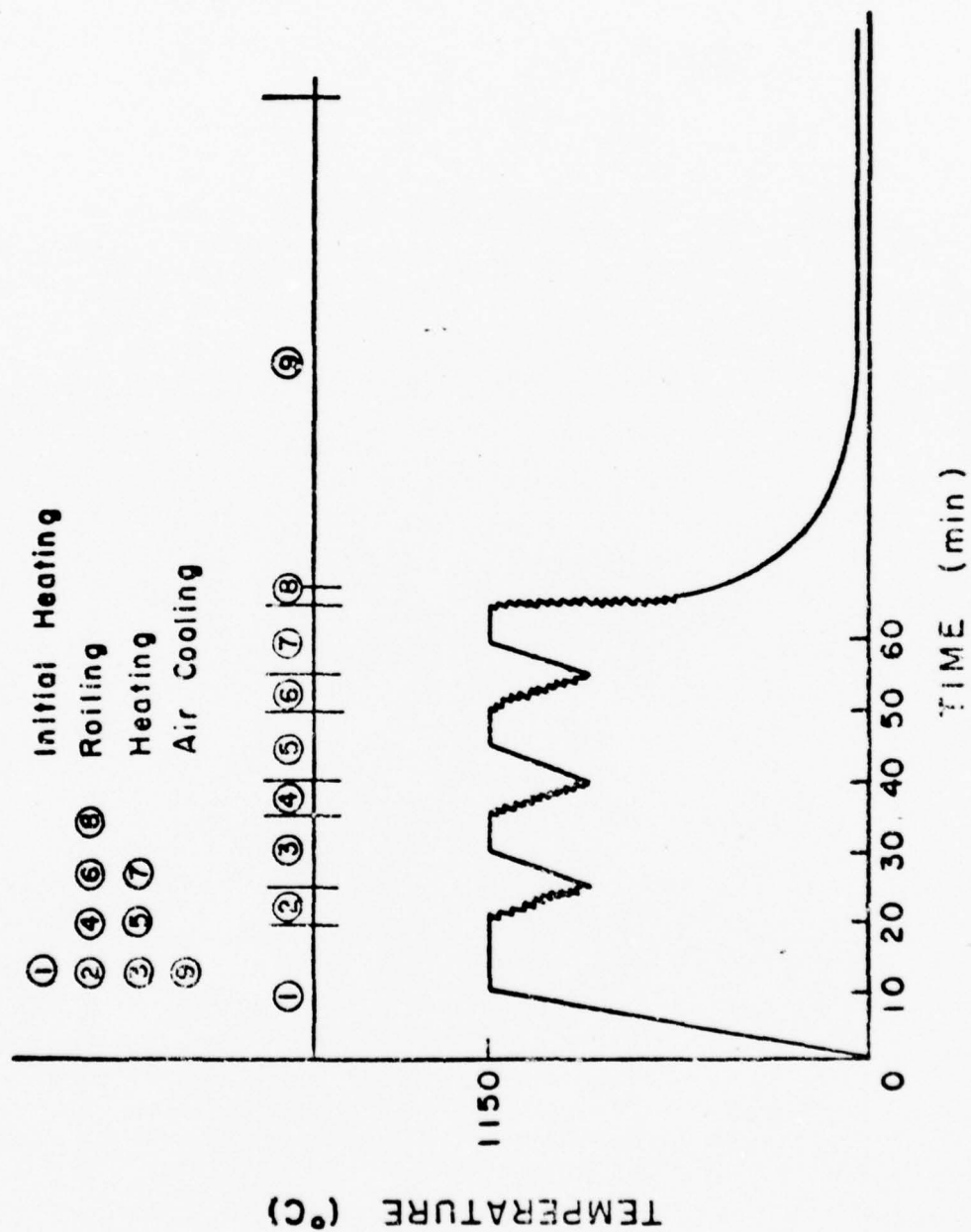


Fig. 6. Heating and Rolling Schedule.

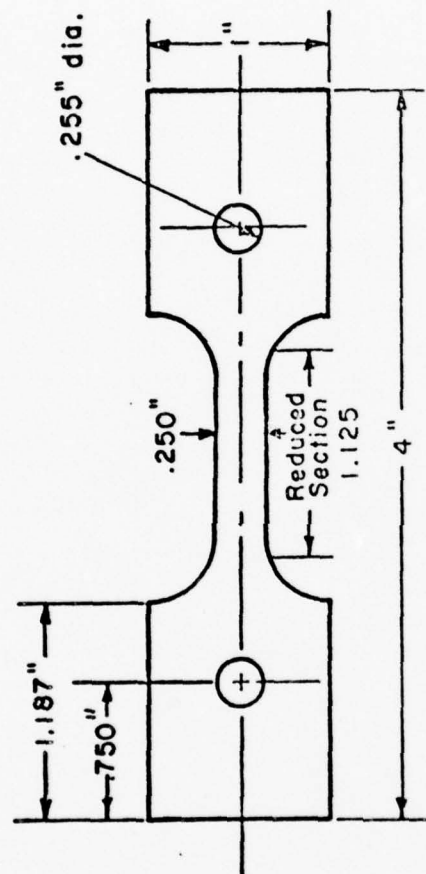


Figure 7. Tensile Specimen Specification. The nominal thickness of specimen is .080" (2.0 mm).



### 3.1.3 Heat Treatment.

Tensile specimen received heat treatments as follows:

- (a) enclosed in a container, heated at 700°C for 20 minutes in a lead pot.
- (b) quenched in oil, then in liquid nitrogen for 30 minutes.
- (c) clamped flat with stainless steel plates, enclosed in a container, heated to 830°C for 1 hour.
- (d) quenched in oil, then in liquid nitrogen for 30 minutes.
- (e) tempered at 200°C for 1 hour.

The reason for the first thermal cycle ((a) & (b)) used in the above procedure was to refine the martensite plate size in the soft layer.

### 3.1.4 Interfacial Bonding Measurement.

There are several methods to characterize interfacial bonding. The method chosen here was similar to the one Gilman<sup>(7)</sup> used to measure the surface energy of various single crystals. In this method a partially split specimen, (Fig. 8), is loaded as a double cantilever beam and the force required to propagate the crack recorded. Knowing the original crack length and the width of the sample, the interfacial bonding energy density,  $\gamma$ , can be calculated according to:

$$\gamma = \frac{6F^2 L^2}{Ew^2 t^3}, \quad (3.1)$$

where  $t$  is the half thickness,  $F$  is the force,  $L$  the crack length,  $w$  the width, and  $E$  is Young's modulus. For the case where the split is not centered,  $\gamma$  can be written as:

$$\gamma = \frac{3F^2 L^2}{E w^2} \left( \frac{1}{t_1^3} + \frac{1}{t_2^3} \right) \quad (3.2)$$

where  $t_1$  and  $t_2$  are thickness of the upper and the lower halves.

For the present tests, special four layer sheets comprised

of alternating hard and soft layers of equal thickness were produced by the standard techniques. A four-layer sheet was prepared using each of the following oxidation treatments: no oxidation, 1/2 hr., 1 hr., 1 1/2 hrs., 2 hrs., 2 1/2 hrs., 3 hrs. at 600°C. Five specimens 1" x 13/16" x .031" were prepared from each sheet. The specimens were heat treated as prescribed in Section 2.4. A hole was cut by electro discharge machining (EDM) as indicated in Fig. 8. By means of a sharp wedge forced against the specimen end, a crack was introduced in the center interface. The crack was propagated until it extended to about half the specimen length. Specimens with irregular cracks were rejected.

The specimens were then tested in an Instron machine by clamping the wires (Fig. 8) in standard friction-type grips. When the crack began to increase in length, the applied force decreased suddenly because of the increased deflection of ends of the specimen. The force at which this happened was recorded as critical force for crack propagation. The crack lengths were measured under the microscope. The interfacial bonding energy was calculated by means of Equation 3.2.

In order to improve the measurement of the interface bonding energy a change was made in the analysis of the test data and in the way the test was conducted, the method used is basically the same as that previously described. The split specimen (Fig. 9) was loaded as a double cantilever beam and the force  $F$ , required to propagate the crack was recorded. Knowing the original crack length  $L$ , and width  $w$  of the sample, the interface bonding energy density  $\gamma$  was calculated.

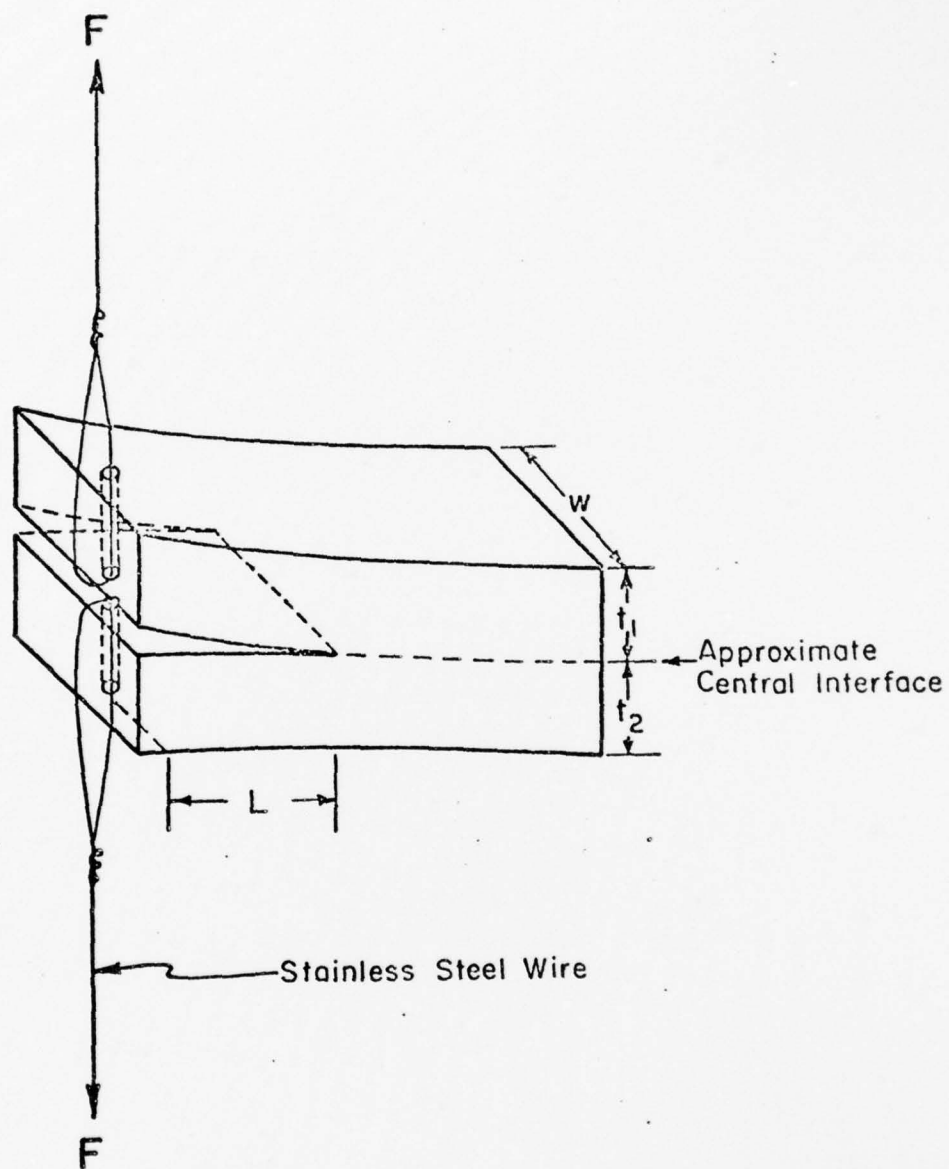


Figure 8. Specimen for Interfacial Bonding Energy Measurement.

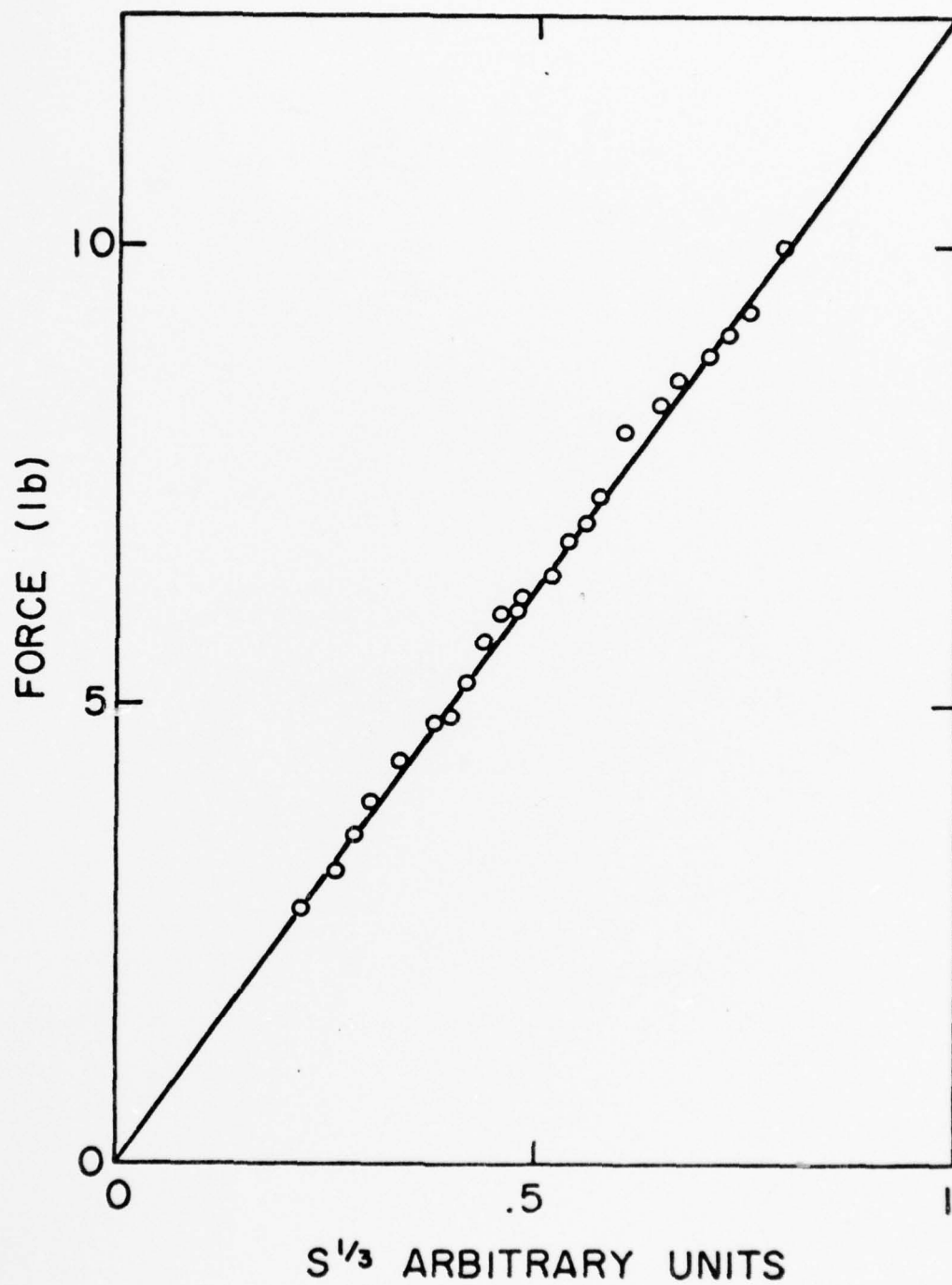


Figure 9. A Typical Plot of  $F$  vs  $S^{1/3}$

Samples were prepared by hot rolling two layers together. In order to eliminate the difficult task of forcing open a starter crack between the layers after the sample was fabricated, a portion of each layer was thinned to substantially less than the rolled half-thickness; this assured the presence of a crack immediately after rolling. The starter crack was then expanded slightly with a wedge into the uniform part of the specimen. The average rolling reduction was determined by measuring the areas enclosed by marker-holes before and after rolling. Specimens of approximately 1/2 in. (12.3mm) x 1 in. (25.4mm) were prepared with a hole drilled using an electric discharge machine. Wires were attached through the drilled hole to the uniform portion of the specimen. The specimens are tested in an Instron machine by clamping wires in the standard friction grips (Fig. 8). When the crack begins to increase in length, the applied force decreases suddenly because of the increased deflection of the ends of the specimen. The force at which this happens was recorded by a strip chart recorder and the crack length measured by a traveling microscope. By measuring different values of  $F$  and  $L$ , an average value of  $\gamma$  can be obtained by using the above equations. However, measurement of  $L$  is inconvenient and was eliminated by means of the equation relating the elastic deflection of the ends of the cantilever beams  $\delta_e$  and elastic force,  $F_e$ , i.e.,  $F_e = \frac{3EI}{L^3} \delta_e$  or in terms of the time derivatives,  $\dot{\delta}_e$  and  $\dot{F}_e$ ,  $L^3 = 3EI \dot{\delta}_e / \dot{F}_e$ , where  $I$  is the areal moment of inertia,  $\dot{\delta}_e$  is the crosshead speed, and



$\dot{F}_e \equiv s$  is the slope of the force time curve which is chart recorded. Thus,

$$\gamma = \left[ \frac{6(3EI\dot{\delta}_e)^{2/3}}{E w^2 t^3} \right] \left( \frac{F}{s^{1/3}} \right)^2. \quad (3.3)$$

As the interface crack propagates along the specimen,  $F$  and  $s$  both decrease and a plot of  $F$  versus  $s^{1/3}$  yields a straight line passing through the origin as shown in Fig. 9. Since all the bracketed terms in the above equation are fixed and known, the slope of this line determines  $\gamma$ .

### 3.1.5 Tensile Test.

The tensile-specimen design (Fig. 8) utilized pin-loading. To hold the tensile specimens, a pair of pin-loaded grips were designed and machined. The performance of these grips and the tensile specimen during testing was satisfactory.

All the tensile specimens were tested at room temperature ( $\sim 22^\circ\text{C}$ ) with an Instron Floor Type machine with maximum capacity of 10,000 lbs. A strain gauge extensometer (Model G-51-16) was used to record strain. The cross-head speed was maintained at .02"/min. at all times so that the strain rate was the same for all specimens. The force and strain were recorded during the test.

### 3.1.6 Microstructure.

Sections of tensile test specimens were mounted and polished. The microstructures were studied with a Leitz optical microscope or a scanning electron microscope if high magnification was needed for fine details.

### 3.1.7 Microhardness Test.

The microhardness as a function of distance in the modulation direction and along the tensile axis was measured with a Knoop indenter and a 400 grams load. This measurement was used as a test of proper quenching of the tensile specimen and to obtain information on the hard and soft layer strength levels in the complex as compared to each single component.

### 3.1.8 Tensile Testing Program.

A systematic program was implemented to investigate the effect of interfacial bonding and fraction soft layer on the tensile properties of the alloy complex. Oxidation treatment of layers at 600°C for 0 hour, 1 hour, 2 hours, and 3 hours were selected. For each treatment four samples were produced at the 0.5 fraction soft layer ( $f_s = .5$ ). Another series of samples received the 2 hours oxidation treatment while fraction of soft layer varied from 0 to 1.0.

For mechanical testing a standard sample was required. Each sample contained eleven layers in total, five hard layers and six soft layers. The outer layers were soft ones which might reduce the possibility of specimen cracking originating at exterior surface flaws. For convenience in mechanical testing as well as to keep materials costs low, the specimen thickness was kept around .080" (2mm), i.e., a wavelength of about .015" (.4mm). All the specimens were to be heat treated and tested at the same condition which will be described in a latter section. Table II gives a summary of all specimens, their oxidation treatment prior to hot-roll welding, and the volu-

TABLE II

Summary of Specimen Identification, Treatment,  
and Volumetric Fraction of Soft Layer.

Fraction Soft Layer fs OXIDATION TREATMENT	0.0		0.25	0.5	0.75	1.00	
	Solid	Laminated	Laminated	Laminated	Laminated	Laminated	Solid
None	D 021			D 111			DP 1
	D 022			D 112			DP 2
	D 023			D 121			DP 3
	D 024			D 122			
1 hr at 600°C							
				D 211			
				D 212			
				D 221			
2 hrs at 600°C				D 222			
			D 331	D 311	D 351	D3P1	
			D 332	D 312	D 352	D3P2	
			D 333	D 321	D 353	D3P3	
3 hrs at 600°C			D 334	D 322	D 354	D3P4	
				D 411			
				D 412			
				D 421			
				D 422			

metric fraction of soft layer for this study.

### 3.2 Experimental Results and Discussion.

#### 3.2.1 Interfacial Bonding Energy Measurement.

The interfacial bonding energies obtained for various oxidation treatments by means of the techniques described in Section 2.5. are shown in Fig. 10. These results are regarded as tentative because the specimens have so few layers and because the measurement technique was under development during their measurement, but the data do show a reduction in bonding with increasing oxidation time. The interfacial bonding energy decreases as oxidation time increases as expected, since increasing of oxidation results in poorer bonding, therefore, requires less energy to propagate cracks.

Using the more precise measuring technique, additional data was obtained. Four samples were made from 01 steels which have been oxidized in air for 2 hours at 600°C (1110°F). They were each rolled twice and after each rolling annealed at 1150°C (2100°F) for ten minutes. The rolling reduction of these samples ranges from about 4% to 40%. Measurements showed that the bonding energy is essentially independent of rolling reduction at about  $5 \times 10^5$  erg/cm<sup>2</sup> (Fig. 11). This is a rather surprising result and we postulate that the bonding energy decreases slowly with increased amount of oxides at the interface and does not vary significantly with increased rolling reduction, and that rolling may well influence the interlamellar bond strength by reducing the oxide particle size and hence reducing the size of the longest initial crack. Further experiments show the bonding energy does

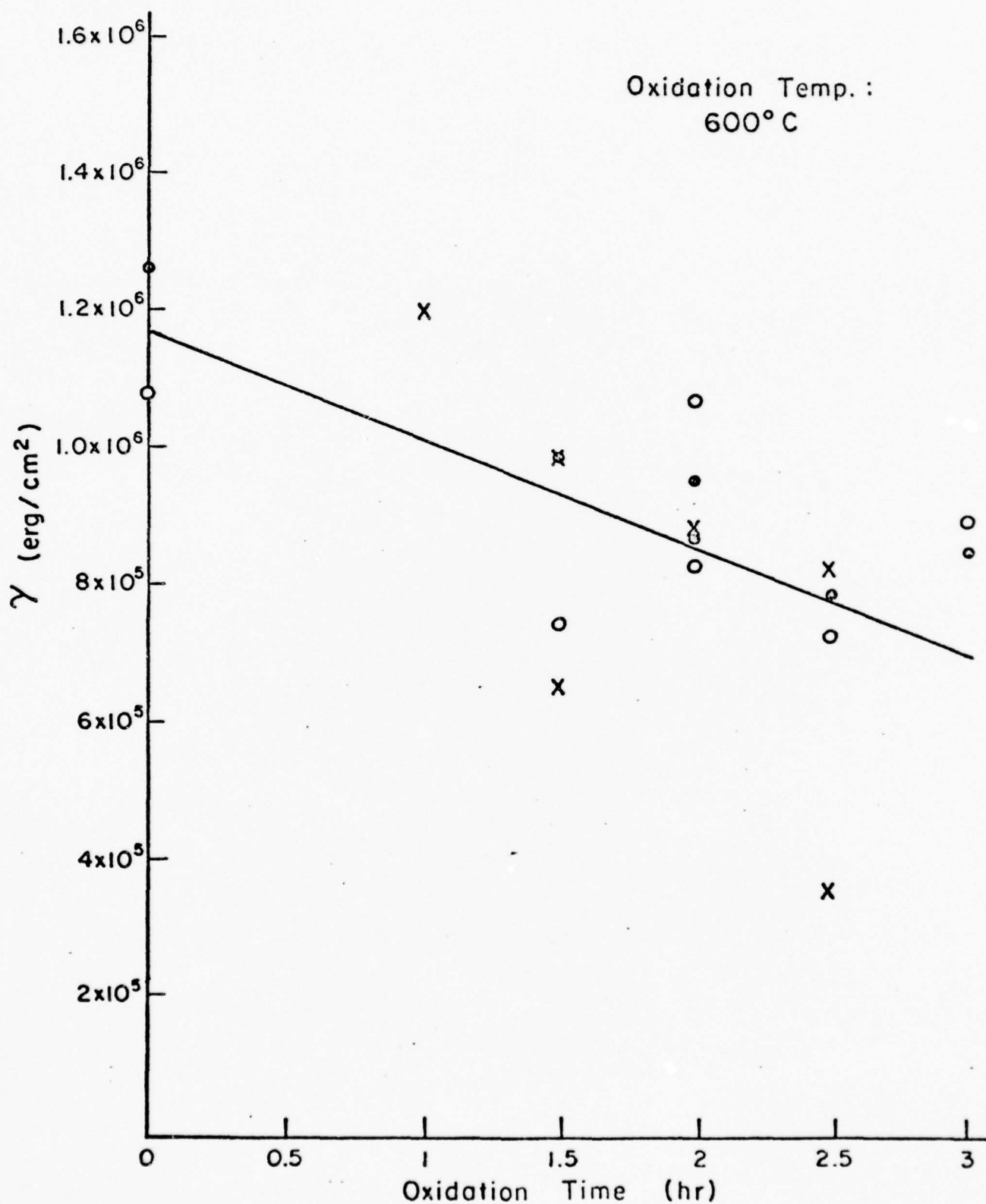


Figure 10. Plot of Interfacial Bonding Energy ( $\gamma$ ) versus Oxidation Time.



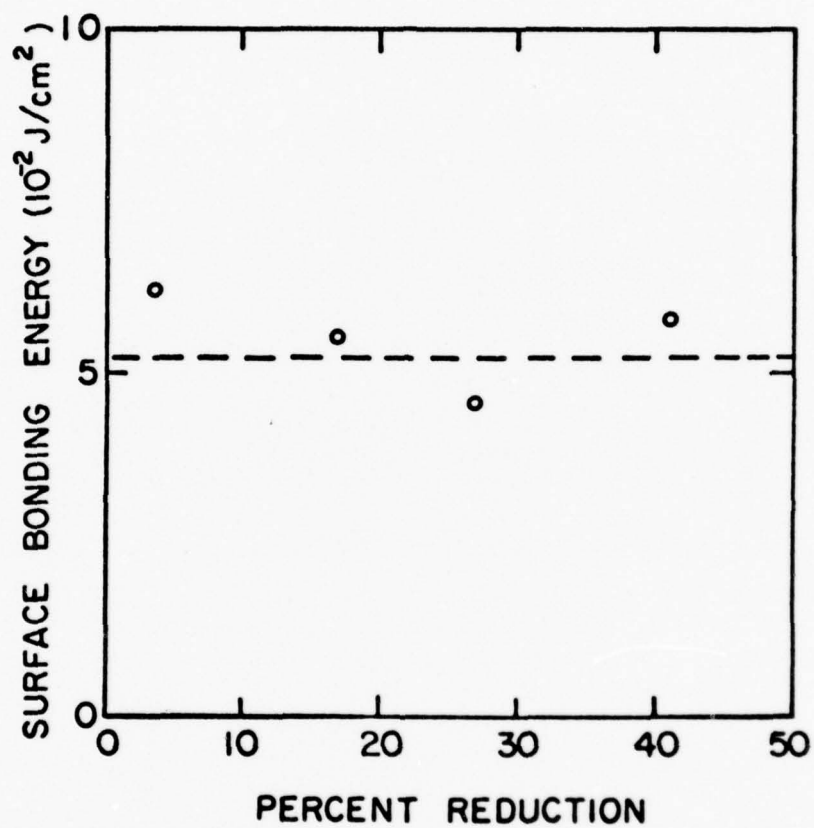


Figure 11. Surface Energy Density of Oxidized 01/01 Interface vs Rolling Reduction

depend on heat treatment temperature and time.

For these experiments, samples were prepared by a fixed hot rolling treatment followed by a ten minute anneal at 1200°C (2200°F) or 1050°C (1900°F) or 870°C (1600°F). The interfacial energy of these samples is shown in Fig. 12. In spite of insignificant differences in rolling reduction, an increase in energy with increasing post-rolling annealing temperature is clear.

A value of  $\gamma = 5 \times 10^5$  erg/cm<sup>2</sup> for the oxidized 01/01 interface implies a value of stress intensity factor of about 15 ksi  $\sqrt{\text{in}}$  for the propagation of a crack along the interface. While large improvement in tensile ductility in the model system is achieved when this kind of interface is substituted for well bonded ones, further reduction in the value of  $\gamma$  is required for the high strength system to be described later.

### 3.2.2 Tensile Test Results.

The tensile test data will be divided into three subsections: (a) the stress-strain ( $\sigma$ - $\epsilon$ ) curves for solid 01 steel and solid soft alloy PS2; (b) the effect of oxidation time of each individual layers prior to hot-roll welding on the tensile properties of alloy complex at the fifty percent of soft layers (i.e.,  $f_s = .50$ ); and (c) the effect of soft layer fraction on the tensile properties of alloy complex at a constant oxidation time of 2 hrs. at 600°C. The data for specimens which failed outside the reduced section were not included except for cases where ductility was very low, i.e.,  $f_s = 0$  and  $f_s = .25$ .

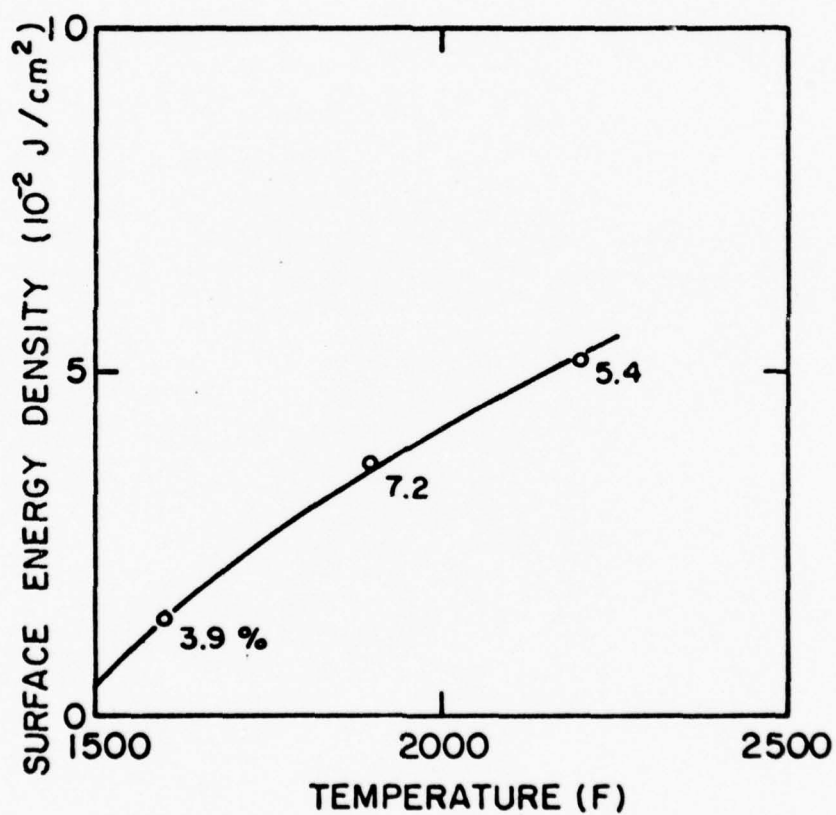


Figure 12. Surface Energy Density of Oxidized 01/01 Interface with 3.9%, 7.2% and 5.4% Rolling Reduction vs Heat Treatment Temperature.

### 3.2.2.1 $\sigma$ - $\epsilon$ Curves for Solid Single Components.

Figure 13 shows the  $\sigma$ - $\epsilon$  characteristics for solid 01 steel and solid Purdue soft alloy PS2. The 01 steel after hardening and light tempering is expected to be of high strength ( $\sim 340$  ksi or  $2.3 \text{ GN/m}^2$ ) and to be brittle and Purdue soft alloy PS2 is expected to be ductile and of lower strength. The measured strength for 01 was around 300 ksi ( $2.1 \text{ GN/m}^2$ ), not far from the expected value, and no plastic strain was observed. The tensile strength for PS2 was around 180 ksi ( $1.2 \text{ GN/m}^2$ ) and the total strain was about 5%. The last figure is lower than one desires to have but it is large enough to have meaningful tests on the alloy complex. Note the stress-strain curves presented here are engineering stress-strain curves. The heavier symbol at the end of each  $\sigma$ - $\epsilon$  curve represents the fracture point.

### 3.2.2.2 The Effect of Oxidation Time (Partial Debonding) on Tensile Properties at Constant Fraction Soft Layer.

The fraction of soft layer was chosen to be .50, i.e., equal amounts of hard layer and soft layer, as suggested by the design rationale. At this constant soft layer fraction, four sets of specimens were prepared: no oxidation of layers prior to hot-roll welding, 1 hr., 2 hrs., and 3 hrs. oxidation at  $600^\circ\text{C}$ .

The  $\sigma$ - $\epsilon$  curves for these four sets of specimens are shown in Figures 14, 15, 16, and 17. The tensile stress ( $\sigma_T$ ), 0.1% yield ( $\sigma_Y$ ), and the plastic strain ( $\epsilon_p$ ) of these specimens as a function of oxidation time are plotted in Fig. 18. The  $\sigma_T$  and  $\sigma_Y$  decrease slowly while the plastic strain increases significantly as oxidation increases. These are expected because as the oxidation

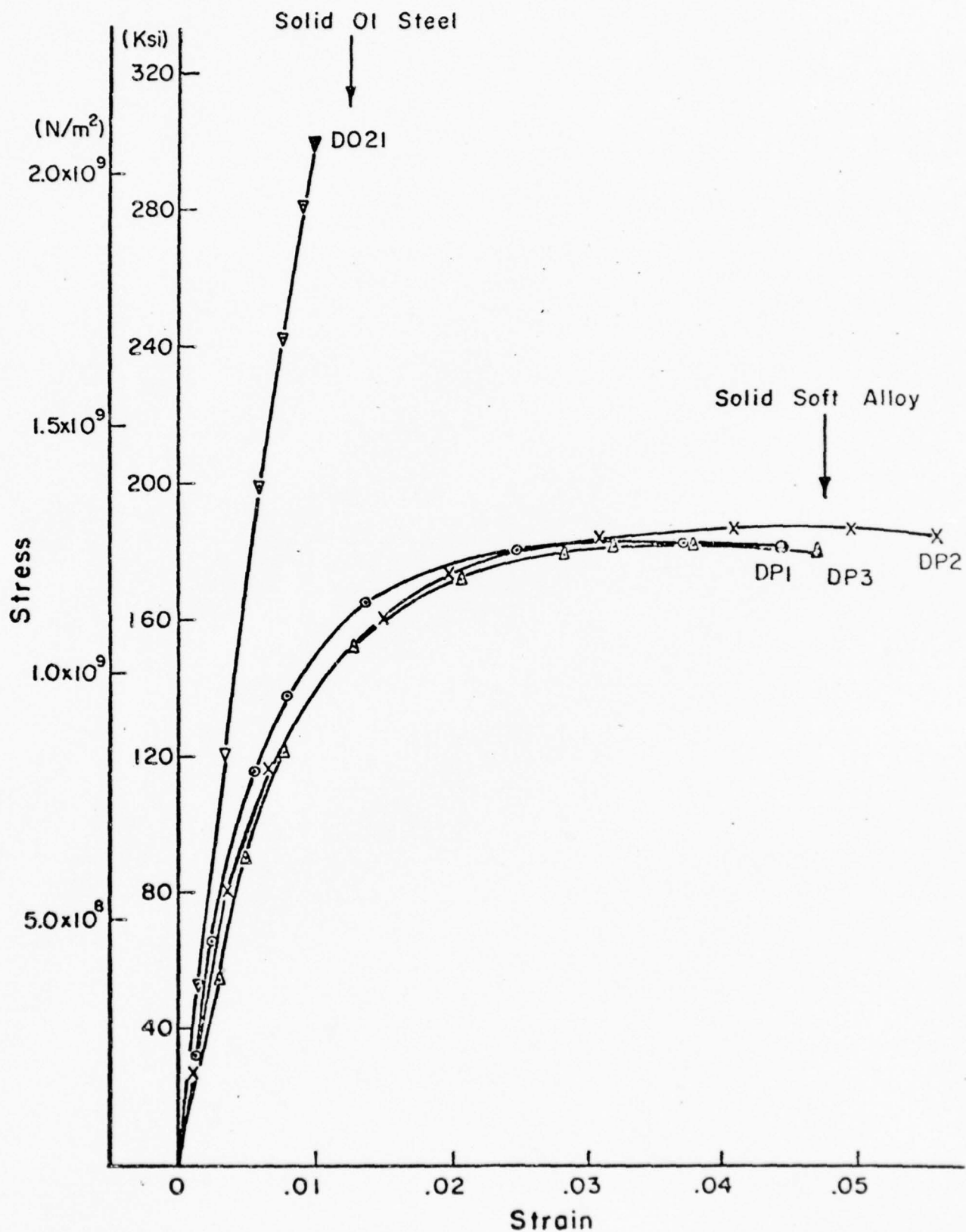


Figure 13. The Stress-Strain Curves for Solid Oil Steel and Solid Purdue Soft Alloy PS2.



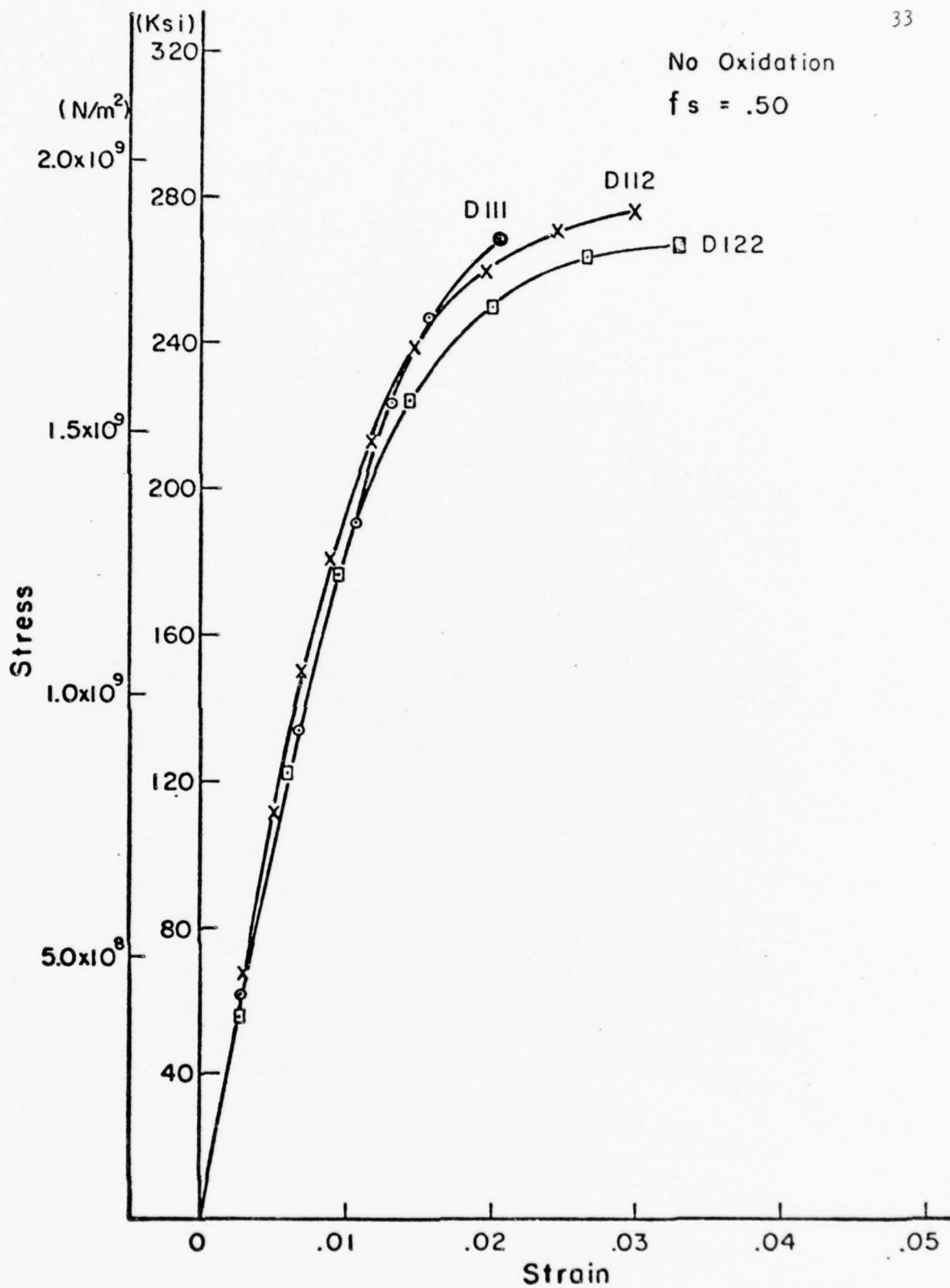


Figure 14. The Stress-Strain Curves for Specimens with No Oxidation Treatment Prior to Hot-Roll Welding.

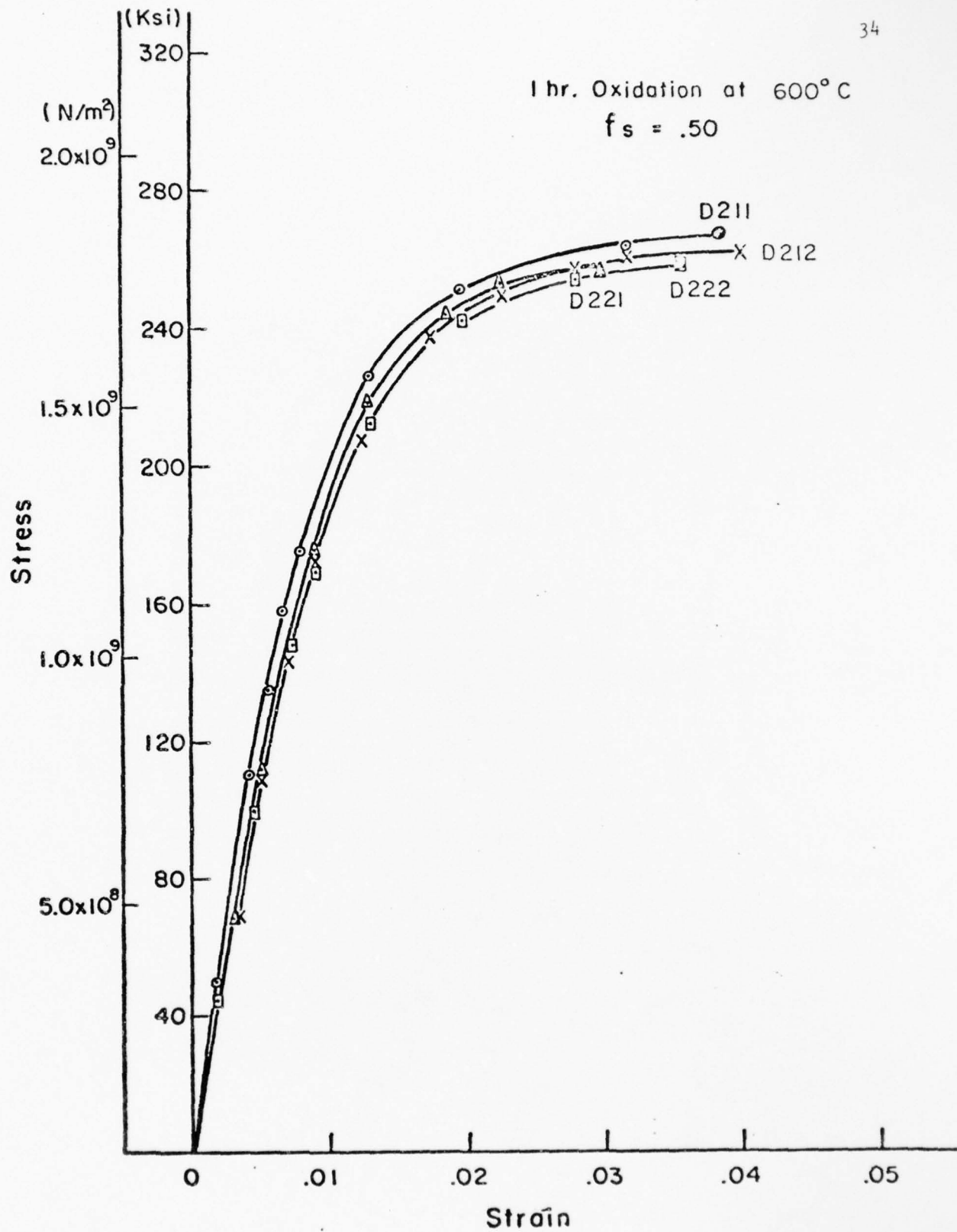


Figure 15. The Stress-Strain Curves for Specimens with 1 hr. Oxidation at 600°C.

2 hrs Oxidation at 600°C

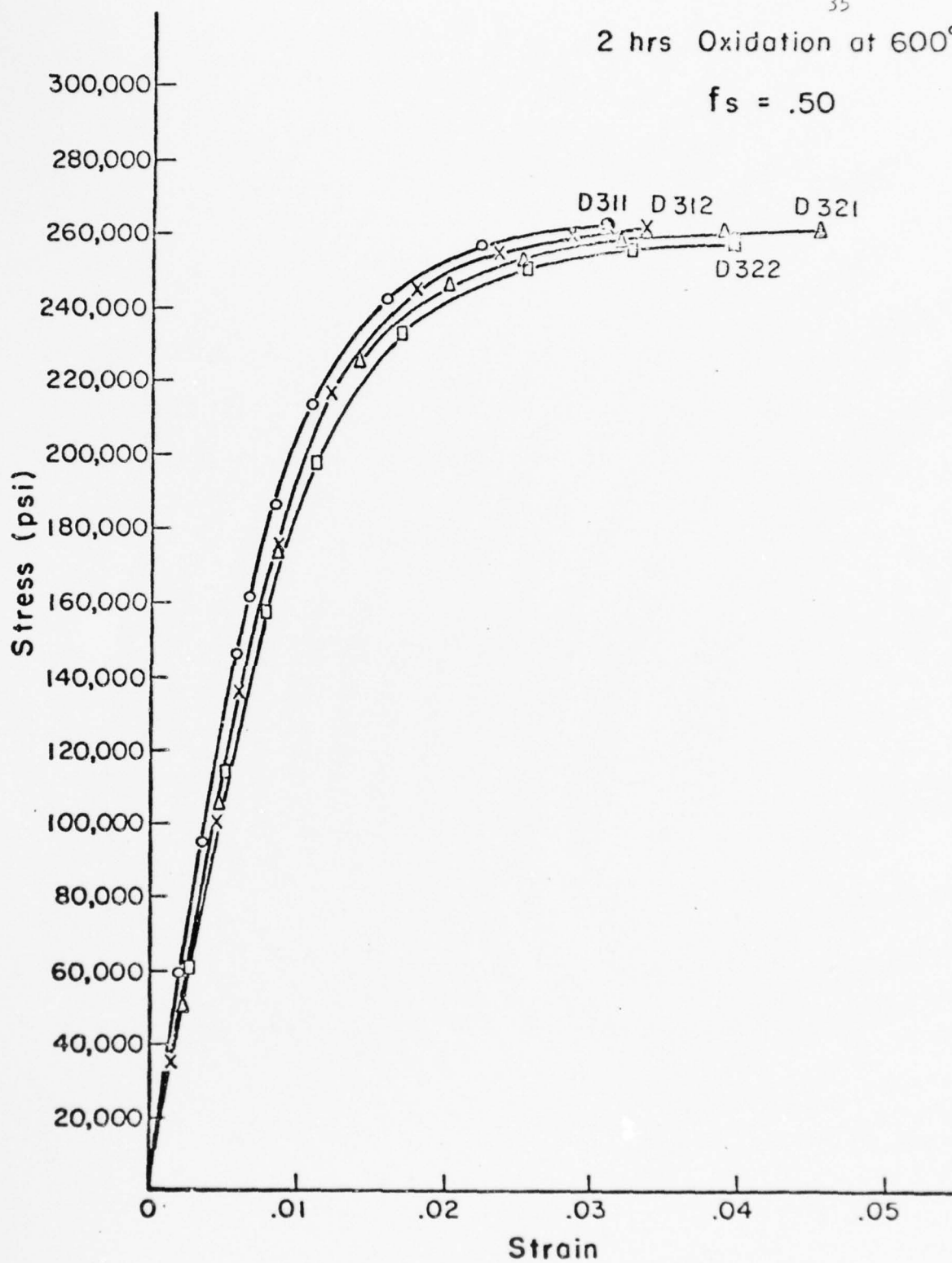
 $f_s = .50$ 

Figure 16. The Stress-Strain Curves for Specimens with 2 hrs. Oxidation at 600°C.

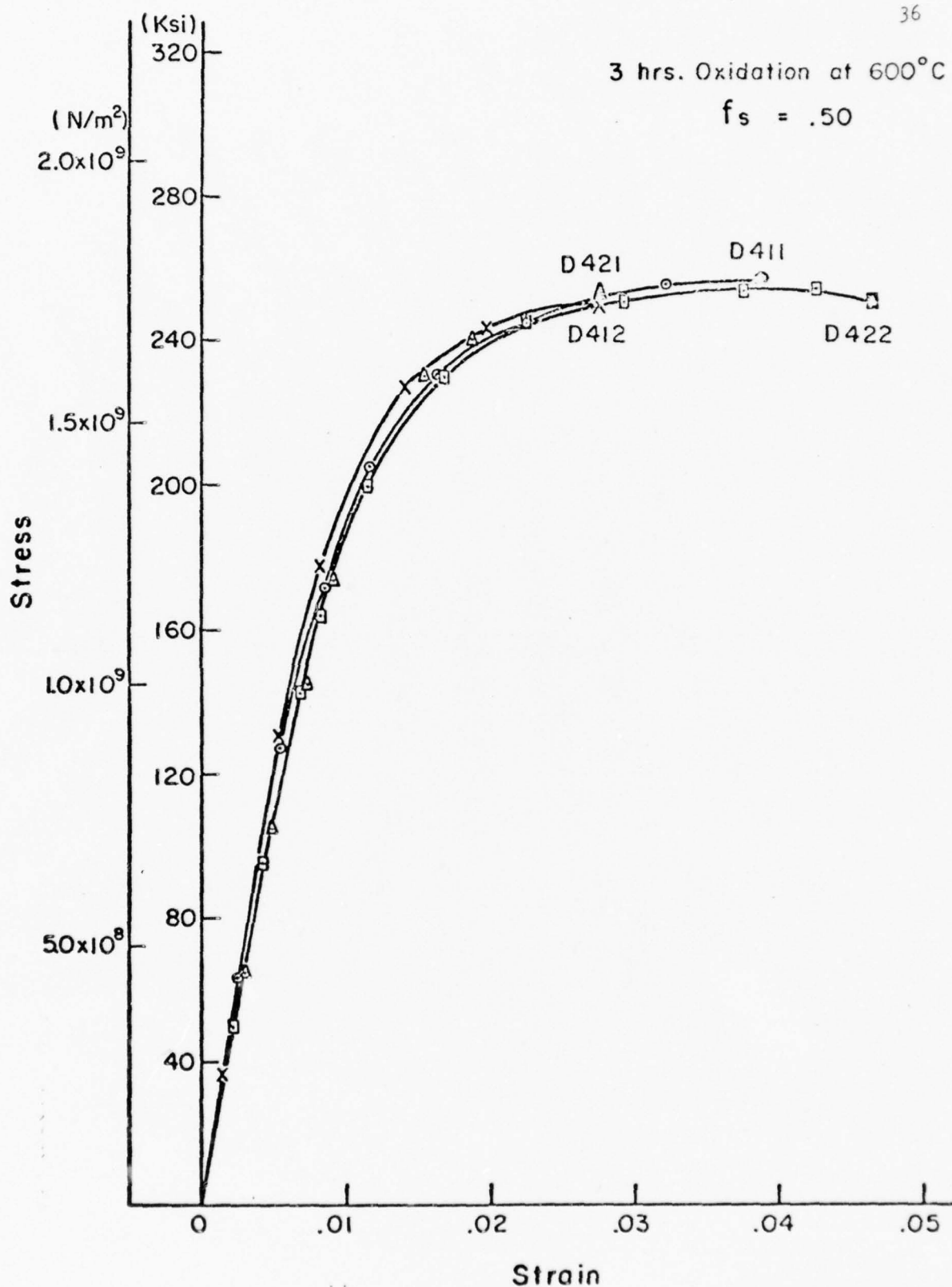


Figure 17. The Stress-Strain Curves for Specimens with 3 hrs. Oxidation at 600°C.

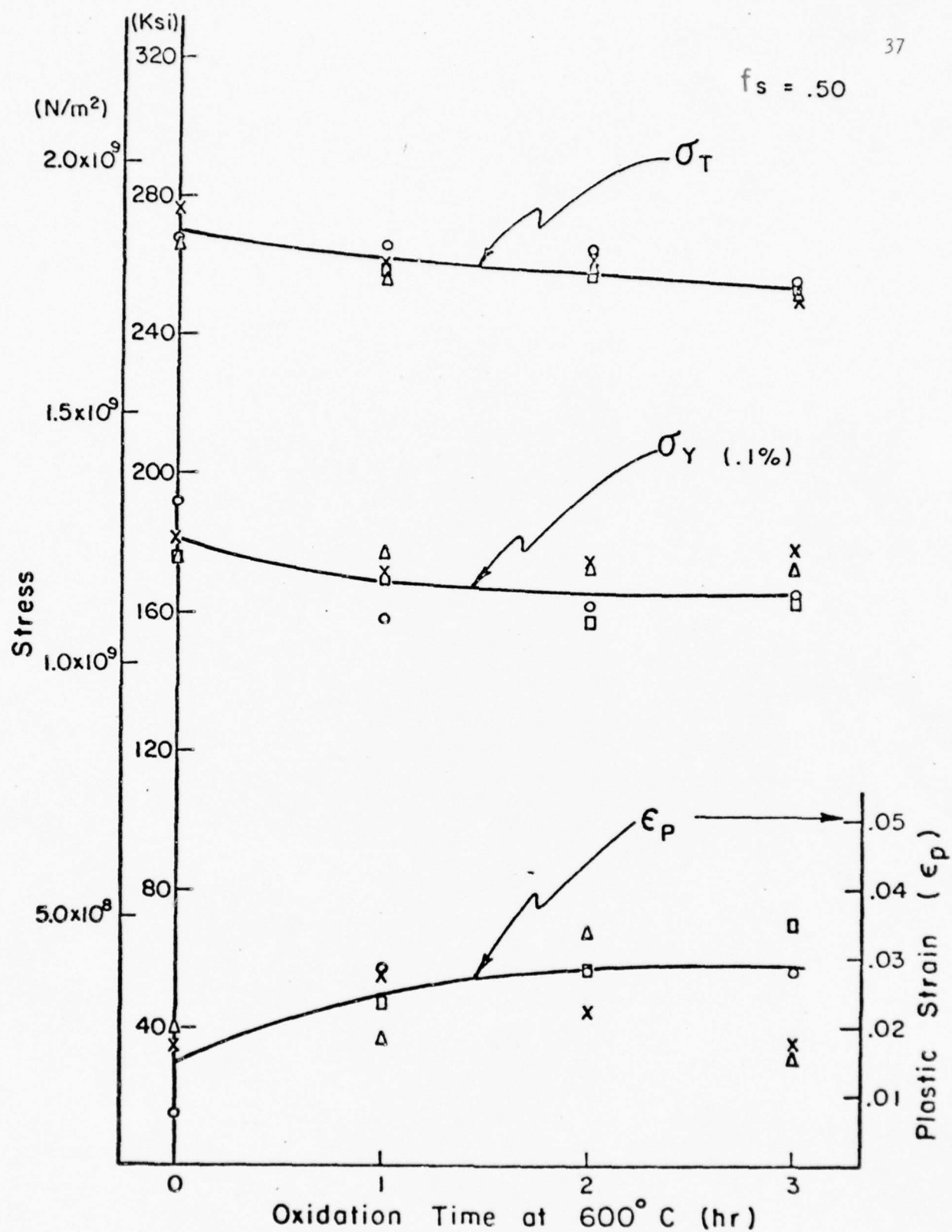


Figure 18. The Tensile Stress, .1% Yield Stress and Plastic Strain as a Function of Oxidation Time for Specimens with  $f_s = .50$ .



increases the interface bonding becomes less perfect. The unbonded areas where retained oxide particles reside may serve as a blunt to the approaching crack and may also allow the interface to separate and let the soft layer to deform independently. As a result, the plastic strain and percent reduction in area are increased as oxidations increases. This is also in agreement with the interfacial bonding energy measurement. The small decrease in the strengths, less than a 10% drop as specimens oxidized for 3 hrs., may be due to the slight decrease in effective hard layer volume by decarburization accompanying oxidation. The plastic strain is almost doubled as oxidation time is increased to 3 hrs. The plastic strain increases more rapidly initially and levels off after about 2 hrs. oxidation.

### 3.2.2.3 The Effect of Soft Layer Fraction on Tensile Properties at Fixed Oxidation Time (Partial Debonding).

Two hours oxidation at 600°C appears to be an optimum treatment for the alloy complex with  $f_s = 0.50$  in terms of tensile properties (Fig. 18). In order to see the effect of soft layer fraction at this optimum treatment, four additional sets of specimens:  $f_s = 0$  (i.e., laminated 01 steel),  $f_s = .25$ ,  $f_s = .75$ , and  $f_s = 1.0$  (i.e., laminated soft alloy PS2), were prepared for comparison with the  $f_s = .50$  set of specimens already tested.

The  $\sigma$ - $\epsilon$  curves for these five sets of specimens are presented Fig. 19. All the  $f_s = 0$ , and  $f_s = .25$  sets of specimens failed outside the reduced section and are included to show their brittle nature and the crack jumping phenomena which was expected (Design Rationale. The slope of the elastic portion of  $\sigma$ - $\epsilon$

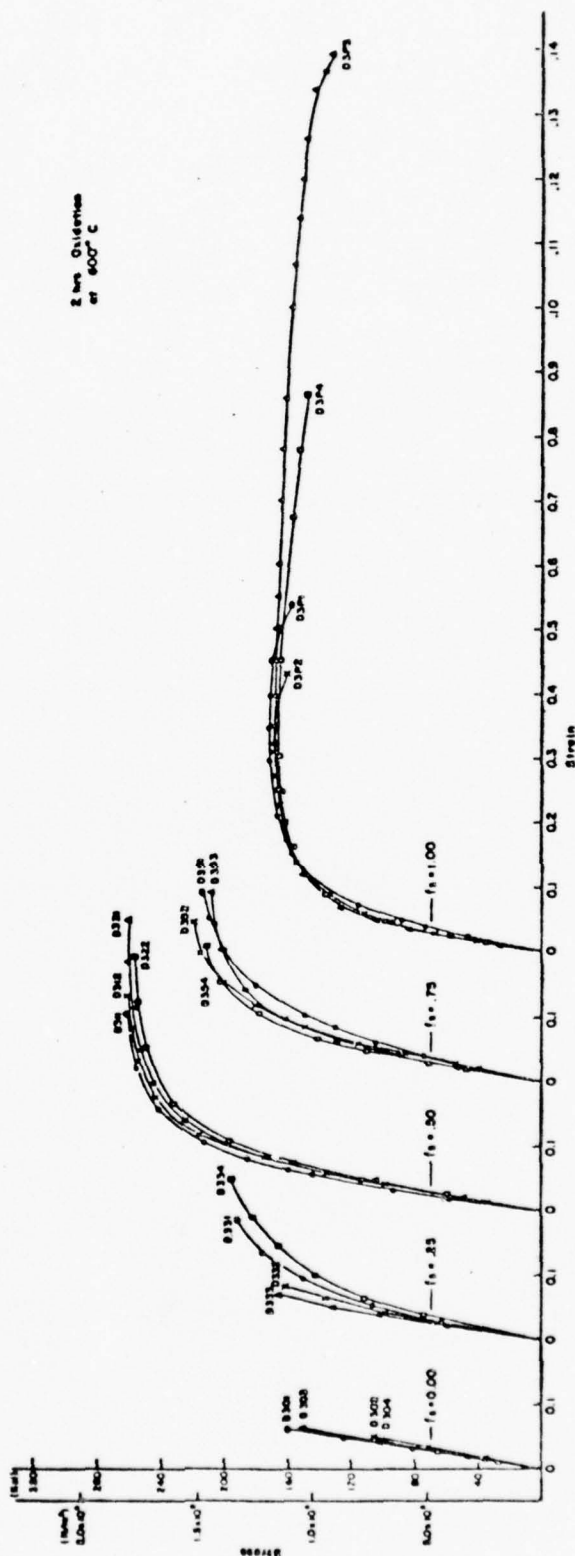


Figure 19. The Stress-Strain Curves for Specimens with  $f_s = 0, .25, .50, .75$  and  $1.00$ . All specimens were oxidized at  $600^\circ\text{C}$  for 2 hrs. prior to hot-roll welding.

curves decreases as  $f_s$  increases. The tensile stress and 0.1% yield stress drop sharply as  $f_s$  increases (Fig. 20). The plastic strain and percent reduction in area increase slowly with increasing  $f_s$  and rapidly beyond  $f_s = .75$ . The amount of plastic strain as a function of soft layer fraction seems to deviate from the law of mixtures while the strengths of the alloy complex agree well with the law of mixtures.

### 3.2.3 Microstructure.

An example of oxide particles retained in the interfacial area is shown in Fig. 21. The nearly circular shape dark particles across the middle of the micrograph are oxide particles. This SEM micrograph with a 3000 magnification was taken on a section of a specimen in which layers were oxidized at 600°C for 30 minutes prior to rolling.

The optical microstructure of complex D121,  $f_s = .50$  and oxidation treatment 2 hrs. at 600°C, is shown in Fig. 22.

### 3.2.4 Microhardness.

Tensile specimen D121 was sectioned into five pieces. The outer two parts including pin hole and the central reduced section were mounted and polished for microhardness measurement. Fig. 22 shows the Knoop hardness number versus distance modulation direction (i.e., perpendicular to interfaces). The hardness numbers in hard or soft layers alone are quite consistent except two outer soft layers.

The hardness numbers in the hard layers are around 800 while those in the soft layers are about 410. The constant hardness of

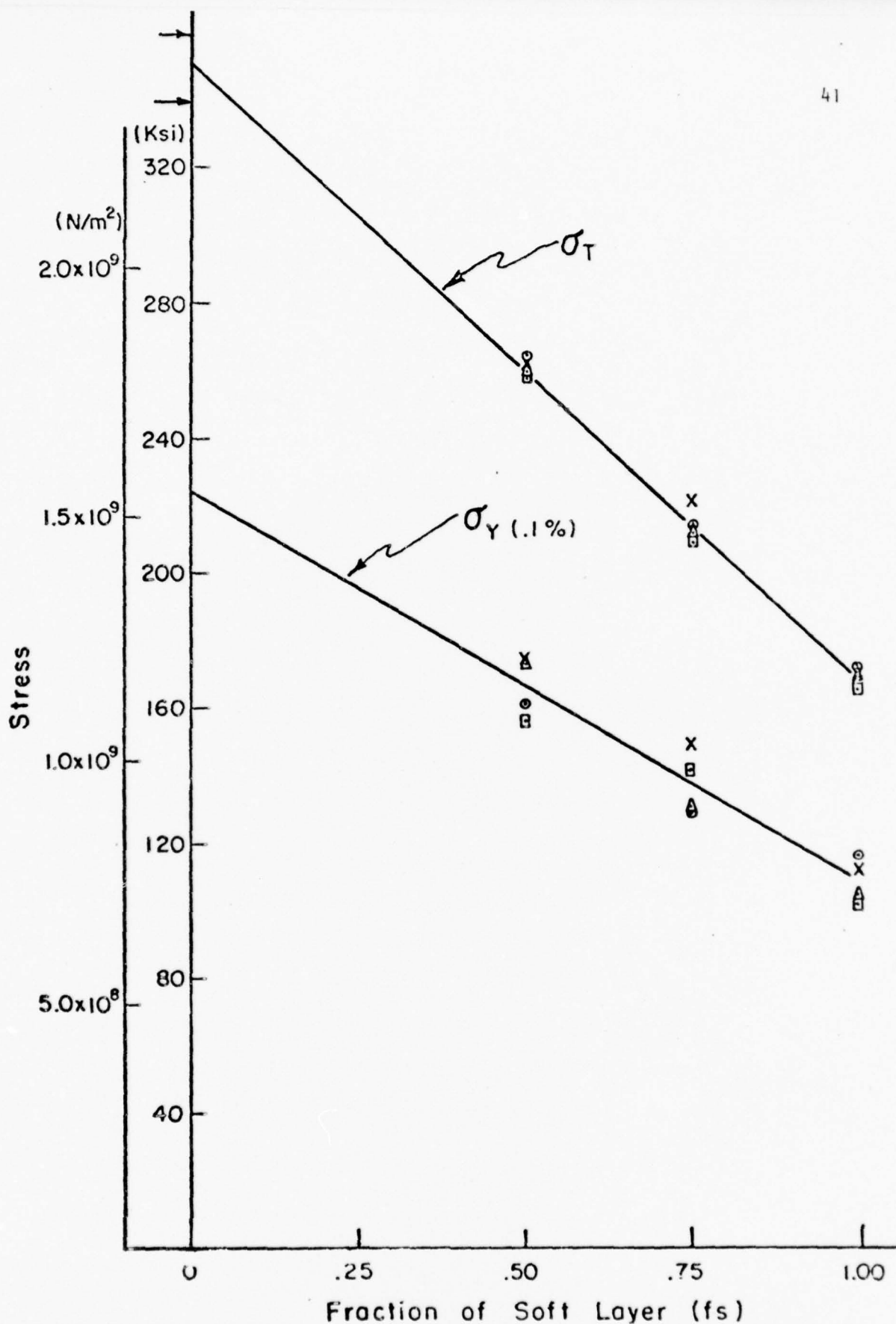


Figure 20. The Tensile Stress and .1% Yield Stress as a Function of Fraction of Soft Layer for the Same Specimens as in Figure 17. Arrows at the upper left corner of the figure represent the upper and lower bounds of 01 steel strength converted from microhardness data.

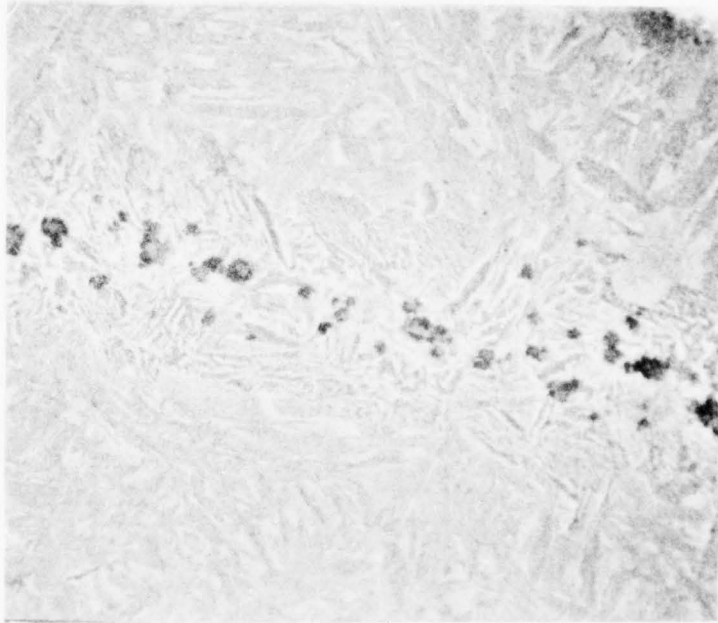


Figure 21. The Microstructure of a Specimen Oxidized at 600°C for 1/2 hr. Prior to Hot-Roll Welding. The dark particles in the central portion of the micrograph are oxide particles. Magnification 3000x



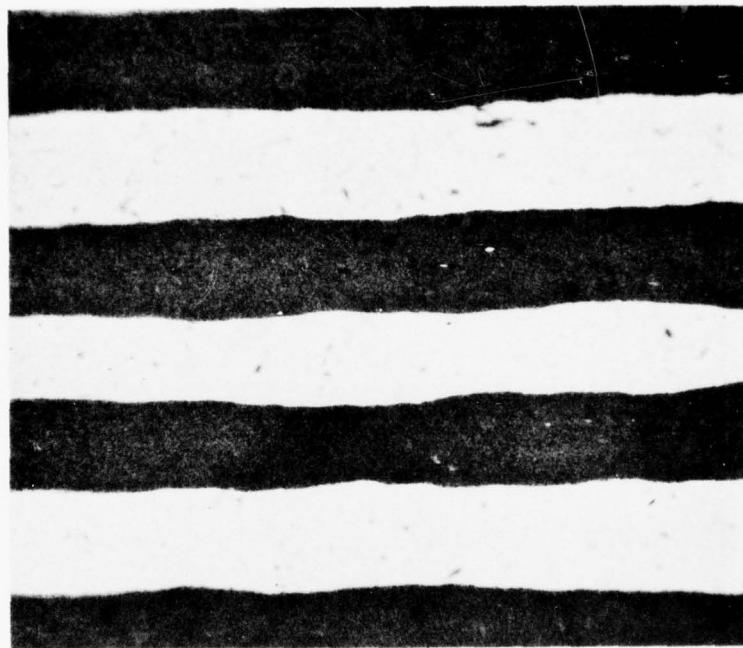


Figure 22. The Microstructure of Specimen D 121. The dark areas represent the hard layer (01 Steel) consisting of fine martensite with a small amount of retained austenite. The light areas are the soft layer (Purdue S2 alloy) in which the martensite appears to have larger plate size. Magnification 80X.

# Specimen D121

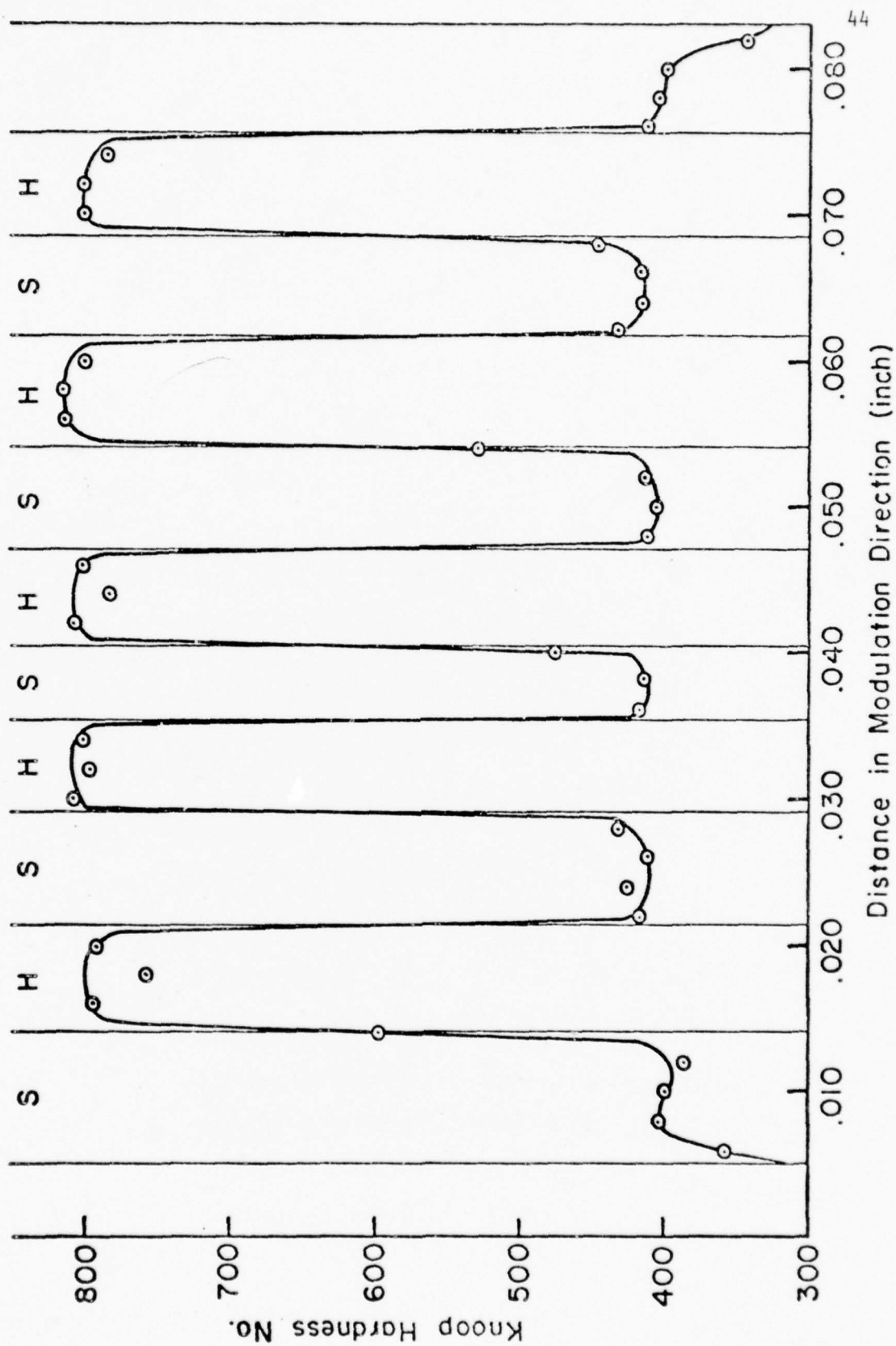


Figure 23. The Microhardness As a Function of Distance in Modulation Direction for Specimen D 121.

the soft and hard layers and proper hardness achieved in both prove that the heat treatment was properly performed. The decrease in hardness at the exterior surface of the outer soft layers might be due to the draining of carbon from these layers into the stainless steel container during the hot-roll welding process.

### 3.2.5 Fracture Path.

The fracture surfaces of all the specimens tested were examined microscopically. Typical schematic fracture topographies are shown in Figs. 24 and 25 for no oxidation, 3 hrs. oxidation at 500°C respectively. Figure 24A is a scanning electron micrograph of a typical portion of the fracture shown schematically in Fig. 24. Figure 25A shows a corresponding view for Fig. 25 in the fracture topography; first, the overall fracture surface is irregular in appearance except for a few hard layers where smooth brittle fracture occurred. Secondly, debonding along interfaces and some degree of necking of individual layers is present. Thirdly, the origins of cracks in these specimens were usually located in the interior. These four figures show that as oxidation time is increased, the amount of necking as well as the amount of partial debonding increases. This results in the increased strain and reduction in area as observed in the tensile test results. Figs. 26, 27, 28, 29, and 30 show schematically the fracture appearances of specimens D304, D332, D353, and D3P4. These specimens were all oxidized for 2 hours and show soft layer contents which range from zero to one. Figs. 26A, 27A, 28A, 29A, and 30A are scanning electron micrographs of the portions of the

## Specimen D 112

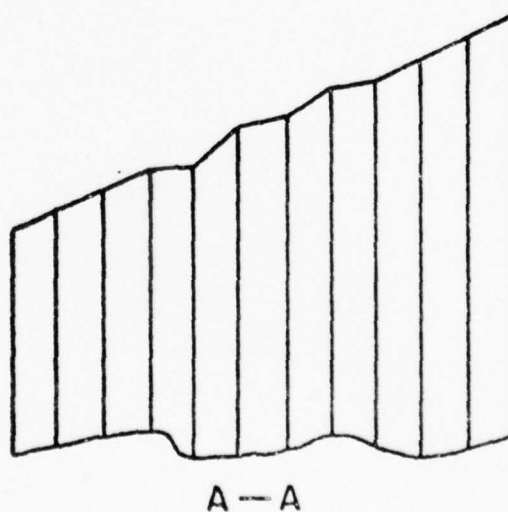
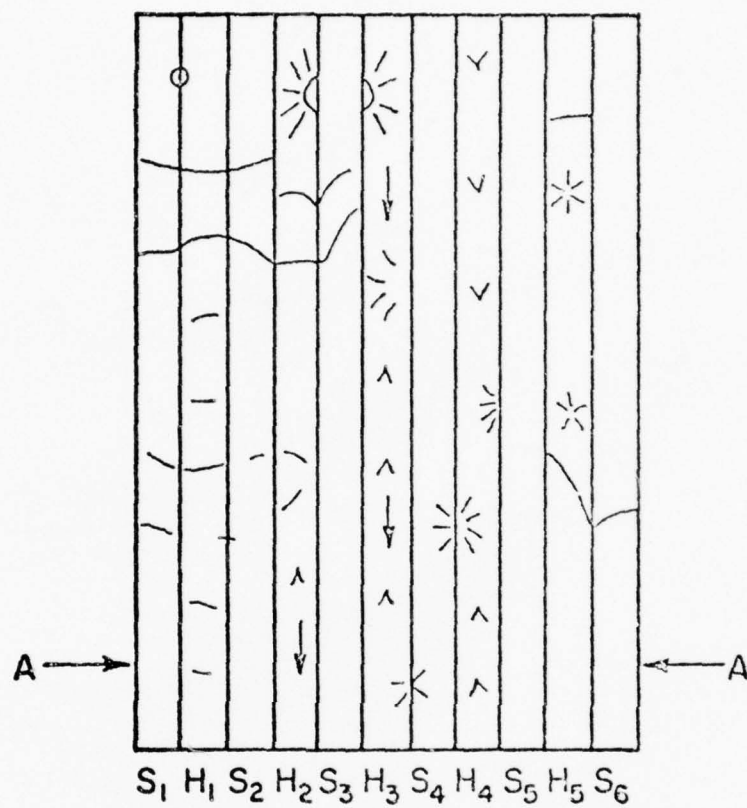


Figure 24. A Schematic Fractograph for Specimen D 112. The crack originated from H<sub>2</sub>, S<sub>3</sub>, and H<sub>3</sub> area. The shear fracture modes dominated except in H<sub>2</sub>, H<sub>3</sub>, and H<sub>4</sub> where brittle fracture occurred. No debonding or necking was observed.

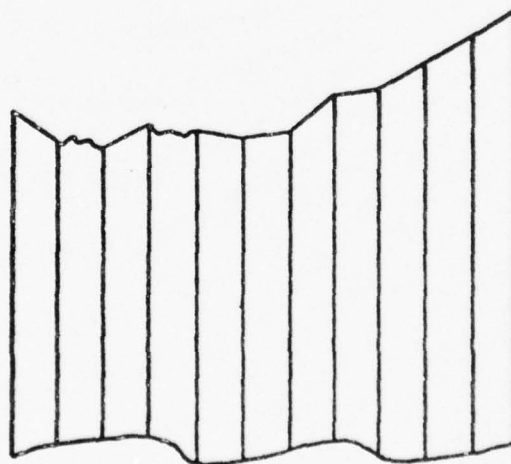
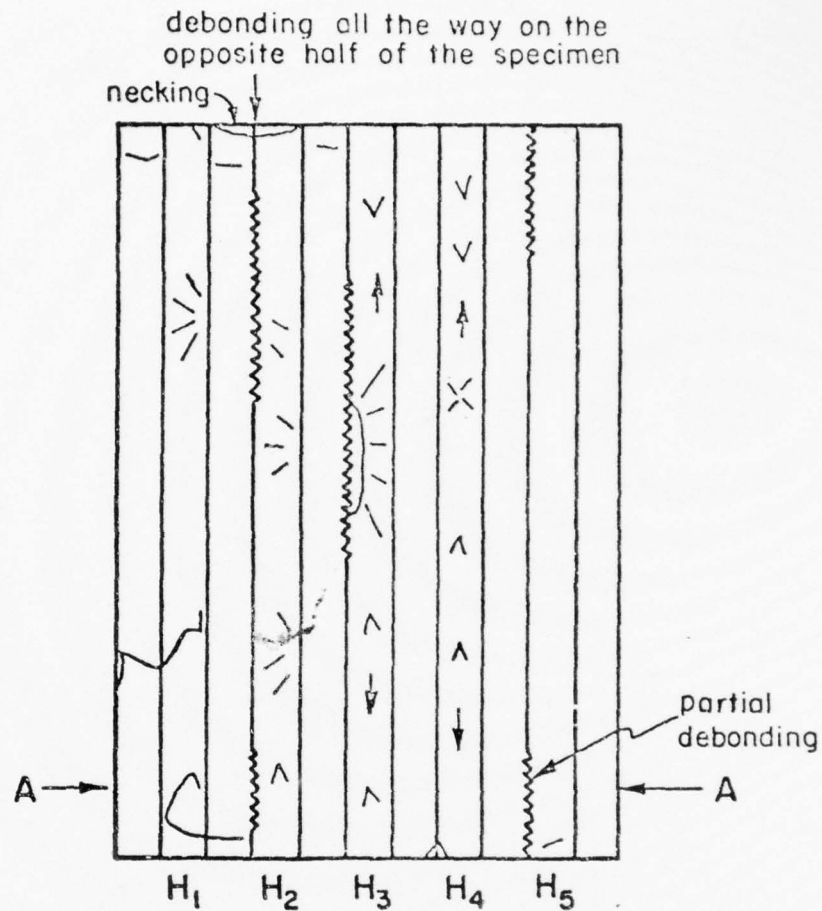


Figure 24A. A Micrograph Showing the Fracture Surface of Specimen D 112.  
Magnification 100x.



# Specimen D411

48



A—A

Figure 25. A Schematic Fractograph for Specimen D 411. There are more typical cone and cup tensile fracture characteristics at edges, more debonding. Shear fracture modes were observed except H<sub>3</sub> and H<sub>4</sub>. The crack originated from the central portion of H<sub>3</sub>.

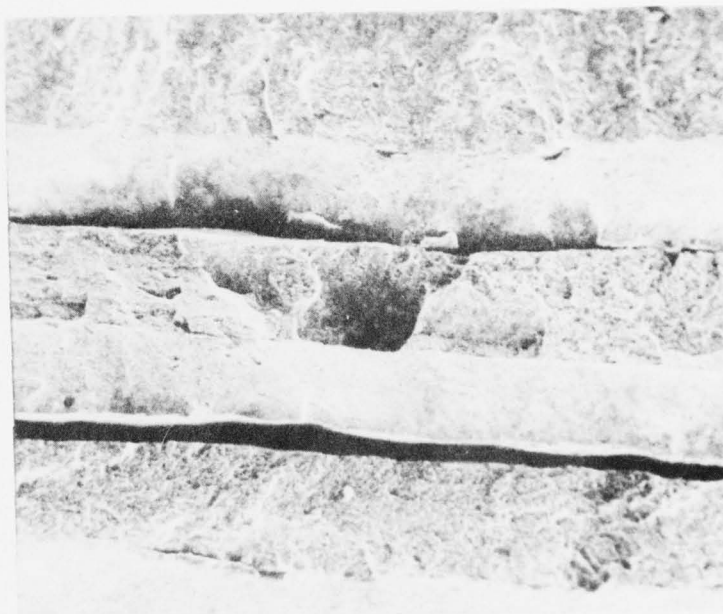


Figure 25A. A Micrograph Showing the Fracture Surface of Specimen D 411.  
Magnification 100x.

## Specimen D 304

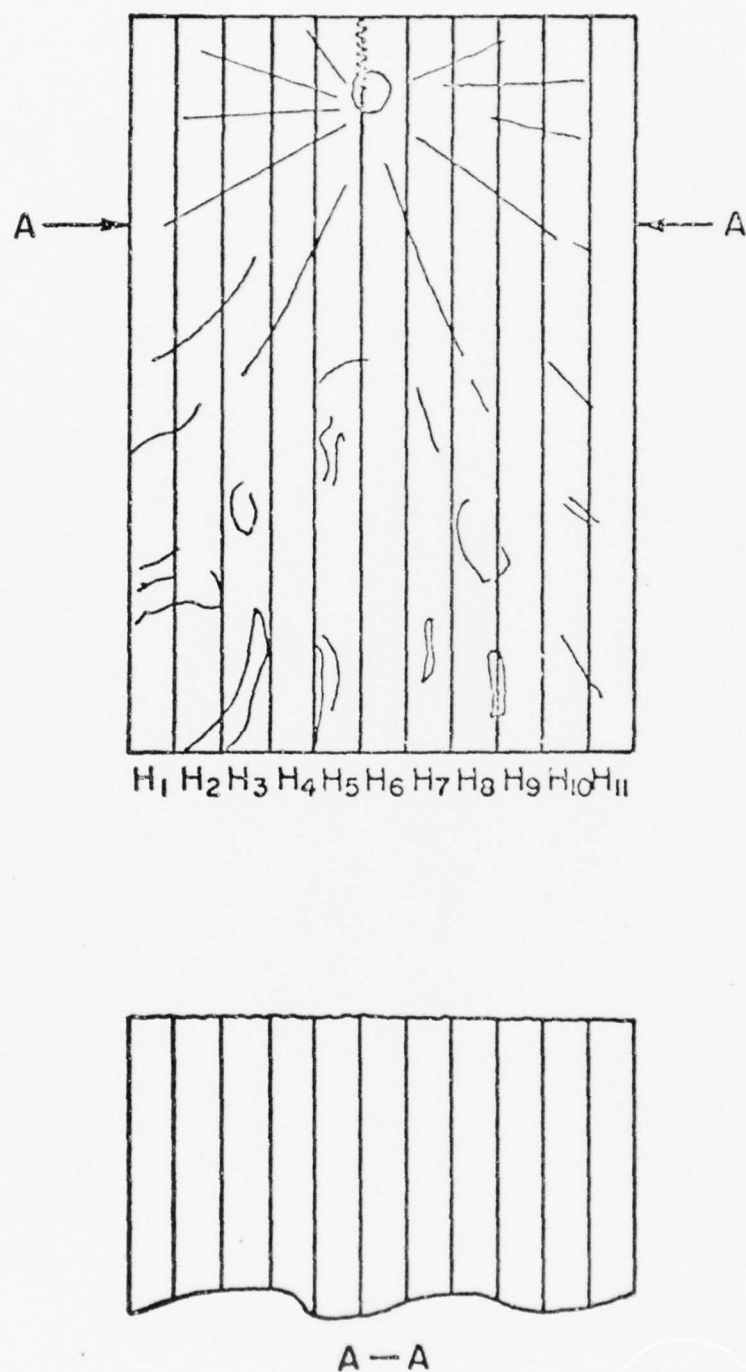


Figure 26. A Schematic Fractograph for Specimen D 304 ( $f_s = 0$ ). Crack originated from the interface between  $H_5$  and  $H_6$ . Brittle fracture occurred in the upper half of the specimen and shear dimple type in the lower half. The interfaces were indistinguishable.

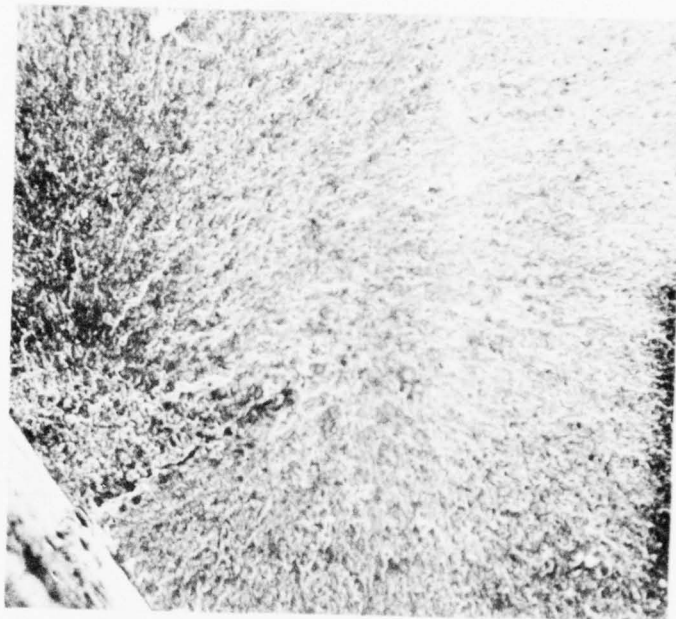
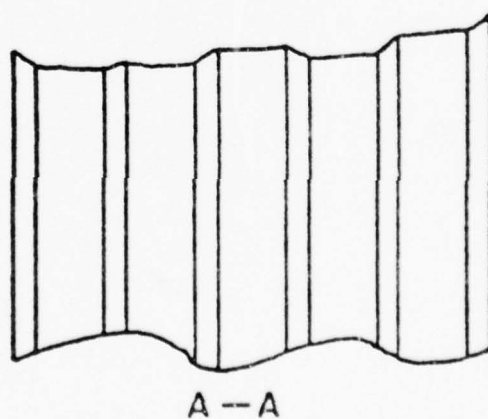
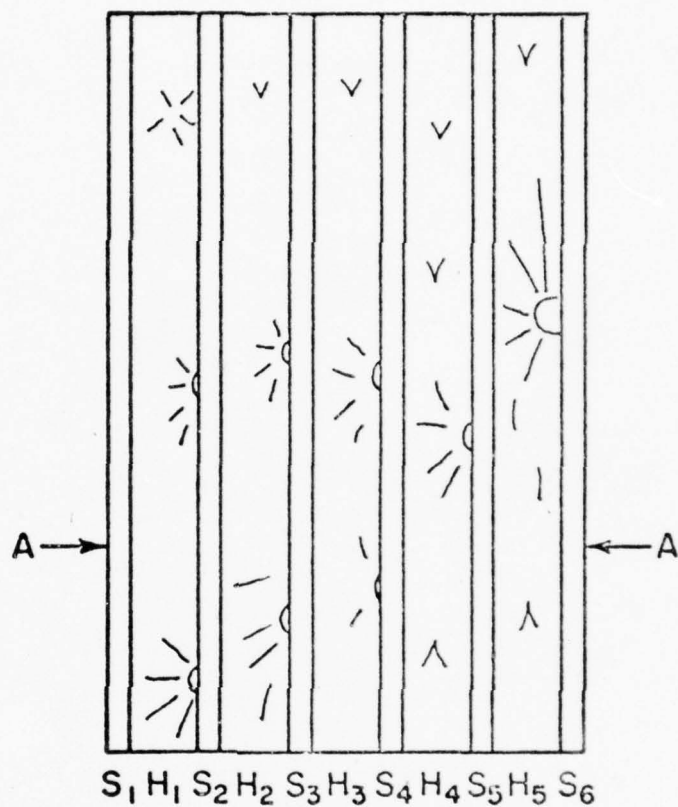


Figure 26A. A Micrograph Showing the Fracture Surface of Specimen D 304.  
Magnification 100x.

## Specimen D 332



**Figure 27.** A Schematic Fractograph for Specimen D 332 ( $f_s = .25$ ). Brittle fracture occurred in hard layers and shear fracture occurred in soft layers. Crack originated from H<sub>5</sub> propagating to the left of the specimen. Multiple crack nucleation sites were observed in hard layers.



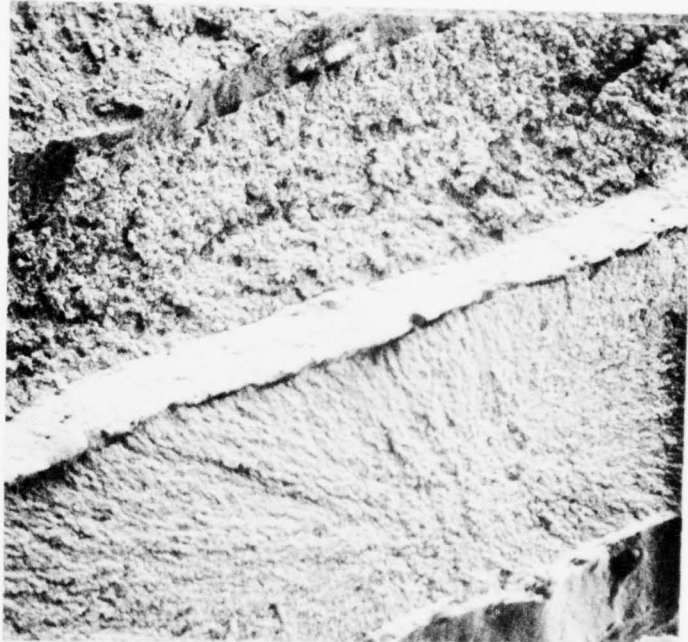


Figure 27A. A Micrograph Showing the Fracture Surface of Specimen D 332.  
Magnification 100x.

## Specimen D 312

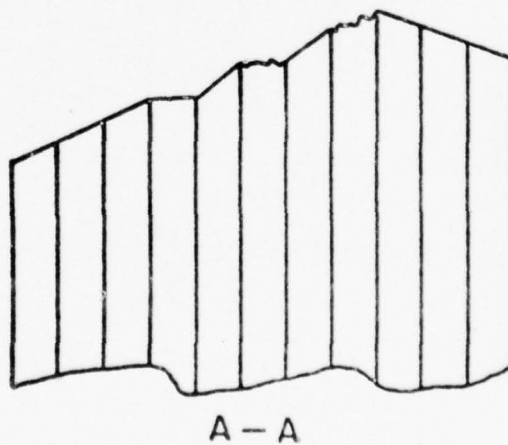
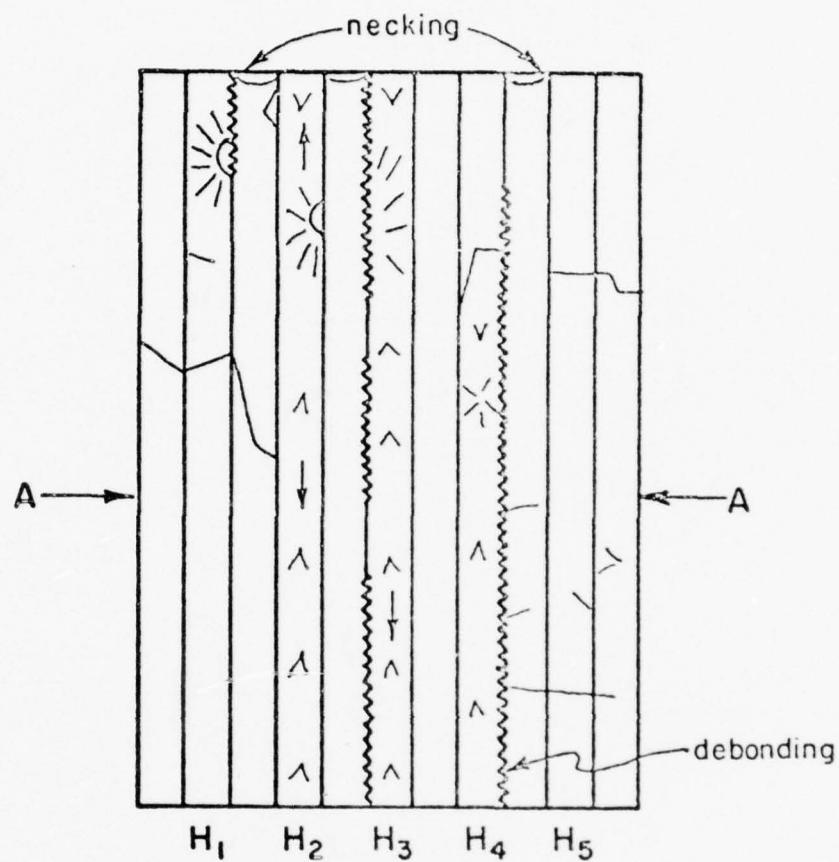


Figure 28. A Schematic Fractograph for Specimen D 312 ( $f_s = .50$ ). Repeated from Figure 23.

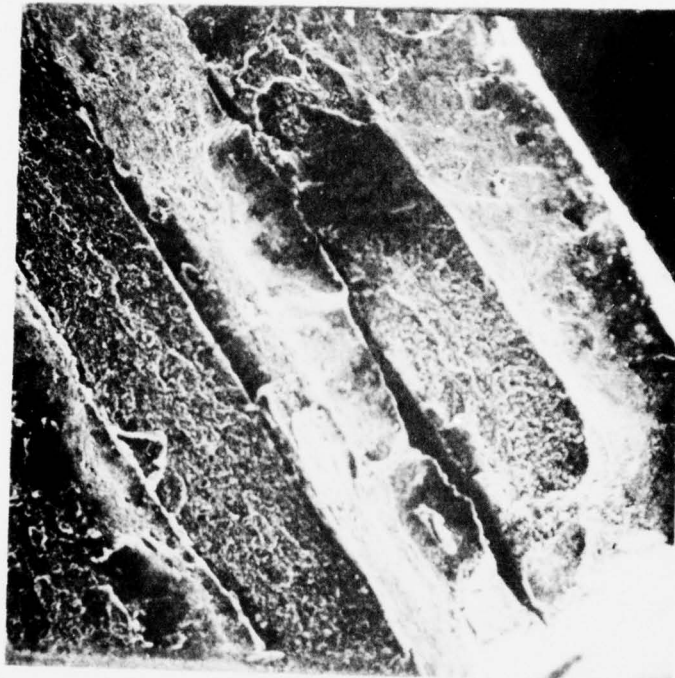


Figure 28A. A Micrograph Showing the Fracture Surface of Specimen D 312.  
Magnification 100x.

## Specimen D 353

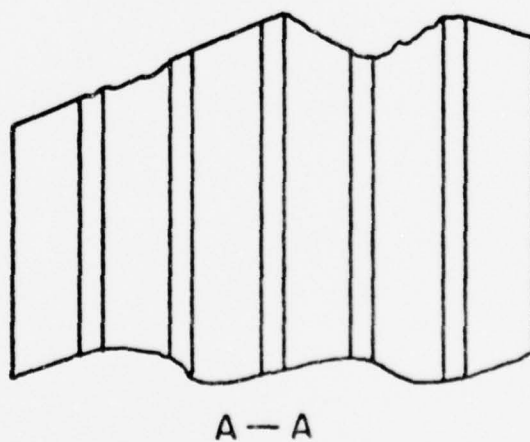
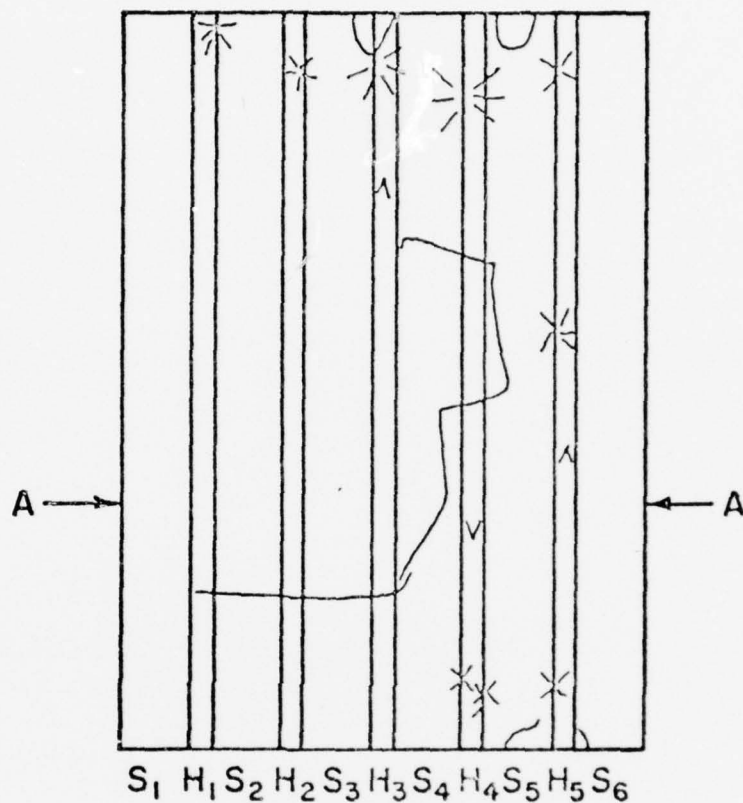


Figure 29. A Schematic Fractograph for Specimen D 353 ( $f_s = .75$ ). Except H<sub>5</sub>, mostly shear fracture modes were observed. Crack originated from the upper portion of the specimen, most likely H<sub>4</sub>.

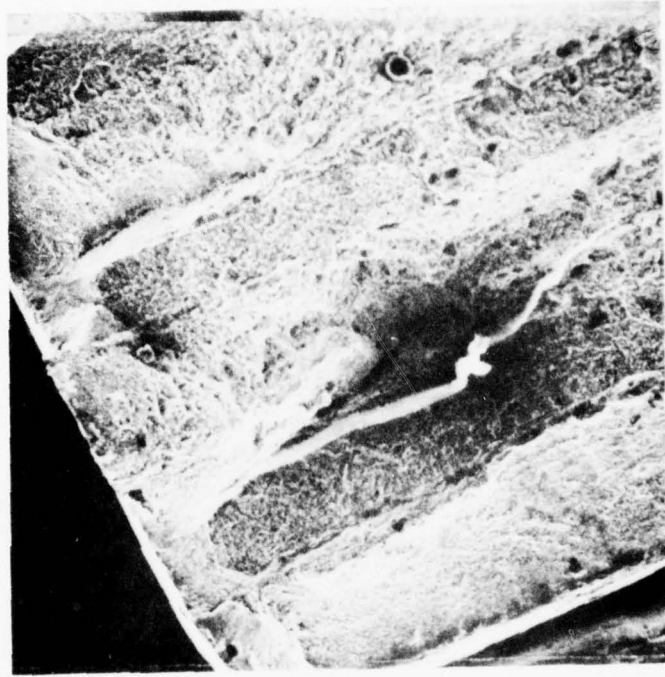


Figure 29A. A Micrograph Showing the Fracture Surface of Specimen D 353.  
Magnification 100x.

## Specimen D3P4

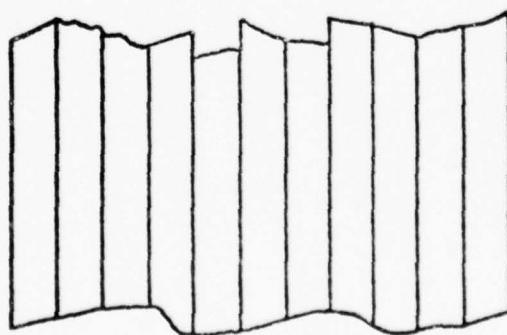
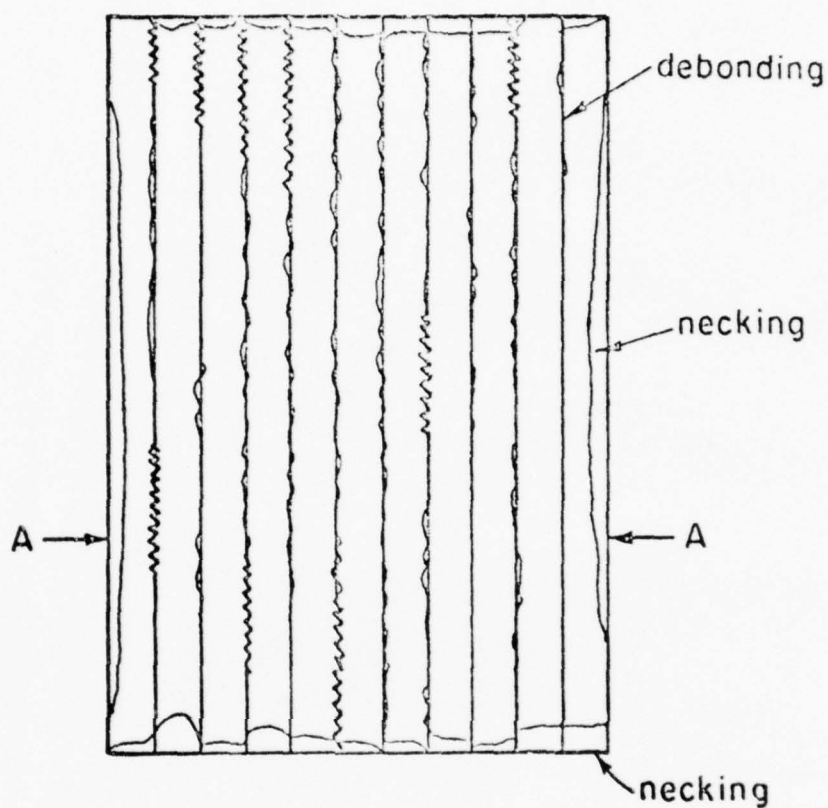


Figure 30. A Schematic Fractograph for Specimen D3P4 ( $f_s = 1.00$ ). Exclusively ductile shear fracture occurred in this specimen. There was about 95% debonding and large amount of necking observed.



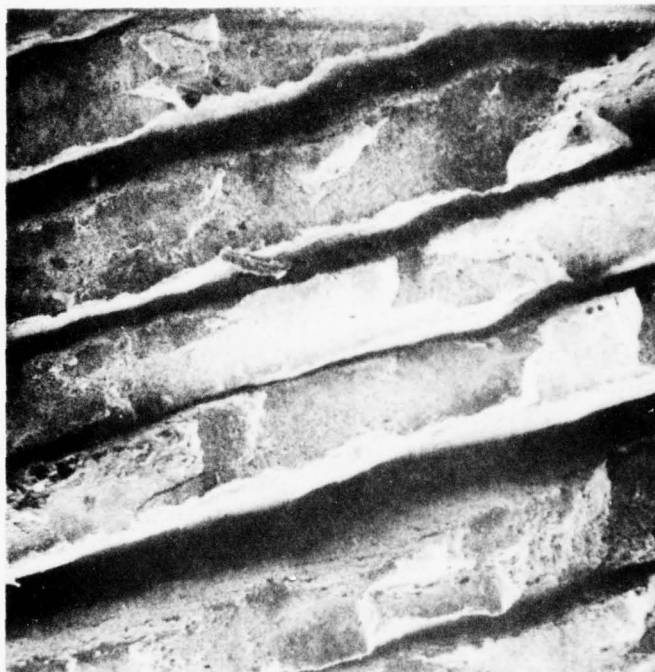


Figure 30A. A Micrograph Showing the Fracture Surface of Specimen D3P4.  
Magnification 100x.

fractures shown in Figs. 26-30. The fracture in the laminated 01 steel (Fig. 26) shows typical brittle fracture characteristics. For specimens with  $f_s = .25$ , Fig. 27 shows several crack nucleation sites as fracture propagated across the whole specimen. As  $f_s$  is increased, Figs. 28 and 30, the degree of debonding and necking increases and so does the amount of shear fracture. Fig. 29 shows reduced debonding and necking and the corresponding tensile tests show decreased ductility but not decreased area reduction. The reason for this exceptional behavior is not clear.

In contrast to the scanning electron micrographs of fractures of laminated complexes, the fracture of the solid 01 and solid PS2 alloy are both smooth and perpendicular to the tensile axis. These are shown in Figs. 31 and 32.

### 3.3 Conclusions.

A Purdue soft layer alloy PS2 has been designed based on several design criteria to match the hard layer alloy, AISI type 01 tool steel. The PS2 alloy was successfully fabricated with a vacuum melting facility at crystal growing laboratory of Purdue University. The ingots were hot-rolled to suitable size for manufacturing of alloy complex (MMS) with 01 steel.

One of the most important conclusions in a preliminary study was that the interfaces were too well bonded. As a result, the soft layers could not deform independently and little ductility was observed. In the model system, a technique of creating partial debonding in interfaces by oxidation of the surfaces of layers prior to hot-roll welding has been developed and evaluated. A method of interfacial bonding energy measurement was developed to characterize the inter-

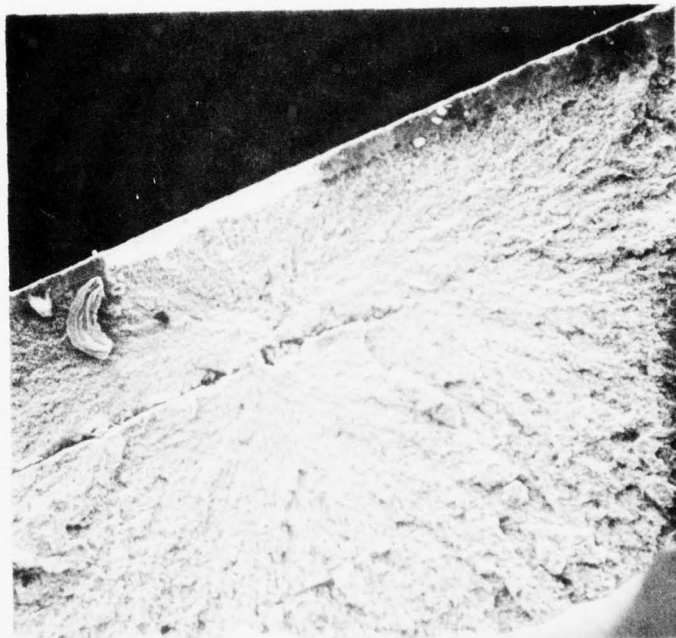


Figure 31. A Micrograph Showing the Origin of a Crack in a Solid 01 Specimen.  
Magnification 100x.

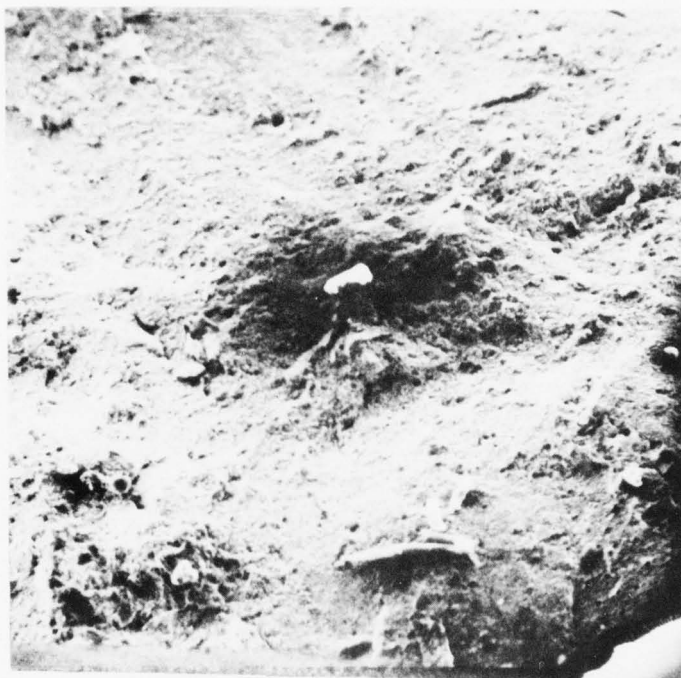


Figure 32. A Micrograph Showing the Origin of a Crack in a Solid Purdue S2 Specimen. Magnification 100x.

face bonding and preliminary measurements were made which show that the energy decreases as the oxidation time increases.

The partial debonding which resulted from the retained oxide particles in the interfaces, contributes ductility to the alloy complex as had been theorized. The evidence is shown in the study of the effect of oxidation time on the tensile properties of alloy complex at 50% soft layer fraction. In that study, the tensile stress and .1% stress decrease slowly with increasing oxidation time, while the plastic strain increases rapidly as oxidation increases which is in agreement with interfacial bonding energy measurement.

In the case of the effect of soft layer fraction on the properties of alloy complex at constant oxidation time, i.e., identical debonding condition, the results show: (1) the tensile stress ( $\sigma_T$ ) and .1% yield stress ( $\sigma_Y$ ) drop sharply as  $f_s$  increases; (2)  $\sigma_T$  and  $\sigma_Y$  of the alloy complex obey the law of mixtures; (3) the plastic strain and the percent reduction in area increase slowly with increasing  $f_s$  and rapidly beyond  $f_s = .75$  which seems to deviate from the law of mixtures.

The examination of fracture surfaces revealed that the shear fracture modes dominate except in few hard layers where brittle fracture occurred for specimen of 50% soft layer. The fracture topography was quite irregular. There were more partial debonding and more necking which implied more plastic strain as oxidation time was increased. This agrees with the tensile test results quite well.

Another interesting observation was that the failure in these specimens originated mostly from interior rather than from the edge of one hard layer as occurred in preliminary tests. This suggests

that the replacements of hard layers by soft ones on the outermost layers helps decrease the probability of specimen failure from surface flaws.

### 3.3.1 Conclusions from Model System

The following conclusions were drawn from the study of the model system and were used in planning the high strength system program:

1. The design rationale on strength was not disproved. The law of mixtures holds for tensile strength for fractions soft layers greater than about 0.5 when this premature fracture occurs which is predicted by the design rationale as due to elastic crack jumping.
2. To get deformation in (and hence fracture toughness from) the soft layers they must debond from the adjoining hard layers during deformation and fracture. A technique for developing interfaces which will debond has been partially developed.
3. A very high hardness hard layer is required to get the design strength at  $0.5 = f_s$ . The soft layer should also be as strong as possible.

## IV. THE HIGH STRENGTH SYSTEM

The high strength complexes contain alternating layers of high-speed tool steel and a matching lower hardness alloy. They were designed to utilize the maximum hardness available in the high-speed steel and to achieve toughness by allowing independent deformation of the softer alloy. Initially REX 71<sup>\*</sup> was used at a hardness of 70 Rc

---

<sup>\*</sup>Crucible Steel.



(1075 DPH)(obtained by triple tempering at 540°C) as the hard layer and alloy PS4 was matched to it. However, complexes from REX 71 always fractured in the prior austenite grain boundaries at a stress much below that expected from the indentation hardness. AISI M4 tool steel was substituted for REX 71 to help avoid this premature fracture problem. Although this substitute was successful, M4 has a maximum hardness of 65 Rc (800 DPH) which represents a substantial decrease in potential strength. Essentially all the work reported in this section is on M4/PS4 complexes.

Another major change was required in order to control bonding of soft layers to high-speed steel hard layers. The high-speed steel layers contain alloying elements which reduce preformed oxides and these layers usually either bond readily to the soft layer or form a gas pocket along the interface. (The gas is presumed to be Co formed by reduction of the iron oxide which had been positioned in the interface.) To control the bonding in these complexes two thin layers of austenite stainless steel (AISI type 310) were placed at each interface and their interface was oxidized and formed the parting plane. The properties of this interface and interface zone will be described.

#### 4.1 The Alloys and Heat Treatment.

The alloy complex is comprised of two essential layers which alternate and are separated by a thin interface zone. The alloys comprising the two essential layers must be:

1. compatible in heat treatment, i.e., they must be heat treated together,
2. equal in carbon activity, i.e., carbon does not tend to diffuse from one to another during heat treatment,

3. properly bonded, i.e., the interface must be sufficiently well bonded to prevent interface shear and thus maintain the same strain in the hard layer and the soft layer but the interface must be weak enough so that it will part during cracking and hence allow the softer layer to plastically deform.

The alloys presently in use are M4\* and PS4 developed within this project and melted by Armco Steel. Their compositions (nominal for M4 and actual for PS4) are given in Table III. PS4 was developed to match a slightly higher carbon high-speed steel and has a carbon activity some 20% higher than that of M4. Thus about 0.05 wt. pct. carbon transfer occurs from PS4 to M4 during the heat treatment of the present complexes. The interface zone is comprised of two sheets of AISI 310 stainless steel each of which has been carburized to the same carbon potential as the PS4. Each has also been preoxidized on one surface. The stainless surfaces facing PS4 and M4 are clean and the preoxidized surfaces abut. The entire zone has a thickness of about 5 pct. of the total of the hard and soft layer thickness, i.e., about 5 pct. of the repeat distance in the complex.

TABLE III. ALLOY COMPOSITIONS (wt. pct.)

Alloy	%C	% Co	% Cr	% Mo	% Ni	% V	% W
M4	1.35	--	4.25	4.50	--	4.00	5.75
PS4	.28	10	--	1.5	26	.5	--
310	C*	--	25	--	21	--	--

\*Carburized to activity of C in PS4.

\*Crucible Steel CPM M4.

The M4 steel was obtained in bars  $3/8" \times 1"$  ( $9.5\text{mm} \times 25\text{mm}$ ). For the manufacture of the complexes, the bars were protected in temporary stainless steel envelopes and rolled down to sheets of  $.020"$  ( $0.5\text{mm}$ ) thick at a temperature of about  $2100^{\circ}\text{F}$  ( $1150^{\circ}\text{C}$ ). The PS4 alloy had been cast in ingots of about  $1\ 1/4" \times 3" \times 10"$ . The ingot was cut and rolled down to sizes in a similar manner. According to manufacturer's instructions, the M4 steel was annealed after rolling by holding at  $1600^{\circ}\text{F}$  ( $870^{\circ}\text{C}$ ) for 2 hours and cooling at  $25^{\circ}\text{F}$  ( $14^{\circ}\text{C}$ ) per hour in the furnace to below  $1000^{\circ}\text{F}$  ( $540^{\circ}\text{C}$ ).

Hardening heat treatment of the complex is essentially the heat treatment for the M4 recommended by the manufacturer followed by a hardening and tempering treatment for PS4. It is shown in Fig. 33 and involves austenitizing at  $2175^{\circ}\text{F}$  ( $1190^{\circ}\text{C}$ ) for 2 minutes, quenching in oil and tempering at  $1000^{\circ}\text{F}$  ( $540^{\circ}\text{C}$ ) for two hours, cooling to  $149^{\circ}\text{F}$  ( $60^{\circ}\text{C}$ )\* and repeating this tempering treatment two more times (triple tempering). The PS4 alloy was then partially transformed to martensite and tempered for 30 min. at  $450^{\circ}\text{F}$  ( $230^{\circ}\text{C}$ ).

#### 4.2 Microstructure of the Complexes

Complexes were prepared from M4 hard layers, PS4 soft layers and 310 interface zones in a number of different layer configurations to exhibit the variation of fracture toughness with the prominent characteristics of the laminates, i.e., the fraction

---

\* The  $140^{\circ}\text{F}$  catch temperature prevented martensite function in the PS4 layers.

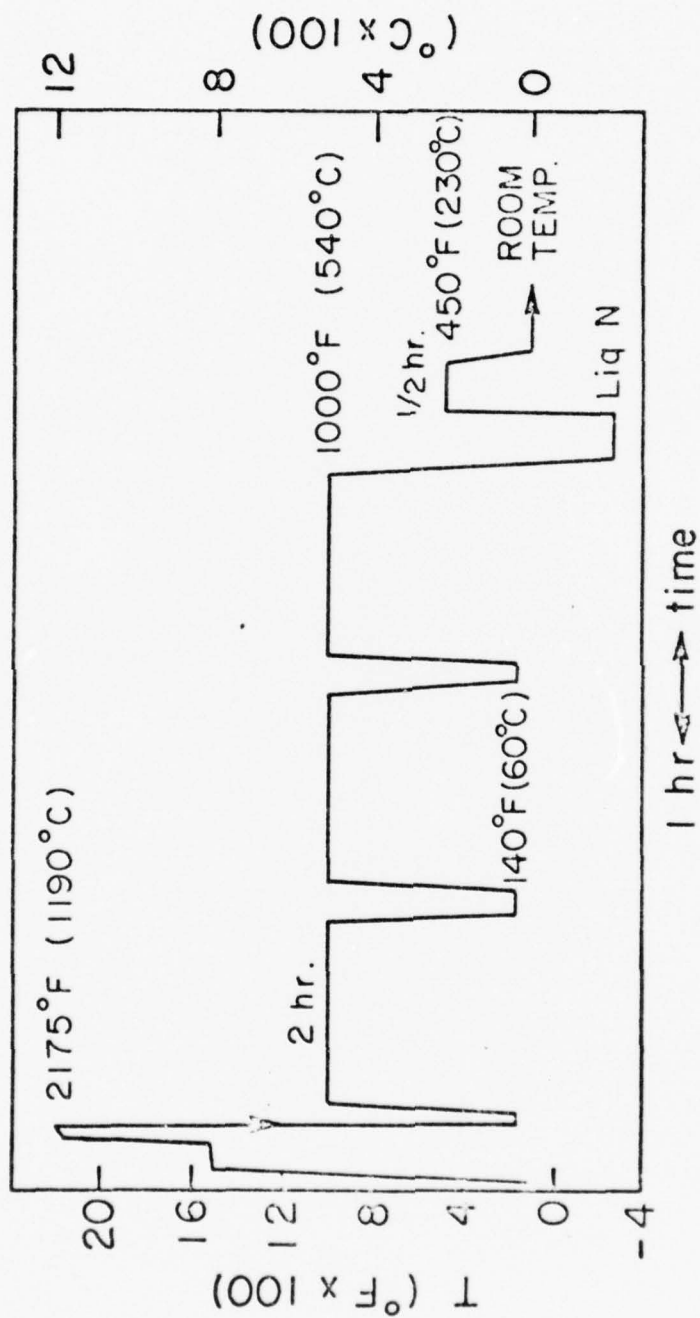


Fig. 33. Schematic Heat Treatment Schedule.

soft layer  $f_s$ , the repeat distance (width of a soft and a hard layer). Some complexes were prepared for tensile testing. The interface bonding was held essentially constant as was the interface zone geometry. The heat treatment previously described was applied to all samples except as noted. Fig. 34 shows the optical microstructure of the resulting complex. The liquid nitrogen quench has resulted in substantial martensite formation in the light PS4 layers and the dark M4 layers exhibit substantially complete transformation after triple tempering. The martensite in the dark (hard) layers is much finer than that in the PS4 and its plate shape is difficult to resolve after triple tempering. The PS4 etches rather lightly since its martensite has been tempered at only 450°F (230°C). The interface zone centers around the oxide bearing interface which is well marked by the fine dispersion of oxide particles. These are trapped at the abutting 310 stainless surfaces and they populate the surface along which parting occurs to allow the soft layer to behave ductilely.

To reduce the value of the interface bonding to a low level, two layers of stainless steel foils were introduced at the M4-PS4-interface. Each foil has only one side oxidized and these sides face each other while the unoxidized surfaces are facing the M4 or the PS4 surface. From past experience, the stainless-stainless surface should be easily debonded. Such an interface has been prepared and measurement of the interface bonding energy gives a lower value of about  $2.5 \times 10^5$  erg/cm<sup>2</sup>, indicating that the stainless-stainless interface has low bonding energy of about

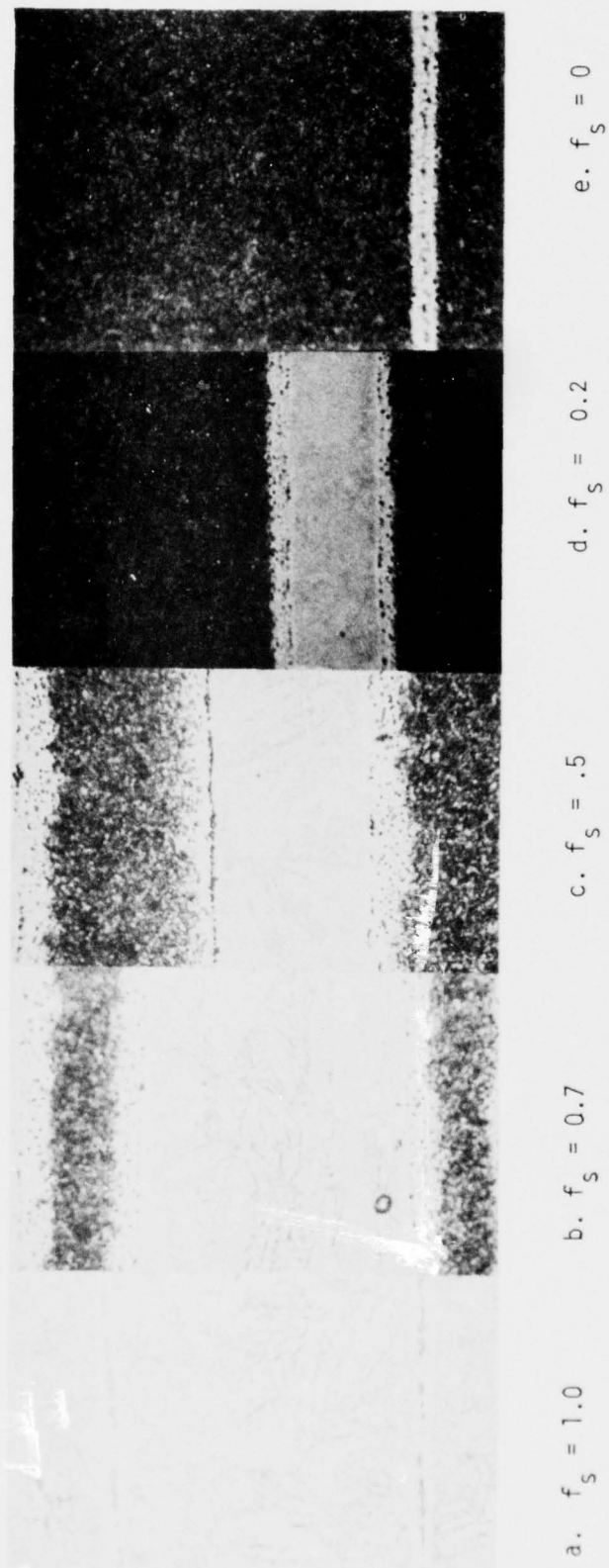


Fig. 34. Optical Microstructures of PS4-M4 Complexes for Fracture Toughness  $f_s$  Series. Fraction PS4 as indicated. The interface zone is shown with high austenite regions on both sides of the dark oxide-bearing interface. Nital Etch 256X.



half that used in the model system.

Several features of the interface and interface zone are of interest. As previously discussed and experimentally demonstrated, an interface with an effective  $K_{IC}$  of 15 ksi  $\sqrt{\text{in}}$  (16 GPa $\sqrt{\text{m}}$ ) or less is desired and the value is determined by interface chemistry and by annealing temperature and time, but not by rolling reduction. The preoxidized stainless steel foil interfaces appear to meet the requirement. In addition the zone has measurable width. As a result of required heat treatments, the interface is necessarily diffused so that the stainless layer is no longer distinct but a zone of altered chemical composition, structure, and mechanical properties is developed. Since many interfaces are present in the complex, the width of their zones is a significant variable. The zone and its width and the variation of width with treatment is discussed below.

Curves drawn through microprobe composition measurements are shown for a typical sample in Fig. 35. The zero distance is the center of the interface marked by oxide particles. Nickel and cobalt are diffused from the soft layer (S) into the hard layer (H). Cr is peaked at the interface where it was added in the stainless steel and has diffused into both layers. The microstructural effects of this is to:

1. Retain austenite in the adjoining region of the hard layer. Notice that Ni, Cr, and Co are all added to this region. These act in opposite ways on the activity coefficient of carbon so carbon content is little affected. Nickel and chromium both lower the  $M_s$  and their

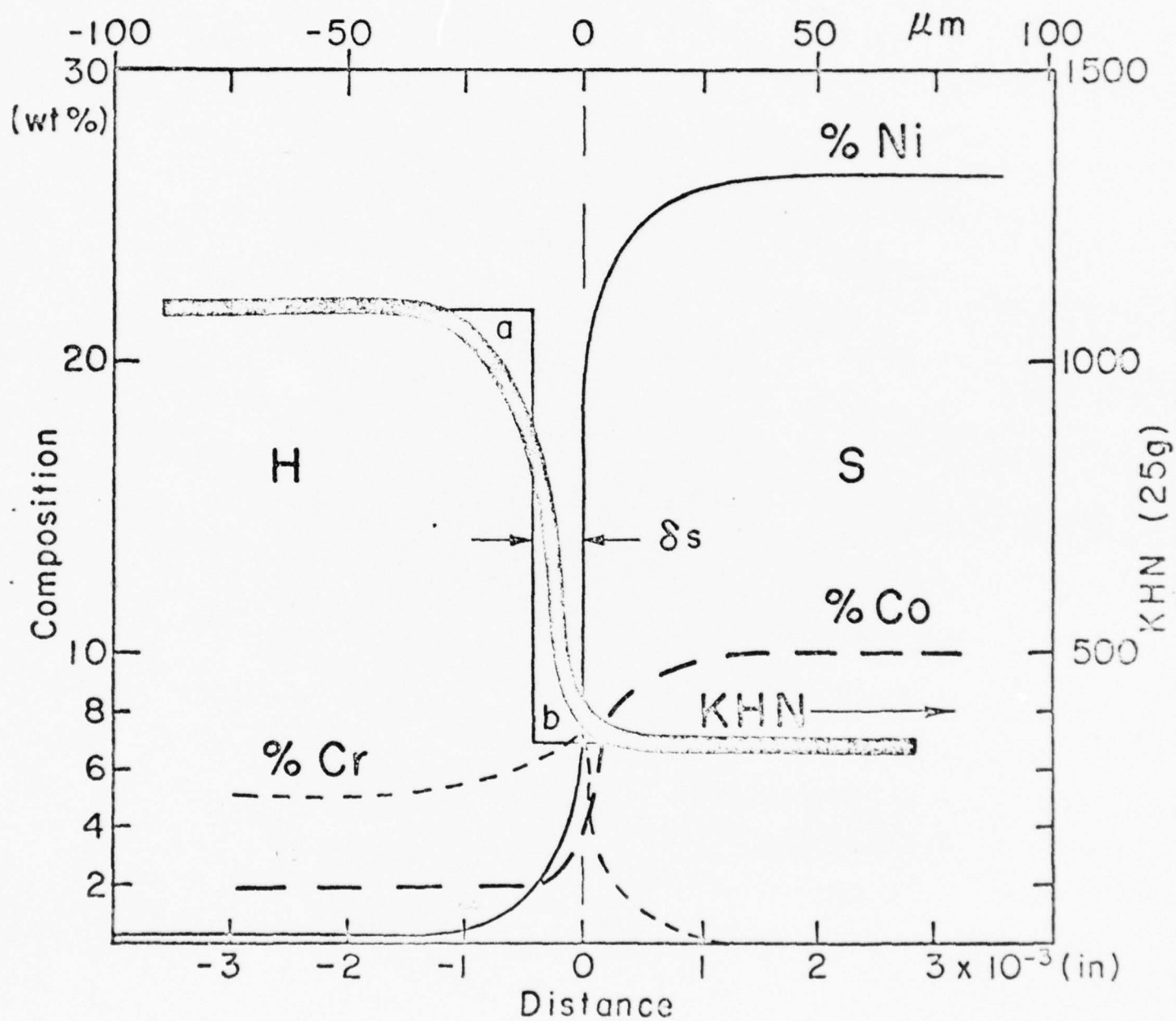


Fig. 35. Interface Zone. Ni, Co, and Cr Profiles from X-Ray Fluorescence Microprobe Analysis and Low Load (25g) Microhardness Profile.

combined effect is perceived to account for the retention of austenite in this region.

2. Stabilize austenite in the adjoining region of the soft layer. This region loses some nickel and cobalt and picks up some chromium. These affect the  $M_s$  in opposite ways but they all decrease the activity coefficient of carbon. Carbon thus probably becomes higher in this region and lowers the  $M_s$  causing complete austenite retention.

Also shown in Fig. 33 is the low load (25g) microhardness profile through the interface. (These hardness readings are much larger than those obtained at high loads and indicate only relative hardness, which suffices for present purposes). These hardness values indicate that the effective strength interface has been shifted 0.0004 in (10  $\mu$ m) into the hard layer to the position marked by the vertical line from b up to a. This line is positioned so that area a is equal to area b.

In summary, the two interface properties of primary interest are: interface zone thickness, in particular  $\delta s$  -- the effective shift into the hard layer and interface binding, the ability to release the soft layer so that its ductility can be utilized to stop crack propagation.

The above experimental results are for one sample and their use for other samples with different heat treatment and rolling reduction histories requires appropriate correction. In the course of processing the complexes, various heat treatments and rolling reductions are carried out. These effects are combined

to produce the interface zone. Since rolling is accomplished rapidly, diffusion occurs during the annealing periods and the effect of rolling is to alter the thickness. The final interface thickness is the combined effect of broadening by diffusion and reduction by rolling.

The combined effect can be calculated in the following way. The diffusion distance during the  $i^{\text{th}}$  annealing is  $\lambda_i = \sqrt{2D_i t_i}$  when  $D_i$  is the appropriate diffusivity at the annealing temperature and  $t_i$  is the annealing time. Following this anneal a thickness reduction  $r_i = h_i/h_{i+1}$  occurs and  $\lambda_i$  becomes  $r_i \lambda_i$ . The  $i+1$  anneal is then carried out with  $\lambda_{i+1} = \sqrt{2D_{i+1} t_{i+1}}$ . The distribution due to these two anneals is characterized by diffusion distance  $[(r_i \lambda_i)^2 + \lambda_{i+1}^2]^{1/2}$ . This may be combined with subsequent reductions until for all reductions, with  $R_i = \frac{h_{\text{final}}}{h_i}$ , one obtains

$$\lambda_{\text{final}} = \sqrt{\sum_{i=1}^N R_i^2 \lambda_i^2} = \sqrt{2} \sqrt{\sum_{i=1}^N R_i^2 D_i t_i} \quad (4.1)$$

#### 4.3 Mechanical Properties.

Two main types of mechanical property measurements were made, fracture toughness for cracks whose front is normal to the interlayer boundary plane (divider orientation) and tensile strength where the tensile axis lies in the laminate plane. The rolling direction was maintained parallel to the axis of tensile loading in both types of tests. The results of these tests show that the experimental material behaved consistently but did not approach the design levels of toughness or strength.

#### 4.3.1 Fracture Toughness Measurements.

In order to determine the behavior of various complexes, several variables were examined in the fracture toughness testing program. The fraction of the complex in the soft (PS4) layers, the thickness of the individual layers, and the thickness of the test sample, were individually varied. The manufacturing techniques and heat treatment were maintained constant as previously described.

The details of the testing procedures in general follow ASTM E 399-72 "Plain-Strain Fracture Toughness of Metallic Materials" with several exceptions dictated by the material. The compact fracture toughness specimen shown in Fig. 36 was used at thicknesses between .04 in (1mm) and .18 in (4.6mm). This thickness is sometimes less than that required by E399-72 and is smaller than W-a. The specimens were machined, in the annealed condition and then heat treated. The surfaces were ground and polished so that cracking could be observed under a metallurgical microscope. The specimens were fatigue cracked at controlled force at a frequency of 20 Hz a hydraulic testing machine.\* They were cycled between a minimal tensile load and a level which would produce  $K_I \cong 10 \text{ ksi}\sqrt{\text{in}}$  (11 MPa $\sqrt{\text{mm}}$ ). About  $10^5$  cycles were required to produce a fatigue crack about .050 in (1.2mm) long, the minimum crack length used. The specimens were tested in a screw driven tensile machine\*\* and the crack opening displacement

---

\* MTS machine in laboratory of Prof. Hillberry, Purdue Univ.  
\*\* Instron Model TTCL.

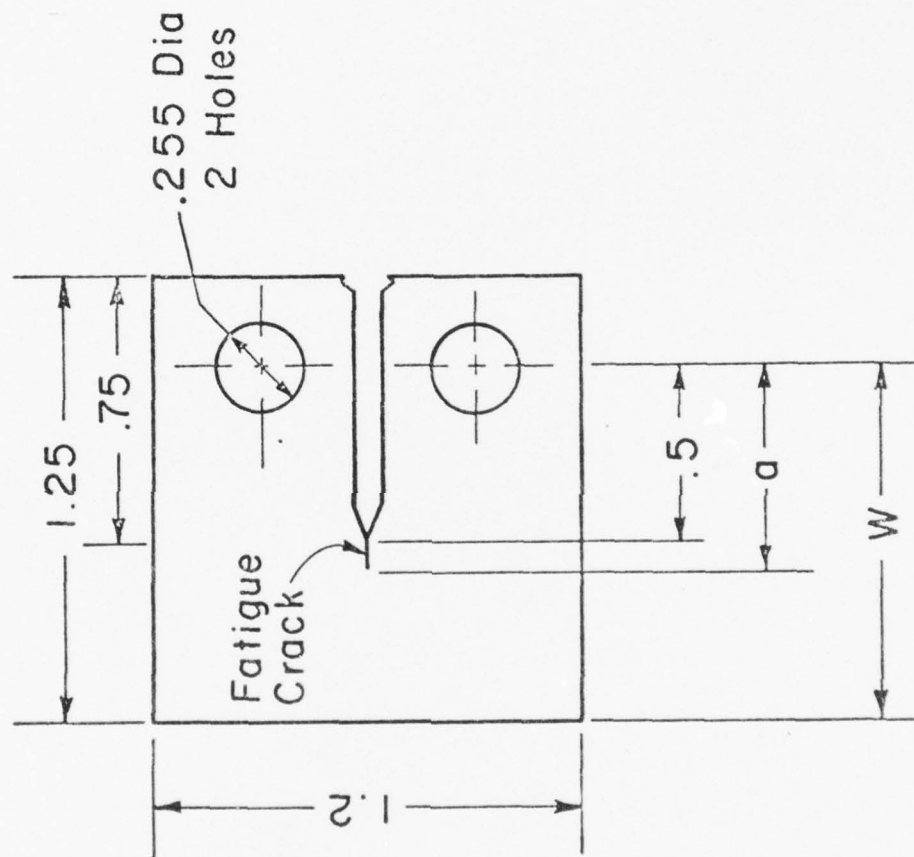


Fig. 36. Compact Fracture Toughness Specimen - Dimensions in Inches. The thickness varied from .04 to .18 in.



(COD) was measured with a standard clip-on gauge which had been calibrated with a mechanical extensometer. The force and COD were recorded. Fig. 37 is a copy of one such record for a sample 14 which had a thickness of 0.155 in. All curves were of this type (Type I according to E399). The  $K_I$  corresponding to the maximum force was found to be reproducible and correlatable material property. Its selection was dictated by the presumption that cracking would be occurring in all layers at this load. The downward part of the force displacement curve was commonly well defined and marked the continued propagation of the crack through the specimen width.

The resulting fractures macroscopically followed the plane defined by the notch and fatigue crack except for oscillations which gradually increased in amplitude as the fracture continued. A macrophotograph of the fracture of Sample 14 is shown in Fig. 38. The fatigue crack is the smoother region and the correlated waves in the hard layer fractures are readily seen under the oblique illumination. The soft layer fracture is straighter.

The  $K_I$  values corresponding to maximum load were calculated from that load,  $P$ , and the geometry (thickness,  $B$ , depth,  $W$ , and crack length,  $a$ ) of the sample according to

$$K_I = (P/BW^2)^{1/2} f(a/W) \quad (4.2)$$

where  $f(a/W)$  is given in E399 for compact specimens where  $a/W \cong .5$ . The  $B$  values for most samples (and all individual layers) were well below those required by E399 for calculation of a valid  $K_{IC}$  hence the values calculated are not so labeled. None the less they are shown to be relatively insensitive to specimen

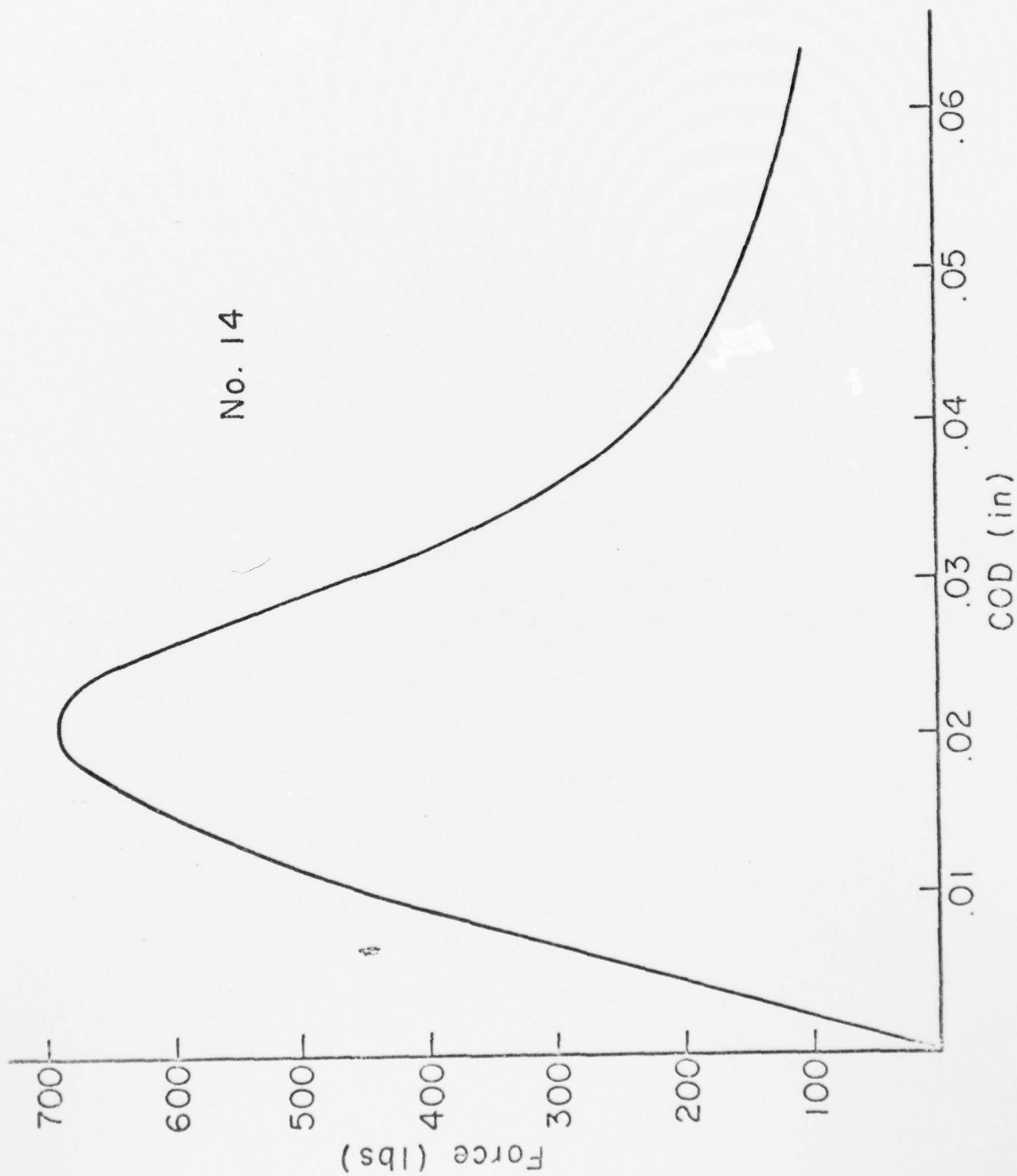


Fig. 37. A Typical Force VS. Crack Opening Displacement Record.

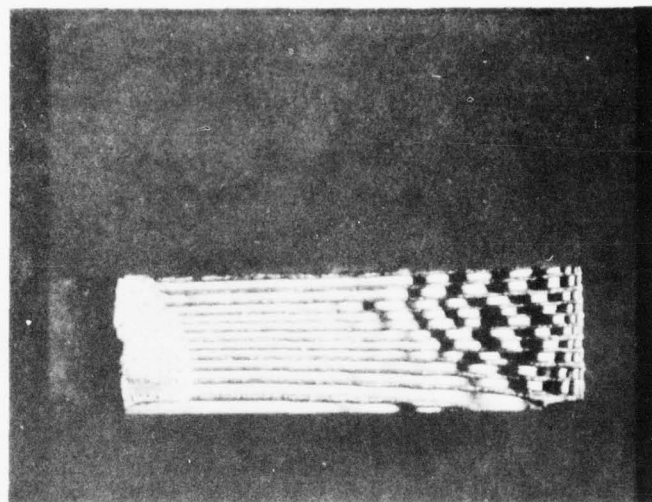


Fig. 38. Macrofractograph of Compact Fracture Toughness Specimen 14. Fatigue crack is on the left. Dark layers are PS4. Light layers are M4. Oblique illumination. 5X.

thickness and to correlate with the structure.

A series of samples was prepared and tested at various fractions of PS4. Maintained constant were the wavelength (total thickness of a typical soft and a typical hard layer) and the sample thickness.\* The results are shown in Fig. 39. The resulting straight line relationship shows that the observed maximum  $K_I$  values for laminates consisting of mixtures of soft and hard layers are approximately linearly related to similar properties of similarly laminated PS4 and M4.

Another series of samples was prepared and tested at various sample thicknesses with layer thickness and fraction soft (PS4) layer maintained constant. The fraction PS4,  $f_s$ , is such an important variable that the  $K_I$  values were all corrected from the measured  $f_s$  to  $f_s = .5$  using the measured  $f_s$  values and the slope of the line in Fig. 39. This correction was typically about  $3 \text{ ksi}\sqrt{\text{in}}$ . The resulting variation of  $K_I$  with  $B$  is shown in Fig. 40. The larger  $B$  values suffice to allow  $K_{IC}$  to be measured according to "plane strain" continuum theory for a homogeneous sample. We were surprised to see any dependence on  $B$  in these laminates.

A third series of samples was prepared and tested to show the effect of soft layer thickness on fracture toughness at fixed  $f_s = .5$  and  $B$ . Since the fraction soft layer is maintained constant, the soft layer thickness varies with the wavelength,  $\lambda$ . These wavelengths lie between .004 to .014 inch (.1 to .35mm) and plastic (plane stress) deformation of the soft layers, which are

---

\*  $\bar{\lambda} = .0092 \text{ in } (.23\text{mm})$ ,  $\bar{B} = .061 (1.56\text{mm})$ .

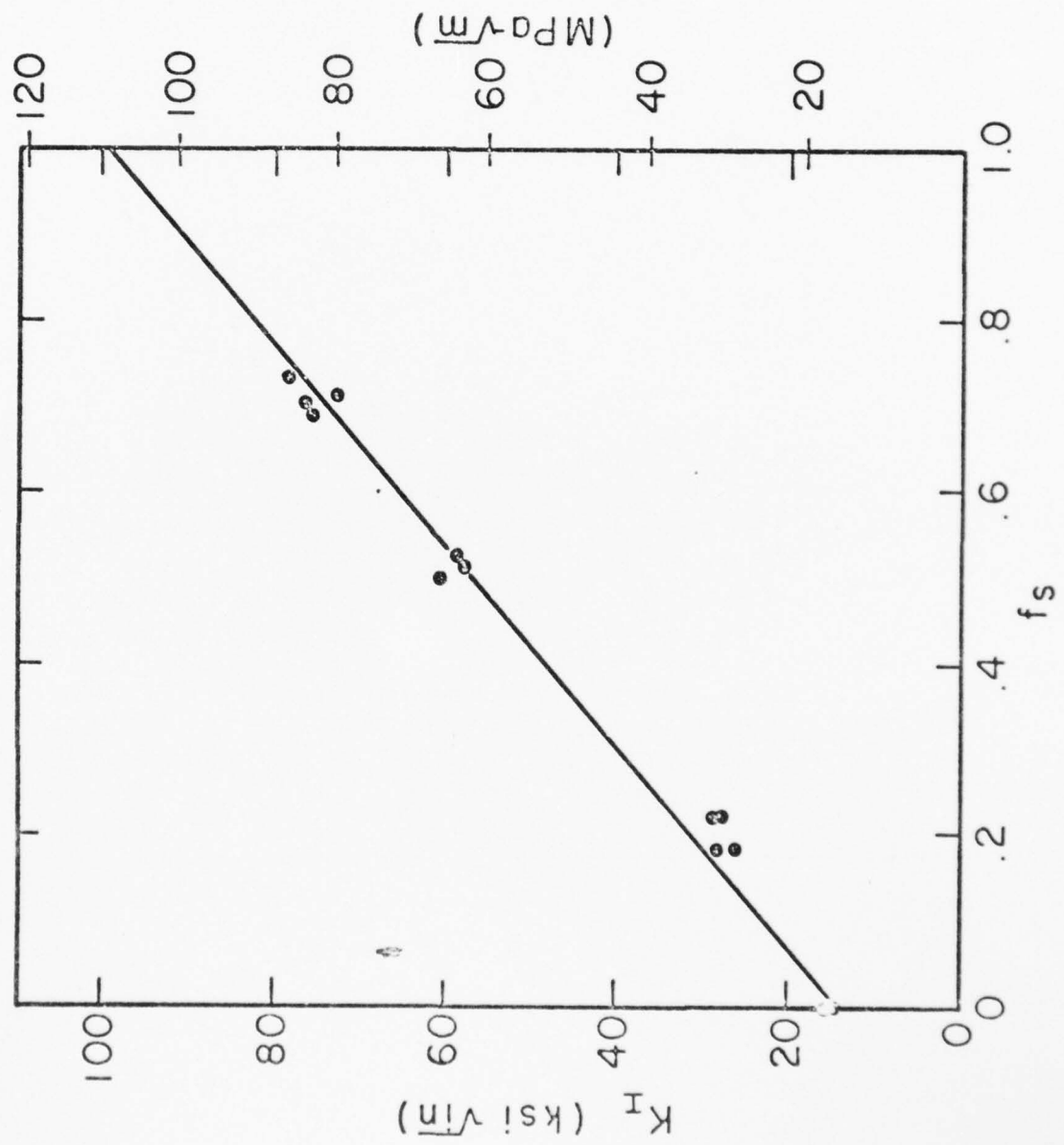
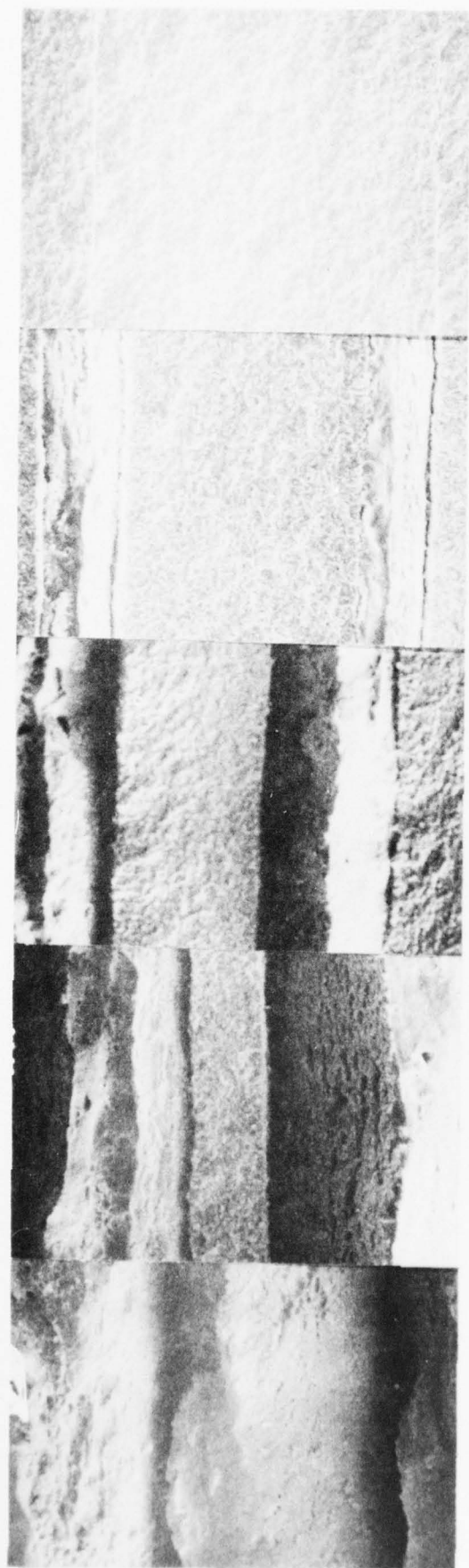


Fig. 39. Fracture Toughness of PS4-M4 Complexes with Constant Wavelength and Total Thickness.



a.  $f_s = 1.0$

b.  $f_s = .7$

c.  $f_s = .5$

d.  $f_s = .2$

e.  $f_s = 1.2$

Fig. 40. SEM Fractographs of PS4-M4 Complexes Broken in Fracture Toughness  $f_s$  Series. Fraction PS4 as indicated. Specimens are tilted so that the necked soft layers are light and dark depending on their angle and the brittle hard layers are a uniform mottled grey. 200X. Compare Fig. 3.



half these thicknesses, extends completely across these layers. The  $K_I$  values are shown as a function of  $\lambda$  in Fig. 41. The scatter is large and one possible curve through the points is drawn. The basis for the curve will be presented below.

The fractures of typical specimens in the  $f_s$  series were examined under the scanning electron microscope (SEM) and fractographs are shown in Fig. 42. These fractographs show that inter-layer parting occurred and (at higher magnification) that it occurred on the oxidized interfaces designed for it. Occasional chevron markings on the fractured hard layer indicate that the fractures went from right to left (as they did, in fact) in each sample. The areas photographed are near the start of the crack, i.e., within a few hundred microns of the fatigue cracked area. The fractographs can be readily compared with the microstructures shown in Fig. 34. Evidently the large plate martensite and retained austenite of the PS4 necked substantially during fracture. The diffused interface zone was essentially brittle on the M4 side of the oxide line and ductile on the PS4 side, Fig. 4, i.e., it behaved as a sharp line in the fracture process.

In order to correlate fracture toughness (or more precisely the  $K_I$  obtained from the maximum load), with the main structural parameters the relations postulated in the Design Rationale were used. These are rediscussed briefly below.

The energy to propagate fracture a unit distance is

$$BG = B(1-f_s)G_H + Bf_s G_s \quad (4.3)$$

when  $G = A K_I^2$ ,  $G_H = A K_{IH}^2$  for the hard (M4) layer in which A is

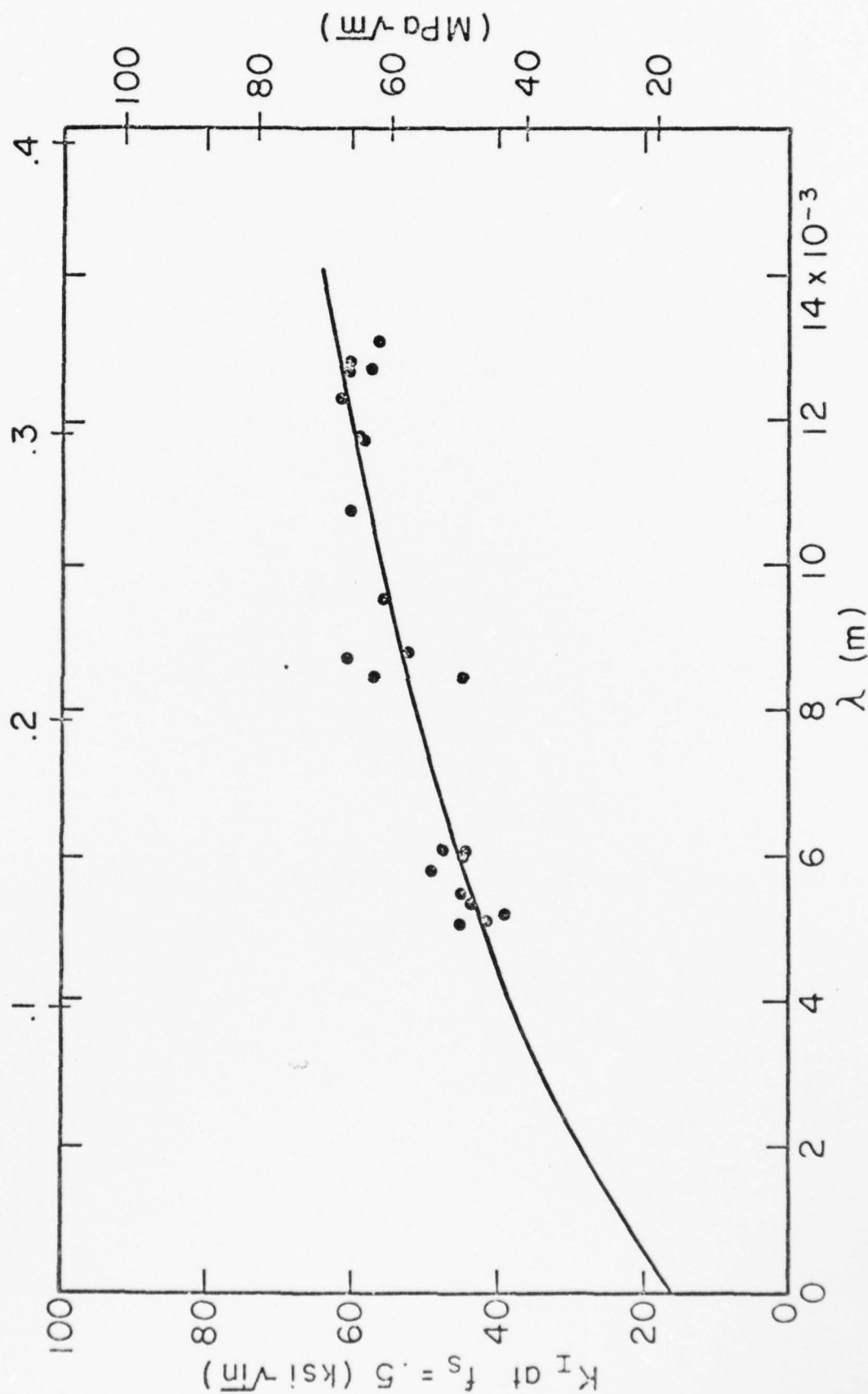


Fig. 41. The Wavelength Variation of Fracture Toughness in PS4-M4 Complexes at Constant  $f_s$  and B.

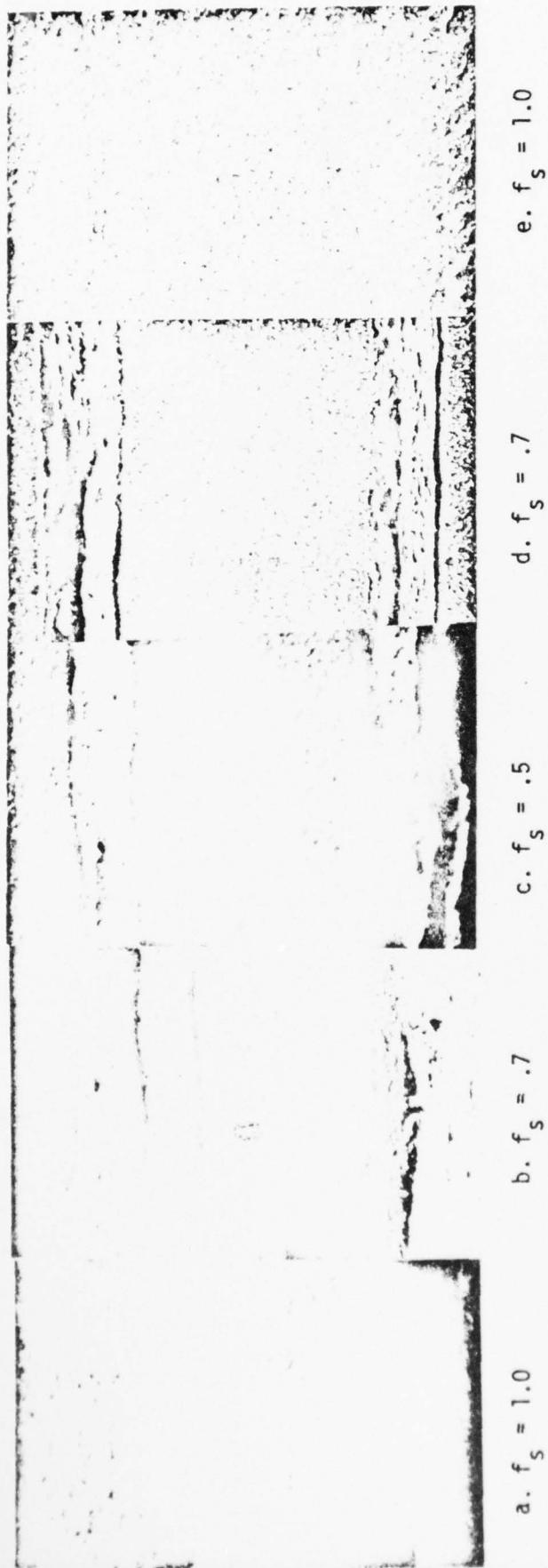


Fig. 42. SEM Fractographs of PS4-M4 Complexes Broken in Fracture Toughness  $f_s$  Series. Fraction PS4 as indicated. Specimens are tilted so that the necked soft layers are light and dark depending on their angle and the brittle hard layers are a uniform mottled grey. 200X. Compare Fig. 3.

a material elastic constant, and where  $Bf_s G_s$  is proportional to the square of the width of the soft (PS4) layer,  $W_s$ . This latter proportionality is postulated because necking is expected to produce severe plastic strain across each soft layer to a depth of  $W_s$  in each soft layer. This distortion is only possible if the interfaces part and remove the hydrostatic tensile stress component which would otherwise be applied to the soft layers by the undeformable hard layers. Such parting has been achieved. Thus,

$$f_s B G_s = CA \sum_{i=1}^{n_s} W_{si}^2 \approx \frac{CAB}{\lambda} (f_s \lambda)^2 \quad (4.4)$$

where  $\lambda = \bar{W}_s + \bar{W}_H$  is the repeat distance and CA is the proportionality constant.

Thus,

$$K_I^2 = K_{IH}^2 (1-f_s) + D f_s^2 \lambda \quad (4.5)$$

This equation is not precisely consistent with the linear variation of  $K_I$  with  $f_s$  shown in Fig. 39 but the required curvature of that line is not outside the scatter of the data. In Fig. 43 the  $K_I^2 - K_H^2 (1-f_s)$  from all tests were plotted versus the combined structural parameter  $f_s^2 \lambda$ . There is considerable scatter but as indicated above linear variation appears not unreasonable. The curve in Fig. 41 is drawn to fit the data using the above relations.

Thus the fracture toughness, the fracture appearance, and the microstructure appear to be reasonably correlated by the simple ideas previously proposed.

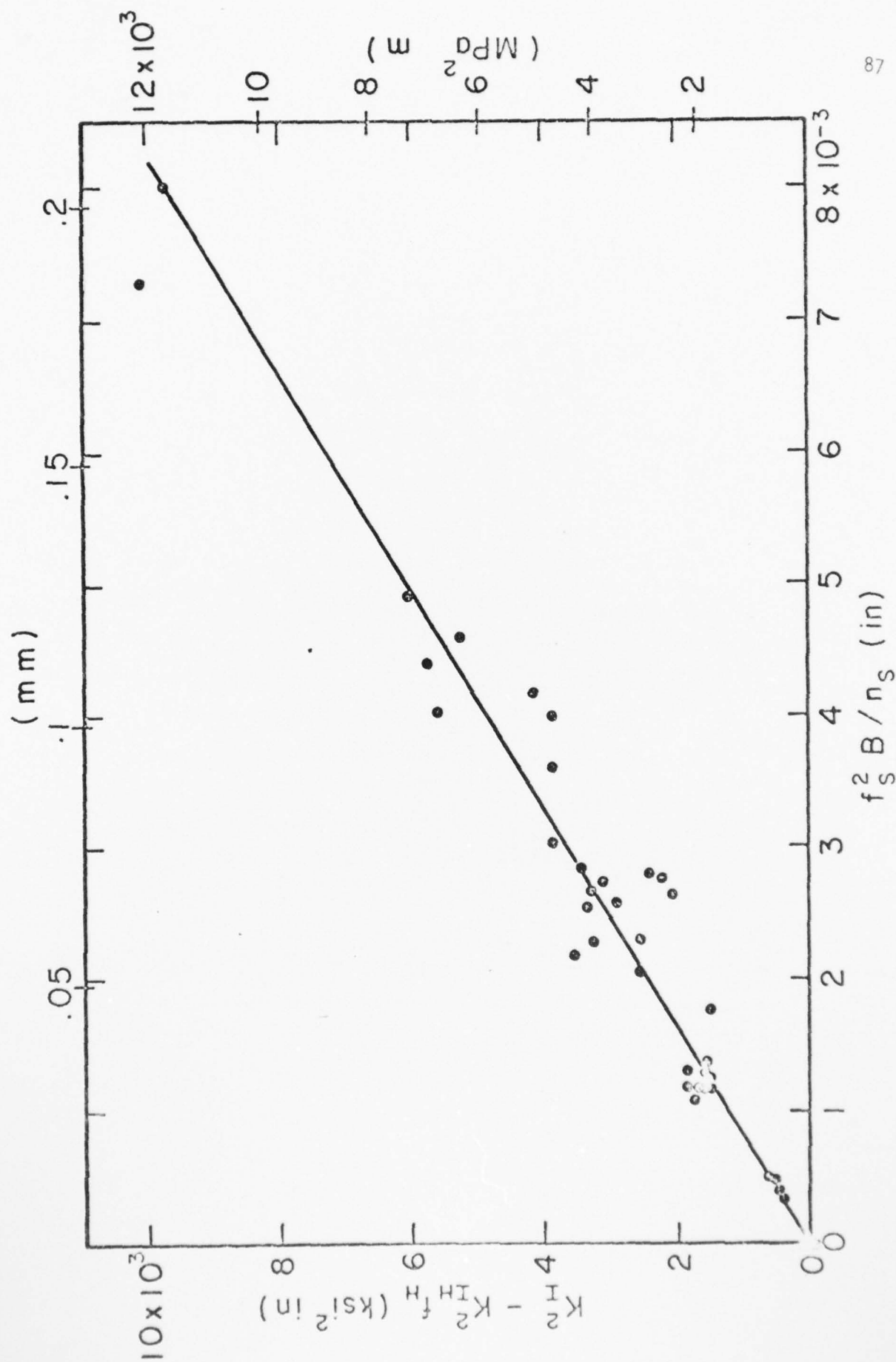


Fig. 43. Fracture Toughness Correlated with Microstructure.

#### 4.3.2 Tensile Tests.

Two tensile test programs were run. In the first program the heat treatment of the complex was varied and the strains were carefully measured so that the yielding and fracture behavior of the hard layer could be estimated. In the second program the heat treatment was fixed as previously given and the fracture stress was measured for several fractions of hard layer. This latter program was not completed because of funding limitations but nevertheless it yielded some pertinent results. .

In the first program tensile tests were conducted on specimens machined from annealed complexes which were subsequently heat-treated including triple tempering for two hours at a temperature between 600°F (315°C) and 1000°F (537°C). Between tempering the complexes were cooled to room temperature which allowed some martensite to form in the PS4 layers. This martensite was then tempered in the next tempering step. The specimen design is shown in Fig. 7. After heat treatment the specimens were ground smooth and for the higher tempering temperatures electropolished<sup>\*</sup> in and near the reduced section. After electropolishing the microstructure of both hard and soft layers could be seen on various parts of the surface and what few defects were observed did not correlate with the ultimate fracture locations.

Electric resistance strain gauges<sup>\*\*</sup> were attached directly to both sides of the test specimens and were read by Strain Gauge

---

<sup>\*</sup> Electropolish was 25bm CrO<sub>3</sub>, 7ml H<sub>2</sub>O, 133ml glacial acetic acid; 20V.

<sup>\*\*</sup> Type EA13 125BT-120 Micro-Measurements, Ramulus, Mich.



Indicator\* as the specimen was loaded in a testing machine\*\* which automatically recorded cross-head position. Cross-head position was used as the strain measurement for strains longer than 2 percent where the gauges failed.

Following fracture the bars were sectioned longitudinally and metallographically polished. The fraction hard layer was measured and corrected for the effective interface shift as discussed previously. Microhardness (KHN) of both hard and soft layers were determined at 500g load. These latter values are plotted versus tempering temperature with corresponding values for bulk samples of M4 and PS4 in Fig. 44. The Knoop hardness of the bulk M4 samples is not greatly different from that of the corresponding hard layers. A smooth curve with a minimum at 700°F (311°C) and a maximum at 830 KHN at 1050°F (565°C) is drawn through both these sets of points. The PS4 layers are slightly harder than the bulk PS4. This is probably because they contain some aged martensite as mentioned above. This martensite is not present in the bulk PS4 alloy. The horizontal line in Fig. 44 indicates the average hardness of the soft layers.

Four typical stress-strain curves are plotted in Fig. 45 as the solid lines. An approximate analysis of these stress-strain curves was carried out to indicate yield in the hard layer. In this analysis the observed amount of hard layer was assumed to be elastically strained according to its published modulus and the

---

\*Type N Baldwin - Lima - Hamilton - Waltham, Mass.  
\*\*Type TTC Instron Eng. Corp., Canton, Mass.

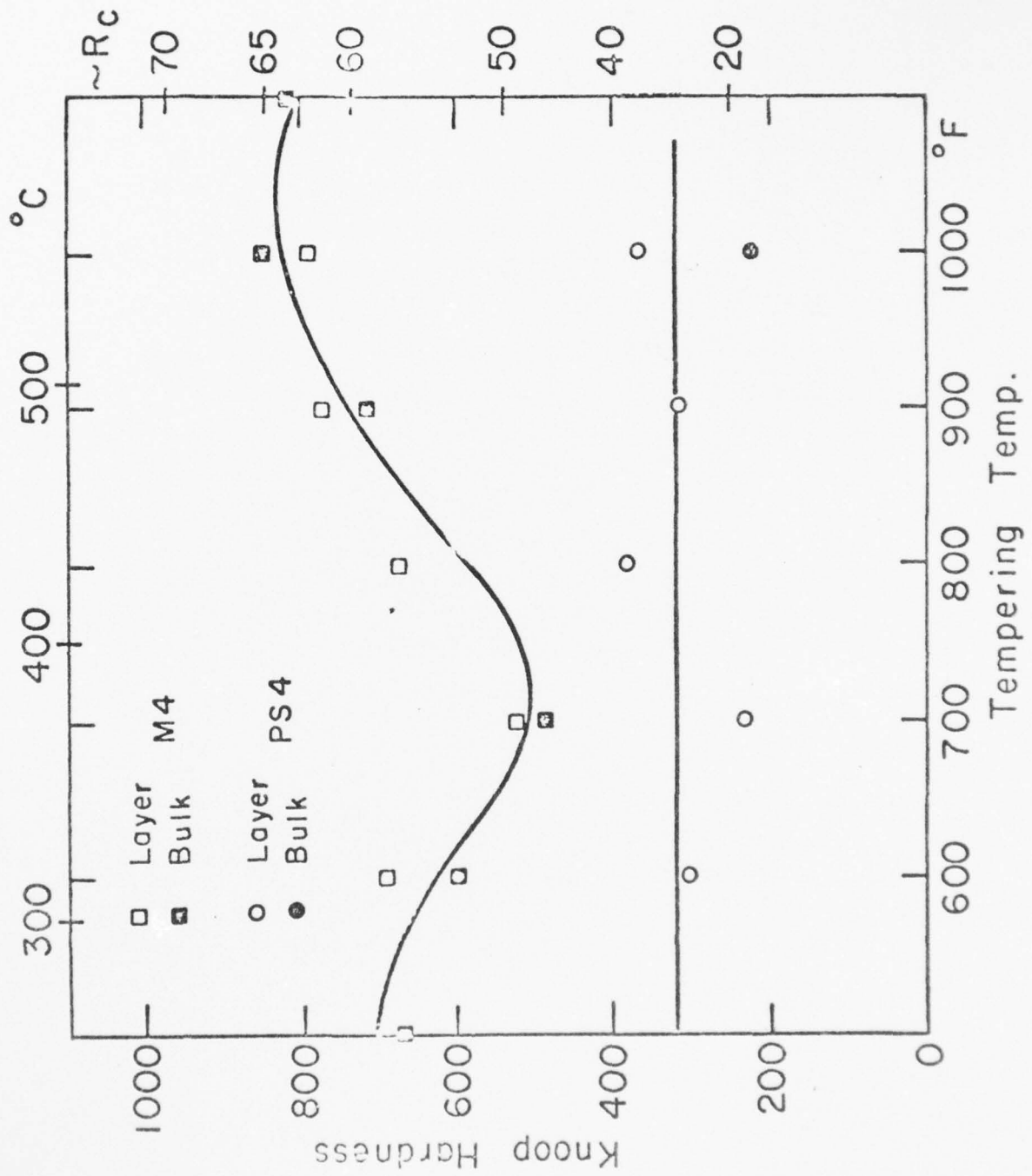


Fig. 86. Hardness (KHN) vs. Tempering Temperature for Hard Layers and Bulk M4 and for Soft Layers and Bulk PS4. Load 500g.

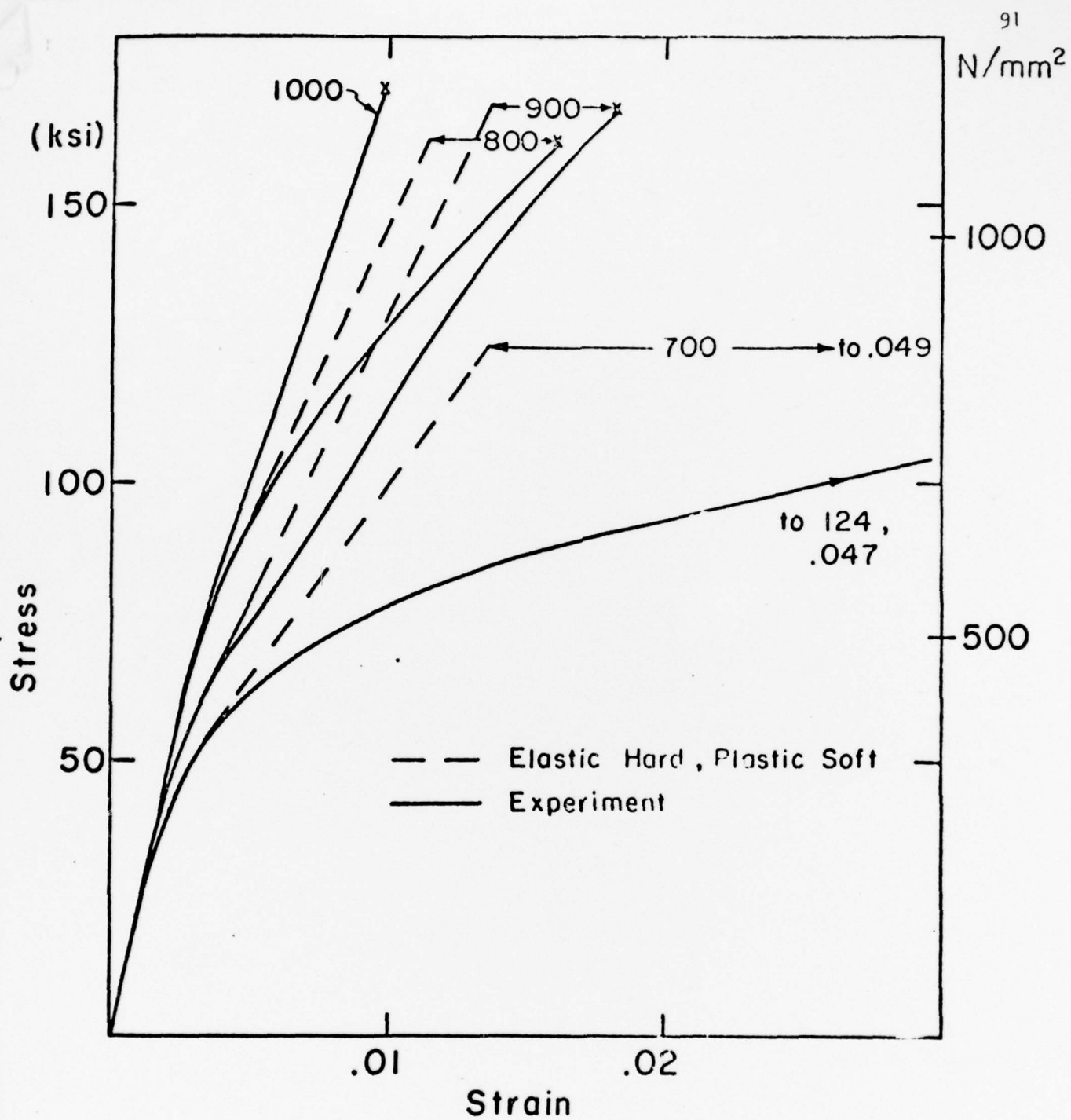


Fig. 45. Stress-Strain Curves for Four Specimens. The approximate elastic-plastic curves are given by the dashed lines. The solid lines are experimental.

soft layer was assumed to be ideally plastic at whatever stress was required to reproduce the "knee" in the stress-strain curves such as those for tempering at 700, 800, and 900 in Fig. 44. These constant stresses superimposed on the elastic stress in the hard layer produced the dashed elastic-plastic curves in Fig. 45. At any stress, deviation toward larger strain corresponds to plastic strain in the hard layer. The stress for 0.2 percent strain deviation was measured and the force provided by the soft layer was subtracted. The remaining force divided by the area of hard layer is taken to be the yield strength of the hard layer. A similar analysis at fracture gave the fracture stress.

Although such analysis produced fairly consistent results in 600, 700, 800, and 900°F tempered samples, those tempered at 1000°F indicated very rapid hardening of the soft layer (or else division of the soft layer into a hard and a soft constituent) and could not be analyzed in this way. This approximate analysis should err in the direction of underestimating the stress in the soft layer and hence overestimating the strengths of the hard layer. Table IV gives the results of this analysis. The hard layer yield strengths and fracture strengths (except for the 1000°F tempered samples which could not be analysed) show considerable scatter but the magnitudes agree satisfactorily with the "rule of thumb" that hardness is twice tensile strength and three times yield strength. The amount of plastic strain in the hard layer is also derived from this simple analysis and it appears to be sufficient to allow satisfactory testing.

In the second series of tensile tests the standard tempering

TABLE IV. Approximate Yield Behavior of the Layers in Tempered Complexes of M4 and PS4.

Tempering Temperature (°F)	Fraction Hard Layer	Soft Layer Yield Stress (ksi)	Hard Layer Yield Stress (0.2%) (ksi)	Hard Layer Fracture Stress (ksi)	Plastic Strain in Hard Layer at Fracture (%)
600	.38	45	210	270	1.5
700	.28	36	190	380	2.9
800	.33	65	280	350	.5
900	.37	41	280	350	.4
1000	.37	--	--	--	--

Values are averages of two tests.



treatment at 1000°F (540°C) was used followed by subcooling and tempering at 450°F (230°C) as illustrated in Fig. 38. The hardness of layers of M4 and PS4 subjected to such treatment was 874 KHN for the M4 and 327 KHN for the PS4. The fracture stress was measured on tensile bars like those in Fig. 7 except that the center  $\frac{1}{2}$  inch long part of the reduced section was further reduced to 0.1 in (2.5mm). As previously determined very little plastic deformation occurs in these samples. The results of the tensile tests in this incomplete series are shown in Fig. 46. The straight line illustrates the law of mixtures applied to the strength estimated from the hardness values of the individual layers and the points are not inconsistent with this line up to about 50% hard layer. About this value the observed fracture strength drops off. This is the behavior which was observed in the model system and which had been predicted as due to elastic crack jumping across the soft layers.

#### 4.4 Conclusions.

1. On the basis of the limited data obtained, the tensile strength of the M4/PS4 complexes appeared to follow the behavior expected, i.e., a linear increase in strength with fraction hard layer up to about 50% hard layer with no significant increase in strength beyond that fraction. This puts the maximum strength at about 275 ksi (1.9 GPa) which is substantially less than the design goal for 400 ksi (2.8 GPa).
2. The fracture toughness of the M4/PS4 complexes with constant modulation repeat distance has been found to vary linearly with fraction soft layer. This law of mixtures is hypothesized as



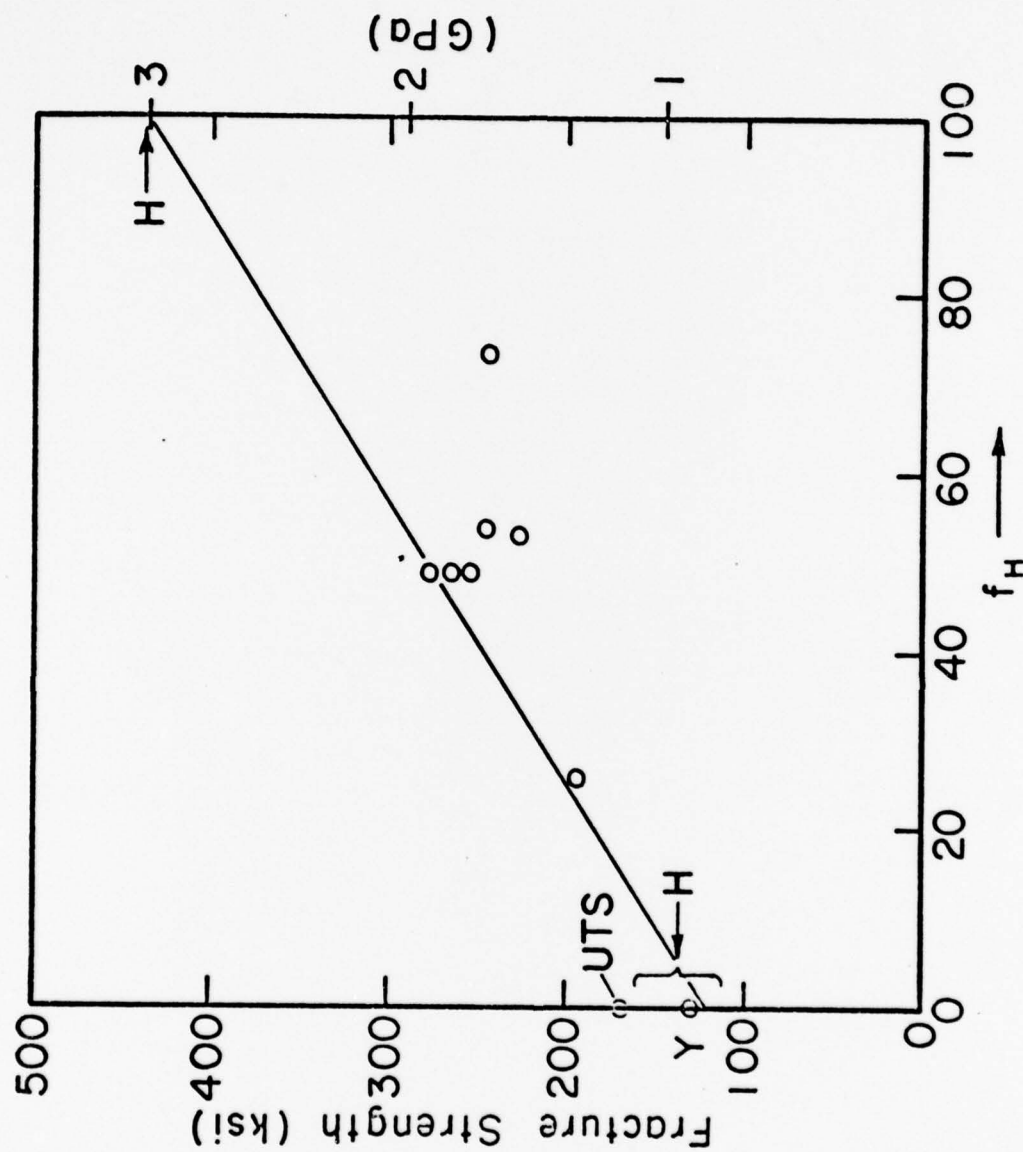


Fig. 46. Tensile Strength of PS4-M4 Complexes Given the Standard Heat Treatment. H shows the strength expected from the observed hardness of the individual layers.

due to the combined effect of the increase in the amount of soft layer and the increase in the width of the soft layer. The fracture toughness of the 50-50 M4/PS4 complexes is about  $60 \text{ ksi}\sqrt{\text{in}}$  ( $65 \text{ MPa}\sqrt{\text{m}}$ ) which is substantially less than the design goal of 100 to 150  $\text{ksi}\sqrt{\text{in}}$  (110 to 165  $\text{MPa}\sqrt{\text{m}}$ ).

3. The consistent and understandable behavior of the complexes which have sufficiently weakly bonded layers is a significant accomplishment of the project. The fact that the complexes do not achieve the design goals is a notable failure of the project. This appears to be due to the extreme brittleness of the hard layers at maximum hardness which forced the use of lower hardness levels in the hard layer. Had the strength been available in the hard layers, the fracture toughness of the complex could have been increased by adjustment of wavelength.

#### V. ACKNOWLEDGEMENTS

This work was supported financially by the Advanced Research Projects Agency of the Department of Defense. The PS2 alloy was melted and cast in the crystal growing laboratory at Purdue University in cooperation with Dr. Harold Harrison. The PS4 alloy was specially melted, cast, donated by the Research Laboratory of Armco Steel Co., Middletown, Ohio. Technical support was supplied by Mr. Arnold Wilson, Mr. Robert Staley, and Mr. David McCabe. Fatigue cracks were developed in fracture toughness specimens in the laboratory of Professor B. Hillberry, Purdue University.

The investigators acknowledge with thanks the above support.

## VI. REFERENCES

1. Argon, A. S., Treatise on Materials Science, 1 (1972) 79-114.
2. Clausing, D. P., Int. J. of Fract. Mech. 6 (1970) 71-85.
3. Wada, T., Wada, H., Elliott, J. F., and Chipman, J., Met. Trans. 2 (1971) 2199-2208.
4. Smith, R. P., Trans. Met. Soc. AIME 233 (1965) 397-401.
5. Zackay, V. F., J. Iron and Steel Inst., 207 (1969) 896-901.
6. Gergerich, W. W., Hemings, P. L., Zackay, V. F. and Parker, E. R., Fracture (1969), Ed., Pratt, P. L., Chapman Hall, Lond.
7. Gilman, J. J., J. Appl. Phys., 31, (1960) 2208-2218.

## TASK II

CATALYTIC PROPERTIES OF SURFACE SITES ON METALS  
AND METAL OXIDES AND THEIR CHARACTERIZATION  
BY X-RAY PHOTOELECTRON SPECTROSCOPY

Program Manager: R. G. Squires (317)749-2489

Project Scientists: L. F. Albright (317)749-2489

W. N. Delgass (317)749-2238

R. A. Walton (317)494-8292

N. Winograd (317)494-8126

Catalytic Properties of Surface Sites on Metals  
and Metal Oxides and Their Characterization  
by X-Ray Photoelectron Spectroscopy

SUMMARY

A. Technical Problem

The long range objective of this research program is to modify the distribution of oxidation states which are stable at the surface of a metal oxide catalyst by controlling the dispersion of the catalyst on its inert support. The catalytic activity and selectivity of the catalyst will then be correlated against the oxidation state of the surface sites -- which will be measured using x-ray photoelectron spectroscopy.

This technique has general applicability to a large number of catalyst systems. The scope of our research has been expanded to include the study of selective hydrocarbon synthesis from CO and H<sub>2</sub> over supported bimetallic cluster catalysts. The synthesis reaction is central to production of clean fuel and substitute petrochemical feedstocks from coal.

B. General Methodology

The catalytic activity and selectivity of many catalysts can be varied by controlling the oxidation state of the surface oxide. The development of techniques to control and to measure the surface oxidation state (or states) would make possible novel catalysts with enhanced activity and/or dual site catalysts with unique selectivity properties.

Three methods of controlling the surface states will be investigated. (A) The dispersion of the active catalysts on an inactive support will be varied in hopes that the stable oxidation state at given ambient conditions will be influenced by the degree of dispersion of the catalysts. (B) The



chemical composition of bimetallic cluster catalysts will be systematically varied and correlated with the corresponding catalytic reactivity and selectivity for hydrocarbon synthesis. (C) Reactions at electrode surfaces will be studied in hopes that controlled potentials applied to the electrode will influence the oxidation state of the surface sites.

The success of these techniques will be determined by measuring the catalytic activity and selectivity of various reactions on the oxide catalysts and measuring the resulting surface oxides formed by x-ray photoelectron spectroscopy (ESCA). ESCA is a tool uniquely suited to this research since it can measure the oxidation state and chemical composition of surface species.

#### C. Technical Results

##### (1) CO and NO reactions on chromia supported on silica:

The first phase of our study of CO and NO reactions on chromia has been completed and a paper describing the results was presented at the Sixth International Congress on Catalysis, London, England, July 12-16, 1976. A brief summary of the work is given below.

Infrared spectroscopy has been used to observe the surface species on a chromia-silica catalyst during the reduction of nitric oxide by carbon monoxide. Spectra taken during the reaction (250 - 300°C) show that the catalyst surface is predominantly covered with chemisorbed nitric oxide species. Stable carbonates are also observed, but chemisorbed carbon monoxide and nitrous oxide are not observed.

The catalyst activity can be correlated with the concentration of an active surface species of nitric oxide, probably a dinitrosyl complex, having



an infrared absorption band at  $1735\text{ cm}^{-1}$ . The rate expression of carbon dioxide formation was found to be:

$$r_{\text{CO}_2} = K_2' P_{\text{CO}} \log (I_0/I) 1735\text{ cm}^{-1}$$

Nitric oxide was reduced to nitrous oxide and lesser amounts of  $\text{N}_2$ . The two parameter reaction model proposed gives a remarkably good fit to both the rate of reaction as a function of  $\log (I_0/I)$  and selectivity of the products as a function of  $P_{\text{CO}}$ .

## (2) Hydrocarbon synthesis over Bimetallic Clusters

Initial work in this area concered development of techniques for the use of quadrupole mass spectrometry to follow the CO methanation reaction. Although care must be taken to insure operation of the mass spectrometer in a pressure region where the response is linear, the application of this analytical tool was successful for both steady state and transient operation of the differential chemical reactor.

Results for Fe-Ru/ $\text{SiO}_2$  catalysts showed clearly that the kinetic behavior of the mixed metal catalyst was significantly different from that of Ru/ $\text{SiO}_2$  and Fe/ $\text{SiO}_2$ . These data, together with Mössbauer spectroscopic evidence, show conclusively that multimetallic clusters of Fe and Ru are formed on  $\text{SiO}_2$  and that the selectivity of the catalyst is changed as a result.

The fast response time of the mass spectrometer together with its capability for repetitive scanning made it possible to study the response of the reaction to step changes in CO concentration. In such experiments over 0.5% Ru/ $\text{Al}_2\text{O}_3$  a step input of CO into flowing  $\text{H}_2$  caused the rate to

go through a maximum 6 - 8 times greater than the steady state rate. It is most likely that this phenomenon is caused by the high  $H_2/CO$  ratio in the adsorbed gas layer on the catalyst surface although some thermal enhancement due to the high rate of heat generation when the reaction rate increases cannot be ruled out.

### (3) Characterization of Surfaces by ESCA

Our proposed research encompasses the continuing development of electron spectroscopy (ESCA) as a technique to determine surface chemical structure as it relates to heterogeneous catalytic and electrochemical reaction mechanisms. We feel very strongly that one of the primary advantages of the ESCA technique is that useable data can be obtained not only on "clean" systems prepared at  $10^{-10}$  torr but also on "dirty" systems prepared under reaction conditions, such as the chromia/silica catalyst system. The possibility of "bridging the gap" between these two situations is most exciting to researchers in the catalysis field.

A number of important results have been obtained recently. Studies of the effects of adsorbed gases on clean metal surfaces have been extended to Cd and Ag. For the Cd system, the  $O(1s)$  binding energies for  $CdO$ ,  $Cd(OH)_2$ ,  $CdCO_3$ , and  $CdO_2$  have been characterized and have been used to follow the decomposition of these species as a function of temperature.  $CdO$  and one additional oxygen state were found on oxygen-exposed Cd films. In the Ag system the  $O(1s)$  binding energies have been reported for  $AgO$ ,  $Ag_2O$ , and  $Ag_2CO_3$ . Contamination of the Ag surface by carbonate was found to be an important complication in interpretation of oxides prepared in air. No

oxide phases were seen on oxygen-exposed Ag films.

Other accomplishments include a theory for predicting Auger energies using ESCA binding energies, and the discovery that PbO surfaces are markedly reduced by  $H_2^+$ ,  $Ne^+$  and  $Ar^+$  bombardment at 400 eV but not by  $Xe^+$  and  $Kr^+$ . The former result is important because it advances the understanding of the role of electron relaxation in determining Auger energies. The latter result shows that some ion/surface techniques for surface analysis, particularly ion scattering spectrometry, may annihilate the chemical character of surfaces they analyze.

Attention has also been directed toward Pt electrode and supported chromia catalyst surfaces. The initial oxidation product of potentiostatic oxidation in 0.2M  $HClO_4$  was found to be  $Pt^{2+}$  while galvanostatic oxidation in  $HClO_4$  or  $H_2SO_4$  produced  $PtO_2 \cdot H_2O$ . ESCA chemical shifts showed the metallic and surface nature of Cu and Ag deposited on Pt by underpotential deposition.

Studies of  $Cr/SiO_2$  catalysts as a function of calcination temperature and heating in CO and NO have yielded both chemical and structural information. While  $Cr^{6+}$  predominated in freshly prepared catalysts, calcination at 500°C converted the chromium to  $Cr^{3+}$ . A remarkable redispersion of the chromium was seen in a narrow temperature region around 500°C. This was evidenced by a sharp increase in the  $Cr(2p_{3/2})/Si(2p)$  intensity ratios. Reaction of the catalyst with CO or NO at 300°C for three hours produced  $Cr^{2+}$ , with a greater degree of reduction on CO.

#### (4) Electrode Reaction Studies

The main objective of this experimental investigation is to clarify the phenomena that occur at or close to the surface of electrodes used in hydrogen-oxygen fuel cells when dilute solutions of KOH or sulfuric acid are used as electrolytes. Studies to date have resulted in the following conclusions:

- 1) Steady-state meniscus currents vary significantly with the concentrations of either the KOH or sulfuric acid electrolytes.
- 2) The temperature at which a cell operates also affects physical properties of the electrolytes and the intrinsic kinetics of the electrochemical steps.
- 3) A key to interpreting the cathodic behavior may be analysis of surface oxides.

ESCA studies of the electrode surfaces have centered on the cathode. The oxygen in the Pt electrode has been followed during activation, start-up, and steady-state fuel cell operation by recording the  $O(1s)/Pt(4f)$  ESCA intensity ratios. The large current fluxes noted at start-up have been found to be associated with high oxygen coverage of the electrode surface.

#### D. Implications for Further Research

Studies on the  $Cr/SiO_2$  catalyst system will continue. Kinetic data in a wide temperature range will be taken to determine activation energies and compare to the model. Isotope studies will be made using IR at reaction conditions to further define and identify the catalytically important surface species.

The main objective of the hydrocarbon synthesis over bimetallic clusters for the next several months will be to obtain kinetic, chemisorption, and, where appropriate, Mössbauer results for the catalysts already prepared. This work will be guided by preliminary screening of the catalysts to see which have the highest yields of higher hydrocarbons. Further development of methods for insuring cluster formation and observing promoter effects will be aided by Mössbauer and ESCA studies. The IR system is now being modified to allow detailed study of the effects of the best catalysts on reaction intermediates. These results will be used as the basis for attempts to further control and improve catalyst selectivity and activity. Thus, we plan to apply the ESCA technique to the characterization of samples more directly related to the actual environment of the catalyst or the electrode. This second phase includes the correlation of the steady state surface behavior as observed by XPS with any catalytic activity. In addition, we plan to study reactions of unusual importance to fuel cell technology and to fundamental corrosion mechanisms. Emphasis will be placed on systems which affect the electrode surface, such as oxidation and adsorption processes, so that the chemical structure of products can be determined.

Paralleling these studies will be further fundamental studies of gas/surface interactions and the interpretation of ESCA data, and an attempt to correlate the changes in metal core binding energies with change in oxidation state for derivatives of certain key metals which show catalytic activity. Included in our studies will be derivatives of rhodium, rhenium, ruthenium, and molybdenum, all of which find use as important components for certain heterogeneous catalysts.



Additional analyses will be made of Pt cathodes in order to clarify how the surface oxides change with time of operation of the cathode, and with the location of the site on the cathode relative to the meniscus. Additional data need to be obtained to clarify further the complicated relationship between the several factors that control the levels of currents generated.



## I. Introduction

The catalytic activity and selectivity of many oxide catalysts can be varied by controlling the oxidation state of the surface oxide. The development of techniques to control and to measure the surface oxidation state (or states) would make possible novel catalysts with enhanced activity and/or dual site catalysts with unique selectivity properties.

Two methods of controlling the surface states will be investigated: a) the Dispersion of the active catalysts on an inactive support will be varied in hopes that the stable oxidation state or active site at given ambient conditions will be influenced by the particle size or composition of the active phase of the catalysts. (b) Reactions at electrode surfaces will be studied in hopes that controlled potentials applied to the electrode will influence the oxidation state of the surface sites.

The success of these techniques will be determined by measuring the catalytic activity and selectivity of various reactions on the oxide or supported metal catalysts and measuring the resulting surface oxides or metal phases formed by x-ray photoelectron spectroscopy (XPS or ESCA) and where applicable, Mössbauer spectroscopy.

The following report will be divided into three sections:

- (II) Catalytic Studies,
- (III) Characterization of Surface States by ESCA, and
- (IV) Electrode Reaction Studies.

## II. Catalytic Studies

R. G. Squires

School of Chemical Engineering

W. N. Delgass

School of Chemical Engineering

### A. Objective

The long range objective of this research program has been to modify the distribution of oxidation states which are stable at the surface of a metal oxide catalyst by controlling the dispersion of the catalyst on its inert support. The catalytic activity and selectivity of the catalyst were then correlated against the oxidation state of the surface sites--which were measured using x-ray photoelectron spectroscopy.

This technique obviously has general applicability to a large number of catalytic systems--an even larger number than might first come to mind since many "metal" catalysts are, in their active state, covered by an oxide layer which is the active species.

#### (1) CO and NO reactions on chromina supported on silica:

The aim of this research was to correlate measured reaction rates with the concentration of catalytically active surface species, as measured at reaction conditions by infrared spectroscopy. The surface species on a chromia silica catalyst has been observed during the reduction of nitric oxide by carbon monoxide.

(2) Hydrocarbon synthesis over bimetallic metal clusters: In the course of development of concepts and methodology for characterizing catalysts and understanding the chemical origin of catalytic activity, we have expanded the scope of our research to include investigation of the catalysis by metals. The new research area is the study of selective hydrocarbon synthesis from CO and H<sub>2</sub> over supported bimetallic cluster catalysts. The synthesis reaction

is central to production of clean fuel and substitute petro-chemical feedstocks from coal. Specific objectives include development of catalysts with high activity for synthesis of specific low molecular weight hydrocarbons, study of chemisorbed species present on selected bimetallic cluster catalyst surfaces during the synthesis reaction, and improvement of ESCA as a quantitative tool for analyzing this new and important class of catalysts.

#### B. Background and Technical Need

(1) CO and NO reactions on chromia supported on silica: The active site for a catalytic reaction is a dynamic entity influenced by temperature, by the oxidizing and reducing nature of the gaseous atmosphere to which it is exposed, by the concentrations of both gas phase and adsorbed species and numerous other factors. We can conclude then that the "active site" for catalytic reaction is influenced by the conditions at which reaction occurs—indeed it might only exist at these conditions. It follows, then, that characterization of this active site may be most meaningful if it is done during chemical reaction.

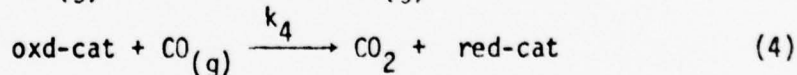
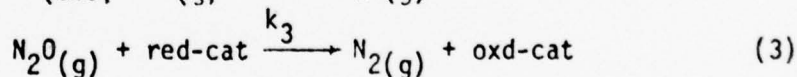
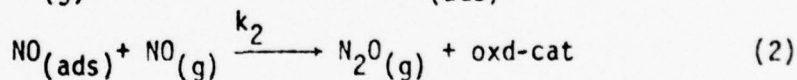
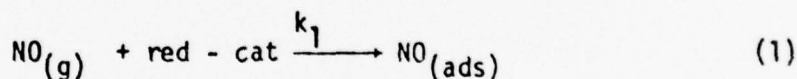
Of the many spectroscopic techniques used in surface chemistry, infrared spectroscopy has proven able to measure the surface concentration of adsorbed specie at reaction conditions. The successful application of infrared spectroscopy to identify surface species that are catalytically active depends on our ability first, to be able to "see" these species on the surface and second, to distinguish these species from the many other surface species that are not kinetically important.

Chromia catalysts are of both commercial and academic interest. Alumina-supported chromia is used to polymerize olefins<sup>(1)</sup>. Chromia also catalyzes the NO + CO reaction, of importance in automobile pollution control, in which it is selective to N<sub>2</sub>O formation<sup>(2)</sup>. The physical and chemical proper-

ties of chromia/alumina<sup>(3)</sup> and chemisorption and catalytic properties,<sup>(4)</sup> have been reviewed. The sensitivity of the state of the chromia catalyst to ambient conditions has been demonstrated by ESR<sup>(5,6)</sup> and magnetic susceptibility studies<sup>(7)</sup>.

The reaction of NO and CO on chromia has been critically reviewed by Shelef and Kummer<sup>(8)</sup> and more recently by Shelef<sup>(9)</sup>. The accepted mechanism for catalytic reduction of NO over a large number of catalysts is a redox (oxygen transfer) mechanism<sup>(9)</sup>. Studies by Taylor<sup>(10)</sup> first demonstrated the detrimental effect of excess oxygen on the NO reduction. Subsequent results by Shelef et al<sup>(2)</sup> indicate that when oxygen reacts with CO + NO mixtures, the oxidation of CO predominates. In addition, in situ determination of the oxidation state of the supported chromia catalysts showed that the presence of oxygen causes a more oxidized catalyst surface which is inactive for NO reduction by CO.

Niiyama et al<sup>(11,12)</sup> propose a rate expression based on applying the steady state assumption to the following series of redox steps:



If steady state is assumed, so that  $2r_1 = 2r_2 = 2r_3 = r_4$ , the following rate expression results:

$$r = \frac{2Nk_1k_2k_4P_{\text{NO}}P_{\text{CO}}}{2k_1k_2P_{\text{NO}} + (k_1 + k_2)k_4P_{\text{CO}}}$$

where N is total number of sites. If  $k_1k_2 \ll k_4$

$$\text{this reduces to } r = \frac{2Nk_1k_2P_{\text{NO}}}{k_1 + k_2}$$



They present data at 400°C to show the excellent fit of this proposed mechanism. This rate expression can not be correct at lower temperatures, however, since at steady state  $r_2 = r_3$  and no net formation of  $N_2O$  is predicted. The formation of  $N_2O$  as an intermediate in the  $CO + NO$  reaction over chromia (and other catalysts) has been reported by Shelef and Otto.<sup>(13)</sup> The appearance of  $N_2O$  at low temperatures which then peaks and disappears at higher temperature, coupled with the increase of  $N_2O/NO$  ratio with space velocity, led Shelef and Otto<sup>(13)</sup> to suggest that  $N_2O$  is a gas phase intermediate. As Shelef and Kummer<sup>(8)</sup> point out, however,  $N_2O$  formation is not inconsistent with the redox mechanism. Referring back to the sequence of reactions (1-4), reaction (2) must occur more rapidly than reaction (3).

Shelef and Kummer<sup>(8)</sup> also suggest that at lower temperatures the catalyst is covered with adsorbed  $NO$ , to the exclusion of adsorbed oxygen and  $N_2O$ . At higher temperatures, where the  $NO$  adsorption is reduced, adsorption of  $O_2$  and/or  $N_2O$  may be preferred. If this is the case, the increase and subsequent decrease of the  $N_2O$  concentration with increasing temperature may not indicate a single mechanism over the entire temperature range (in which  $N_2O$  is an intermediate). The decrease in  $N_2O$  at higher temperatures could be explained by the onset of new reactions, using up  $N_2O$ . This point is important since this assumption is one we plan to check in testing our proposed model.

## (2) Hydrocarbon Synthesis over bi-metallic clusters

Recent concern over oil supplies has, coupled with the USA's relative abundance of coal as compared to oil and natural gas makes it apparent that research is needed on processes using coal, rather than petroleum, as a hydrocarbon raw material. If coal is partially oxidized and combined with  $H_2$ , a "synthesis gas" mixture of  $CO$  and  $H_2$  may be used as feed stock for catalytic processes leading to a variety of processes ranging from methane to high molecular weight hydrocarbon waxes.

The success of such a process depends on the ability of the catalyst to selectively produce the specific desired product. Ruthenium's relatively unique ability to produce higher hydrocarbons makes it a most promising candidate for research in this area. The possibility of controlling and modifying the selectivity of multimetallic cluster catalyst of ruthenium to the metals will also be investigated. Sensitivity to sulfur poisoning is also an important practical criteria.

### C. Accomplishments

#### (1) CO + NO reactions on chromia supported on silica:

Results have been reported<sup>(14)</sup> at the Sixth International Congress on Catalysis, July 1976. Since the results are not yet in print, the important results that pertain to this proposal will be summarized in the following section.

##### (a) Introduction

The kinetics of the reduction of nitric oxide by carbon monoxide and the simultaneous measurement of the infrared spectra of the adsorbed species were studied in order to gain better understanding of the selectivity of chromia toward nitrous oxide formation. The information obtained from this approach was used in proposing a consistent reaction model, identifying the kinetically active surface species, and elucidating the active site character and poison effects.

##### (b) Experimental

The infrared spectra of the adsorbed species and the reaction kinetics were simultaneously measured at reaction conditions in a different plug flow recycle reactor in which the reacting gas (50 cc/min) was recycled (at 4000 cc/min) by a stainless steel bellows pump, assuring differential gradientless conditions in the reactor.



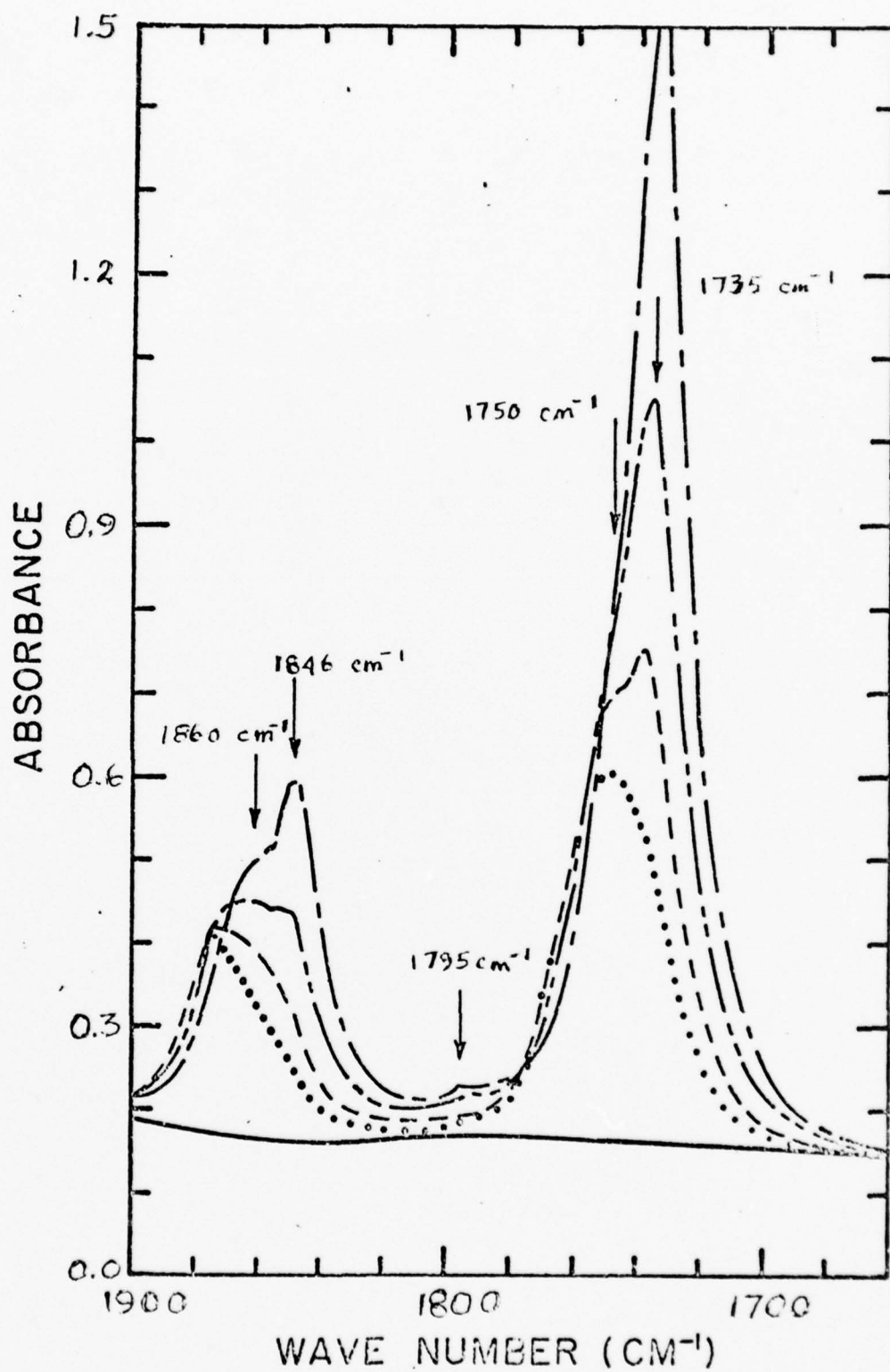


Figure 1. IR spectra taken during the NO/CO reaction over a chromia-silica catalyst.

### (c) Results

The experimental results are summarized in Figures 1, 2, and 3. The solid lines in Figures 2 and 3 curves are predicted by our proposed reaction model, which is discussed in the next section.

Figure 1 shows the spectra taken during reaction at 250°C. The fresh catalyst, calcined at 500°C, shows a high activity and gives rise to two strong IR bands at 1735  $\text{cm}^{-1}$  and 1846  $\text{cm}^{-1}$  under the reaction conditions. The activity decreased during the course of the experiments. At the beginning the deactivation was more rapid, becoming slower after several hours. During this deactivation, changes in IR spectra were noted.

A linear correlation between the band intensity of the 1735  $\text{cm}^{-1}$  band and the rate of  $\text{CO}_2$  formation has been found (see Figure 2). This correlation holds for a wide range of partial pressures of CO and NO. The 1735  $\text{cm}^{-1}$  band in Figure 1 includes a shoulder at 1750  $\text{cm}^{-1}$ , which becomes more prominent as the intensity of the 1735  $\text{cm}^{-1}$  band decreased. Similarly and more clearly, the fresh sample has a shoulder at 1860  $\text{cm}^{-1}$  associated with the 1846  $\text{cm}^{-1}$  band. As the sample deactivates, the 1846  $\text{cm}^{-1}$  band becomes the shoulder of the 1860  $\text{cm}^{-1}$  band as shown in Figure 1.

Integration of the band areas (from absorbance spectra) of these two bands, the 1735  $\text{cm}^{-1}$  and 1846  $\text{cm}^{-1}$  bands, yields a relatively constant ratio of 0.35 - 0.40.

In addition to  $\text{CO}_2$ , the NO/CO reaction produces nitrous oxide ( $\text{N}_2\text{O}$ ) and lesser amounts of nitrogen. In Figure 3 the selectivity of nitrous oxide (defined as  $r_{\text{N}_2\text{O}}/r_{\text{NO}}$ ) is plotted versus the partial pressure of nitric oxide at fixed values of CO partial pressure and chemisorbed NO concentration ( $\log(I_0/I)$ ). The selectivity of nitrous oxide is dependent on the partial pressure

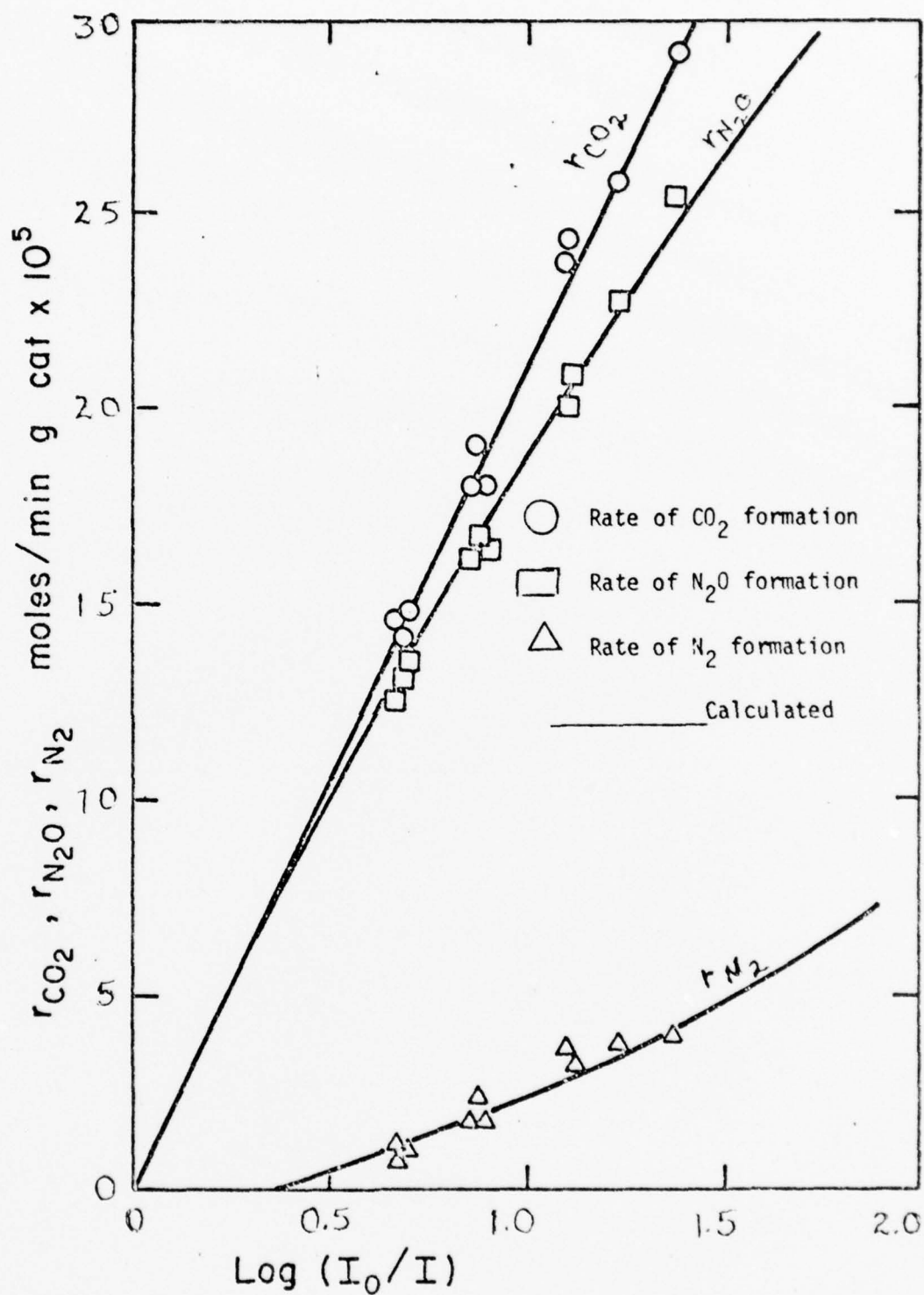


Figure 2. Rates of  $\text{CO}_2$ ,  $\text{N}_2\text{O}$ , and  $\text{N}_2$  formation versus  $\log(I_0/I)$ .

$P_{\text{CO}} = 245$  torr,  $P_{\text{NO}} = 90$  torr,  $250^\circ\text{C}$ .

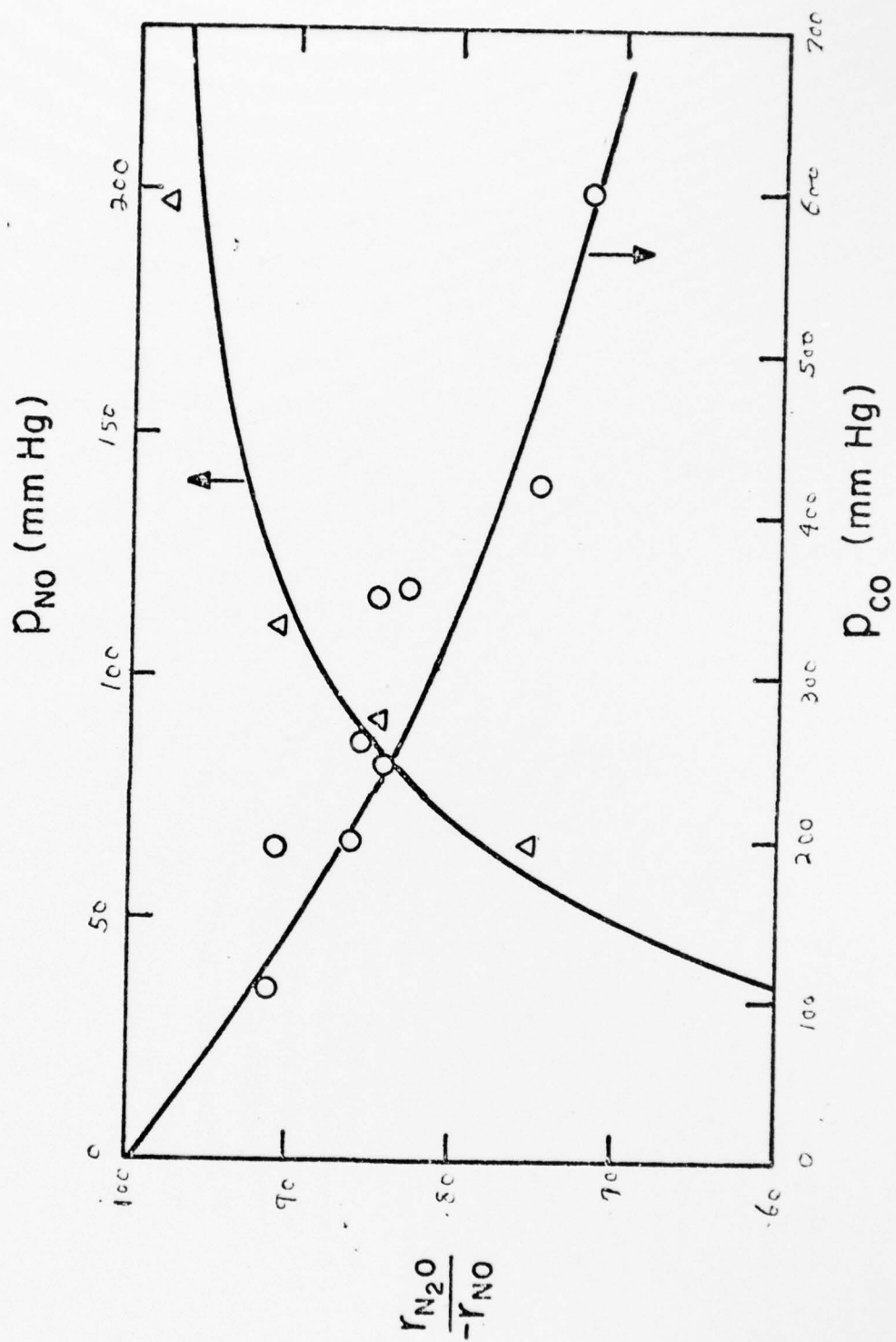
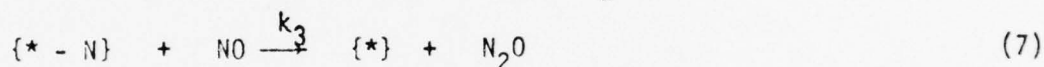


Figure 3 Selectivity as a function of  $P_{CO}$  and  $P_{NO}$

of CO as well as NO, and surface concentration of chemisorbed nitric oxide as indicated by the intensity of the band at  $1735\text{ cm}^{-1}$ . In general, the selectivity decreases as either partial pressure of CO or the surface concentration of chemisorbed NO increases. However, a higher partial pressure of NO leads to a higher selectivity of nitrous oxide if other variables are fixed.

A reaction model which is consistent with infrared and kinetics analyses can be represented by the following four steps:



where  $\{*\}$  is active site;  $\{* - \text{NO}\}$  and  $\{* - \text{N}\}$  are chemisorbed NO and N on the surface, respectively. The concentration of chemisorbed NO,  $[\text{*}-\text{NO}]$ , the rate determining active center, is proportional to the band intensity at  $1735\text{ cm}^{-1}$ :

$$[\text{*} - \text{NO}] = C \log (I_0/I) \quad (9)$$

where C is the proportionality constant. Assuming the rate of formation of  $\{* - \text{N}\}$  in step (6) is equal to the rate of consumption of  $\{* - \text{N}\}$  in step (7) and step (8); i.e.

$$k_2 [\text{*} - \text{NO}] P_{\text{CO}} = k_3 P_{\text{NO}} [\text{*} - \text{N}] + k_4 [\text{*} - \text{N}]^2 \quad (10)$$

where  $P_i$  is the partial pressure of the  $i^{\text{th}}$  component,

the surface concentration of  $\{* - \text{N}\}$  can be calculated by Equation (11):

$$[* - N] = \frac{-k_3 P_{NO} + \sqrt{k_3^2 P_{NO}^2 + 4k_2 k_4 [* - NO] P_{CO}}}{2k_4} \quad (11)$$

The rate of  $CO_2$ ,  $N_2O$  and  $N_2$  formation can be written as:

$$r_{CO_2} = k_2' P_{CO} \log(I_0/I) \quad (12)$$

$$r_{N_2O} = \frac{k_3^2 P_{NO}^2}{2k_4} \left( -1 + \sqrt{1 + \frac{4k_2' k_4 P_{CO} \log(I_0/I)}{k_3^2 P_{NO}^2}} \right) \quad (13)$$

$$r_{N_2} = \frac{k_3^2 P_{NO}^2}{4k_4} \left( -1 + \sqrt{1 + \frac{4k_2' k_4 P_{CO} \log(I_0/I)}{k_3^2 P_{NO}^2}} \right)^2 \quad (14)$$

where  $k_2'$  is the product of  $k_2$  and  $C$ . From Equation (12) and either Equation (13) or Equation (14),  $k_2'$  and  $k_3^2/k_4$  can be calculated. Values of  $k_2'$  and  $k_3^2/k_4$  at  $250^\circ C$  are shown below:

$k_2'$		$k_3^2/k_4$	
$1.27 \times 10^{-5}$	$\pm 3\%$	$1.91 \times 10^{-6}$	$\pm 7.8\%$

Based on these values of  $k_2'$  and  $k_3^2/k_4$ , kinetic data were simulated and plotted with the observed data as shown in Figures 2 and 3. Good agreement was obtained.

Other, more complex reaction sequences were considered which led to models with additional parameters. The added complexity did not seem justified, based on the excellent fit of the two parameter model to the data shown in Figures 2 and 3.



If, as indicated by the infrared evidence, the predominate adsorbed NO specie is a dinitrosyl complex, then both the IR and kinetic data can be explained if the surface specie represented by  $\{*\}$  in equations (5)-(8) is  $\text{Cr} \begin{array}{c} \diagup \\ \diagdown \end{array} \text{NO}$ .

(2) Hydrocarbon synthesis over bi-metallic clusters:

Quantitative analysis of CO methanation mixtures using a quadrupole mass spectrometer can be achieved by following careful calibration procedures described above. Care must be taken to operate the instrument in a pressure region where the signal responds linearly to increases in partial pressure. With proper calibration, mass spectral analysis can be coupled with a differential reactor to measure both steady state and transient reaction rates at low conversion. The transient response of methanation rate over .5% RU/Al<sub>2</sub>O<sub>3</sub> in the Union Carbide gradientless reactor to a step function of CO into a H<sub>2</sub> stream flowing over the catalyst showed a maximum in the rate, six to eight times as large as the steady state value, as shown in Fig. 4. The rate maximum can be explained as an adjustment of the surface concentration of CO from zero to the steady state value with the concentration passing through some optimum value, with respect to adsorbed hydrogen, for methanation activity. The possibility of the maximum in rate being enhanced by thermal effects is also suggested.

Evidence for the possibility of thermal effects was given in the performance of a glass U-tube reactor filled with the same catalyst and treated in a similar manner but heated in a tube furnace. Upon introduction of the step function of CO to the H<sub>2</sub> reactant stream, this reactor was unable to transfer the excessive heat of reaction away from the catalyst fast enough and the system proceeded to a new steady state at higher temperature and

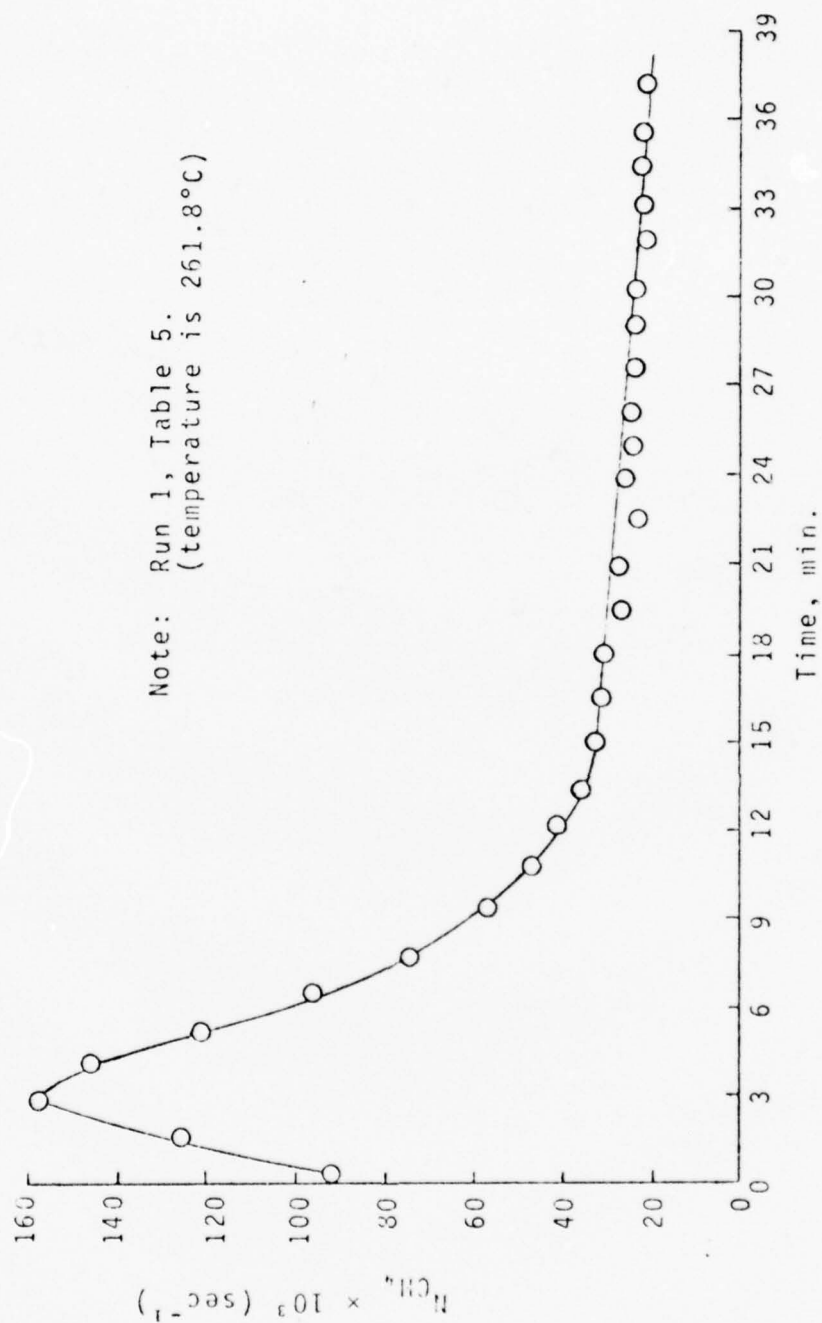


Figure 4. Turnover Number Versus Time for .5% Ru/Al<sub>2</sub>O<sub>3</sub>.

nearly 100% conversion. When care was taken to minimize the heat transfer problem by replacing the tube furnace with a fluidized bed sandbath, steady state differential kinetic data were easily obtained. The analysis included quantitative reaction rate measurement of methane and ethane with qualitative observation of higher hydrocarbon products.

#### D. Results in the Last Three Months

##### (1) CO and NO reactions on chromia supported on silica:

In the past three months extensive modifications to the IR reactor system were in progress. Modifications are being made that will enable us to:

- a) pretreat the samples under high vacuum conditions
- b) interchange cells so that more efficient use of the apparatus is possible
- c) control the temperature more closely
- d) perform isotope experiments in a minimum volume system.

##### (2) Hydrocarbon synthesis over bimetallic clusters:

Steady state kinetic analysis of 10% Ru/SiO<sub>2</sub>, 10% Ru-1% Fe/SiO<sub>2</sub>, 3% Ru-1% Fe/SiO<sub>2</sub> and 1% Fe/SiO<sub>2</sub> was done in the Union Carbide gradientless reactor after allowing the transient behavior to diminish. The 1% Fe/SiO<sub>2</sub> sample showed no activity for hydrocarbon synthesis. The 10% Ru/SiO<sub>2</sub> showed methanation activity but little activity for synthesis of higher molecular weight hydrocarbons while the bimetallic samples showed extensive higher hydrocarbon formation. Because the activity of the bimetallic samples cannot be explained as the sum of the activities of the monometallic catalysts at the same loadings, intimate contact of the active metals in the bimetallic samples is suggested. This suggestion has been confirmed by Mössbauer spectroscopic studies done on the same samples. The Mössbauer data show clearly that a new Fe<sup>0</sup> state, no bulk, metallic Fe, is formed

in the presence of Ru and that the oxidation reduction behavior of this new state can be understood only if intimate contact between reduced Fe and Ru is assumed. Dispersions of the supported Ru-Fe catalysts have been found by both  $H_2$  chemisorption and x-ray diffraction line broadening to be of the order 10% for 10% Ru-1% Fe/SiO<sub>2</sub> and 30% for 3% Ru-1% Fe/SiO<sub>2</sub>.

A new reactor system is now in use to analyze product distributions in more detail via gas chromatographic analysis of the products. Mole fractions of C<sub>1</sub>-C<sub>3</sub> species in the products are shown below for 3% Ru-1% Fe/SiO<sub>2</sub> run at 265°C and an H<sub>2</sub>/CO ratio of 3. The total conversion was 1% and the turnover number was c.a.  $3 \times 10^{-3}$  molecules CO reacted per metal surface atoms per second.

Product molecule	CH <sub>4</sub>	C <sub>2</sub> H <sub>6</sub>	C <sub>2</sub> H <sub>4</sub>	C <sub>3</sub> H <sub>8</sub>	C <sub>3</sub> H <sub>6</sub>
Mole fraction	0.63	0.11	0.07	0.04	0.15

These results are of particular interest because they show that nearly 30% of all the CO converted ends up as propylene. Further enhancement of this relatively high yield for a higher molecular weight olefin as well as continued development of several leads produced in this work will be the object of ongoing research in this area.

E. References

1. A. Clark, Catal. Rev., 3, 145 (1969).
2. M. Shelef, K. Otto, and H. Gandhi, J. Catal., 12, 361 (1968).
3. C. P. Poole and D. S. MacIver, Advan. Catal., 17, 223 (1966).
4. R. L. Burwell, Jr., G. L. Haler, K. C. Kaylor and J. F. Read, Advan. Catal. 20, 1 (1969).
5. L. L. Van Reijen, W. M. H. Sachtler, P. Cossee, and D. M. Brouwer, Proc. Int. Congr. Catal., 3rd, 1964, 2, 829 (1965).
6. D. E. O'Reilly and D. S. MacIver, J. Phys. Chem. 66, 276 (1962).
7. V. B. Kazanski and J. Turkevich, J. Catal., 8, 231 (1967).
8. M. Shelef and J. T. Kummer, Chem. Eng. Progr. Symp. Ser., 67, 74 (1971).
9. M. Shelef, Cat. Rev., 11, 1 (1975).
10. F. R. Taylor, Air Pollution Foundation Report No. 28, (1959).
11. H. Niiyama, H. Iida, and E. Echigoya, Nippon Kagaku Kaishi, 9, 1467 (1975).
12. E. Echigoya, H. Niiyama, A. Ebitani, and K. Murata, Japan-USA Seminar on Catalytic NO Reactions, Susono, Japan, November 1975.
13. M. Shelef and K. Otto, J. Catal., 10, 408 (1968).
14. S. S. Shih, R. G. Squires, and D. S. Shihabi, Proceedings of the Sixth Int. Cong. on Catal., London, July 12-16, 1976.
15. K. A. Windhorst and J. H. Lunsford, J. Amer. Chem. Soc., 97, 1407 (1975).



## Characterization of Surface States by ESCA

R. A. Walton  
Department of Chemistry

N. Winograd  
Department of Chemistry

1. Objective

Our proposed research encompasses the continuing development of electron spectroscopy (ESCA) as a technique to determine surface chemical structure as it relates to heterogeneous catalytic and electrochemical reaction mechanisms. We are particularly concerned with the behavior of clean metal surfaces, prepared under ultra-high vacuum ( $\sim 10^{-10}$  torr) conditions, after exposure to active gases ( $O_2$ , CO, NO, etc.). The major purpose of these experiments will be to characterize the oxidation state of all the stable surface species with a special emphasis on those possessing unusual oxidation states. With a backlog of information of this type we plan to compare these results to samples actually exposed to reaction conditions, be they catalysts or electrodes used in electrocatalytic processes. We feel very strongly that one of the primary advantages of the ESCA technique is that useable data can be obtained not only on "clean" systems prepared at  $10^{-10}$  torr but also on "dirty" systems prepared under reaction conditions, such as the chromia/silica catalyst system. The possibility of "bridging the gap" between these two situations is most exciting to researchers in the catalysis field. Since these complex surfaces must determine the course of most heterogeneous reactions, the ability to characterize these species will have a tremendous impact in identifying the active molecules in many catalytic processes. In addition, the efficiency and reliability of battery power systems and fuel cells depend greatly on the materials character of the electrodes. The dynamic stability of these materials will clearly be related to the types of any unusual species which may form on the electrode surfaces.



## 2. Background and Technical Need

The proposed plan of research encompasses the development of the ESCA technique to determine heterogeneous catalytic and electrochemical reaction mechanisms. The first phase of the work has been concerned with the interaction of clean metal surfaces with gases and metals using samples prepared under ultra high vacuum ( $\sim 10^{-10}$  torr) conditions. The major purpose of these experiments has been to characterize all the stable surface species with particular emphasis on those possessing unusual oxidation states. These studies will now be applied to the characterization of samples more directly related to the actual environment of the catalyst or the electrode. This second phase includes the correlation of the steady state surface behavior as observed by ESCA with any catalytic activity. In addition, we plan to study reactions of unusual importance to fuel cell technology and to fundamental corrosion mechanisms. Emphasis will be placed on systems which affect the electrode surface, such as oxidation and adsorption processes, so that the chemical structure of products can be determined.

Paralleling these studies will be an attempt to correlate the changes in metal core binding energies with change in oxidation state for derivatives of certain key metals which show catalytic activity. Included in our studies will be derivatives of rhodium, rhenium, ruthenium and molybdenum, all of which find use as important components for certain heterogeneous catalysts. In these instances, these species will not be generated in situ but rather will be synthesized outside of the spectrometer and then subjected to ESCA studies. The object here is to generate species of known stoichiometry and molecular structure in order to make a detailed correlation of metal core electron binding energies with structure. This will be of help in our identification of species which are subsequently generated in situ during catalysis.

All ESCA measurements will be made on an existing Hewlett-Packard 5950A Spectrometer. This instrument utilizes monochromatic  $Al K_{\alpha}$  X-ray obtained from a quartz crystal disperser as well as a multi-element detection scheme. The enhanced resolution and sensitivity of this configuration is vital

for interpretation of complex spectra which have overlapping bands. For example, the Au  $4f_{7/2}$  peak on this instrument has a F.W.H.M. of about 0.8 eV. Without the crystal disperser, as is the case with all other commercial instruments, this value rises to  $\sim 1.2$  eV. Since chemical shifts on the order of 0.5 eV need to be discerned on peaks which are overlapping, the use of the Hewlett-Packard system is absolutely essential to perform these experiments.

The x-ray generator and electron analyzer are isolated from a sample treatment chamber by a high vacuum gate valve. This chamber is then pumped separately with two 30 l/sec noble ion pumps and a 350 l/sec titanium sublimator pump. The sample itself is placed on a probe which can be pushed through a set of sliding teflon seals into this chamber and into the analyzer for special analysis. The sample chamber is equipped with a cross-probe for in situ evaporation, a leak valve for introducing needed gases as well as an argon ion gun. The temperature of the sample can be set from  $-180^{\circ}\text{C}$  to  $350^{\circ}\text{C}$ , as indicated by a platinum resistance thermometer, by heating a filament implanted underneath the sample or by passing cooled  $\text{N}_2$  gas through the sample probe tip<sup>1</sup>.

We have added several important additions to this system to expand its versatility for surface studies. First, although the system is essentially compatible for ultra high vacuum, the sliding seal arrangement for the sample probe is not satisfactory. An external chamber was built around the sample inlet with a controlled atmosphere of pure argon. This procedure allows direct transfer of samples from this "dry box" into the instrument without exposure to air or water. To attain pressures of  $10^{-10}$  torr, a bake out oven was built around the instrument and it could be heated to  $150^{\circ}\text{C}$  for removal of residual water. A residual gas analyzer has been installed and is able to monitor the residual gas level<sup>2</sup>.

Three types of sample treatments are available using the above scheme:

(1) "Clean" surfaces can be exposed to low levels of background gases (to  $5 \times 10^{-6}$  torr) during x-ray analysis. This procedure is particularly useful for observing the initial stages of surface coverage<sup>3,4</sup>.

(2) Samples can be extensively exposed to higher pressures in the treatment chamber (up to atmospheric pressure) but the gas must be removed during spectral analysis.

(3) Gross perturbations, such as electrochemical or catalytic reactions can be carried out in the external dry box sample chamber although the spectra must be recorded in vacuo<sup>5</sup>

### 3. Accomplishments

The major thrust of this research has been to identify the presence of various oxidation states on metal and metal oxide surfaces. We have focussed primarily on ESCA and Auger spectroscopy (AES) as tools to carry out this aim. The specific developments during the last year are now presented in greater detail:

(1) X-ray Photoelectron Spectroscopic Studies of PbO Surfaces Bombarded with  $\text{He}^+$ ,  $\text{Ne}^+$ ,  $\text{Ar}^+$ ,  $\text{Xe}^+$ , and  $\text{Kr}^+$ .

Many surface analysis techniques, which involve the characterization of surfaces and the determination of in-depth concentration profiles, are carried out by combining various spectroscopic methods with gas ion-bombardment. For example, ion scattering spectrometry (ISS) is a technique based on the measurement of the energy of primary ions elastically scattered from a solid surface. Secondary ion and ionized neutral mass spectrometric methods (SIMS and INMS) are based on studying the mass distribution of sputtered particles generated by primary ion bombardment. In other relatively non-destructive methods such as ESCA and AES, ion bombardment is employed simply to remove outer layers for in-depth profiling or to uncover a fresh surface.

Modification of surface composition by the incident ion is a factor which must be understood if these techniques are to be of quantitative utility in characterizing surfaces. For example, in ISS measurements which are most surface sensitive (its sampling depth is limited to the outermost atomic layer or two), chemical modification resulting from primary ion-solid interactions may provide erroneous information regarding the initial surface composition. The study of ion surface interactions in binary targets is also of interest in developing relevant theories of the sputtering process for these complex systems.

The surface composition of PbO has been studied with ESCA after bombardment with several inert gas ions of 400 eV. The results show reduction of PbO to metallic Pb with the degree of damage following the order  $\text{He}^+ > \text{Ne}^+ > \text{Ar}^+$ . Both  $\text{Kr}^+$  and  $\text{Xe}^+$  did not reduce the oxide. The depth of damage varied from  $\sim 9 \text{ \AA}$  for  $\text{He}^+$  to  $\sim 1 \text{ \AA}$  for  $\text{Ar}^+$  bombardment. The results were compared to a collisional and a thermal model of the sputtering process.<sup>6</sup>

## (2) The Surface Chemistry of the Cd- and Ag-Oxygen Systems.

The surface chemistry of the Cd- and Ag-oxygen systems has been studied by ESCA using both temperature changes and ion bombardment techniques as methods of inducing structural changes.<sup>7</sup> For the Cd system, the O 1s binding energies for CdO,  $\text{Cd}(\text{OH})_2$ ,  $\text{CdCO}_3$ , and  $\text{CdO}_2$  have been characterized and have been used to follow the decomposition of these species as a function of temperature. For oxygen-exposed evaporated films of Cd, two distinct oxygen phases were noted with one being specifically identified as CdO. For the Ag system, the O 1s binding energies of AgO,  $\text{Ag}_2\text{O}$ , and  $\text{Ag}_2\text{CO}_3$  were reported. On the oxides prepared in air, a significant carbonate contaminant was noted which complicated the interpretation of the O 1s spectra. For oxygen-exposed



evaporated Ag films, no oxide phases were noted even at high oxygen exposures although a broad, structureless background, probably corresponding to absorbed oxygen, was observed.

(3) Auger studies of metal surfaces and their implication to electronic structure elucidation.

A theory has been developed for predicting Auger energies with the use of ESCA binding energies which is rigorous within the framework of the theory of extra-atomic relaxation developed by Shirley et al. Calculations are given for the  $L_3 M_{23} M_{23}$  Auger energies of metallic Ni, Cu and Zn. We argue that the atomistic approach to calculating Auger energies should be valid for Ni as it is for non-transition metals. By including the effect of the second screening orbital on the Auger energy and by taking into account the change in initial state electronic configuration between gas phase Ni atoms and metallic Ni, agreement with experiment can be nearly as good as for the Cu and Zn cases. The results strongly suggest that the first screening orbital is 3d-4s admixed while the second screening orbital is almost 4s-like.

(4) ESCA Studies of Platinum electrode surfaces.

The surface oxides produced from potentiostatic and galvanostatic oxidation of Pt electrodes in  $HClO_4$  and  $H_2SO_4$  are examined using x-ray photoelectron spectroscopy.<sup>8</sup> The oxide I species produced as the initial oxidation product by successively more anodic potentiostatic oxidation in 0.2  $HClO_4$  is found to have a  $Pt^{2+}$  oxidation state, a binding energy characteristic of neither  $PtO$ ,  $Pt(OH)_2$  or  $PtO_2$ , and a limiting thickness of 8 Å. Galvanostatic oxidation in  $HClO_4$  and  $H_2SO_4$  is found to produce  $PtO_2 \cdot H_2O$  as an unlimiting growth oxide or a limiting growth oxide layer depending on the concentration of the acid electrolyte. The incorporation of

the acid electrolyte anion in the surface layer is shown to have an effect on which type of oxide layer is produced. X-ray decomposition and chemical modification by  $\text{Ar}^+$  stripping are shown to produce chemical artifacts complicating any interpretation of a Pt oxide surface layer.

The underpotential deposition (UPD) of copper and silver ions on platinum electrodes has been studied using x-ray photoelectron spectroscopy (ESCA). A significant chemical shift of the ESCA binding energies of the UPD copper and silver atoms relative to bulk copper and silver metal is obtained. Analogous spectral results are obtained for in situ vapor deposition of copper and silver atoms on clean platinum substrates which reveal the metallic nature of the UPD species.

#### (5) ESCA Studies of Chromia Catalysts.

ESCA studies on chromia/silica (Cab-O-Sil) catalysts have now been completed.<sup>9</sup> Supported chromium oxide catalysts have a wide variety of applications including ethylene polymerization,<sup>10</sup> and oxidation-reduction reactions between environmentally important molecules such as CO and NO.<sup>11</sup> In recent years many efforts have involved the characterization of these catalysts in an attempt to sort out the appropriate reaction mechanisms. Volumetric titrations to determine the bulk oxidation state of the chromium routinely used in conjunction with infrared and electron paramagnetic resonance spectroscopy have eluded much information dealing with the above questions. However, these techniques have also revealed that the chromia system is highly complex and as a result, many ambiguities have arisen concerning the state of the catalyst throughout its various reaction histories. One controversial aspect concerns the oxidation state of the chromia which is present as a result of reaction with CO and NO. In relation to treatment of the catalyst with these two gases both singularly and



as a mixture, a wide range of chromium oxidation states from II to V have been proposed. As a possible tool to gather additional information concerning this aspect, we have used XPS to investigate the surface during various stages and conditions of reaction of the chromia catalyst with carbon monoxide and nitric oxide.

The discussion of the results can be divided conveniently into two parts: evidence for (1) changes in oxidation state and dispersion which occur as a result of different calcination temperatures and (2) changes on the surface of the catalyst after reaction with CO and NO.

An analysis of the changes which occur in the Cr 2p spectra of the catalysts as the calcination temperature is varied shows that for the non-calcinated samples, the chromium species are predominantly in the Cr(VI) oxidation state. When these samples are heated to higher temperatures there is a shift of the Cr 2p peaks to lower energies with the Cr(III) state predominating at temperatures of 500°C and above. We note that while the samples calcinated at high temperature have Cr 2p energies which differ from the related energy of bulk  $\text{Cr}_2\text{O}_3$  by only ~0.5eV, the noncalcinated sample is considerably different from  $\text{CrO}_3$ . In fact the experimental values correlate quite well with the Cr 2p<sub>3/2</sub> energies of chromate and dichromate. This observation tends to support the proposed<sup>12,13</sup> chromate and/or dichromate structure of chromia on silica, although unfortunately it is not possible to distinguish between the two by XPS.

In addition to the binding energy shifts which establish the presence of Cr(VI) and/or Cr(III) species, a very dramatic increase in the intensity of the Cr 2p peaks occurs for the sample calcinated at 500°C. Further characteristics of this particular sample include the appearance of an additional O 1s peak at 530.7eV (believed to be the result of crystalline

$\text{Cr}_2\text{O}_3$ ) and an equally dramatic decrease in the intensity of the Si 2p peak. We found this change to be evident on samples containing between 5 and 15% chromium. Through efforts to reproduce this effect we found that both the calcination temperature and the procedure we used to prepare the catalyst were critical. Apparently this intensity change occurs only over a narrow temperature range of approximately  $20^\circ\text{C}$  and by about  $550^\circ\text{C}$  this intensity enhancement had largely disappeared. Furthermore, it was found that when samples which had been calcinated at  $500^\circ\text{C}$  were reheated in air at a lower temperature (4 hours at  $300^\circ\text{C}$ ) this dispersion change was reversed.

Since peak intensities in XPS are directly related to surface concentration, the observed Cr 2p intensities can be at least qualitatively related to the concentration of chromium on the surface. As the larger platelets of  $\text{Cr}_2\text{O}_3$  form at approximately  $500^\circ\text{C}$  and grow to cover the surface, we would expect that the surface concentration of chromium would be greater than that of the initially prepared sample. In addition, this change should be accompanied by a decrease in the relative intensity of the Si 2p peak since the environmental effect of the silica should be correspondingly reduced. This is in fact observed. Furthermore, the formation of a very high surface concentration of  $\text{Cr}_2\text{O}_3$  should result in the appearance of an associated O 1s binding energy. This peak should be located at  $\sim 530.8\text{eV}$  since Allen *et al.*<sup>14</sup> have established that for  $\text{Cr}_2\text{O}_3$  the binding energy difference  $\Delta E(\text{Cr } 2p_{3/2} - \text{O } 1s)$  is  $46.3\text{eV}$ . The O 1s peak that we observe at  $530.7\text{eV}$  is clearly this particular binding energy, its intensity behavior closely mirroring that observed for the Cr  $2p_{3/2}$  peak at  $577.1\text{eV}$ . The decrease in intensity of both the Cr 2p ( $577.1\text{eV}$ ) and O 1s ( $530.7\text{eV}$ ) binding energies as the calcination temperature is raised above  $500^\circ\text{C}$  can be explained

by a decrease in crystallinity which results in a lower surface concentration of chromium.

Measurements were made of the Cr 2p and O 1s binding energies of the catalysts after they had been reacted separately with CO and NO and with 1:1 mixtures of these two gases. The spectra were monitored after reaction at 300°C for a period of three hours. The experimental conditions under which the binding energies were measured (a pressure of  $\sim 10^{-8}$  torr) do not of course correspond to the conditions which prevailed during measurements of the infrared spectra of NO and CO adsorbed on silica supported chromia<sup>15-18</sup>. Accordingly, although we are unable to monitor the nature of the reversibly absorbed species, this technique is suited to an investigation of the nature of the chromium species which are present.

When catalyst samples which had been calcinated at 500°C were reacted with CO, a shoulder appears at  $\sim 576.4$  eV on the low binding energy side of the Cr 2p<sub>3/2</sub> peak due to Cr(III). By measuring the separation between the related Cr 2p peaks of Cr(VI) and Cr(III) species it is apparent that the average binding energy shift per unit change in oxidation number is  $\sim 0.8$  eV. If this linear relationship persists in going from Cr(III) to Cr(II) oxide then the observed Cr 2p<sub>3/2</sub> energy of 576.4 eV is consistent with the presence of Cr(II). Qualitatively relating the intensity of this shoulder to the concentration of Cr(II) present, indicates that while considerable amounts are generated in samples which had been calcinated at temperatures of 500°C and above, samples that were not calcinated or calcinated at 300°C showed very little chromium reduction.

Although the lower oxidation state is also produced when NO is passed over the catalyst at 300°C, the degree of reduction is much less than in the

#### 4. Accomplishments (6/30/76-9/30/76).

Recent work updates the progress reported in the previous section.

Both x-ray photoelectron spectroscopy (ESCA) and Auger electron spectroscopy (AES) have been extensively employed for the quantitative determination of surface compositions of alloys. In both techniques it was common practice to assume that signal intensity is linearly proportional to concentration, although possible matrix-related deviations from linearity are sometimes included.

Elemental Auger and intensity ratio measurements for Pd and Ag with varying alloy compositions were studied. PdAg alloy surface compositions calculated from Auger and from core-level spectral information differ. The Pd Auger/3d intensity ratio was severely affected by the alloy composition while the Ag Auger/3d intensity ratio was nearly unchanged. We attribute these deviations to the localized nature of the Pd 4d electrons when diluted in Ag compared to their relative band-like nature in bulk Pd, thus altering the Auger transition probabilities. We believe comparison of AES and ESCA intensity measurements in this manner provides valuable insight into the electronic structure of these alloys and exposes the large errors that may result in quantitative surface analysis using valence level coupled Auger transitions.

The underpotential deposition of monolayer quantities of Ag and Cu has been studied using ESCA and Auger spectroscopy. ESCA chemical shifts of -0.65 and -0.95 eV vs. the bulk metal were observed although no distinction was noted between the various underpotential states present in the cyclic voltammogram. The shifts were identical to vapor deposited submonolayer films of Ag and Cu on Pt in the low coverage ( $\theta \sim 0.1$ ) limit. A gradual shift with coverage to the bulk metal value for the vapor deposited films and a constant shift with coverage for the underpotential deposit indicated that islanding was present

only in the evaporated films. Measurement of the Cu and Ag Auger spectra gave results independent of the surface work function when compared to the ESCA spectra. Interpretation of this Auger parameter is, however, at present ambiguous.



## REFERENCES

1. K. S. Kim and N. Winograd, Surface Sci., **43**, 625 (1974).
2. K. S. Kim, W. E. Baitinger, J. W. Amy and N. Winograd, J. Electron Spectros., **5**, 351 (1974).
3. (a) J. T. Yates, Jr., and N. E. Erickson, Surface Sci., **44**, 489 (1974).  
(b) D. A. Shirley, Chem. Phys. Lett., **16**, 220 (1972).  
(c) P. H. Citrin and T. D. Thomas, J. Chem. Phys., **57**, 4446 (1972).
4. (a) K. S. Kim and N. Winograd, Chem. Phys. Lett., **19**, 209 (1973).  
(b) K. S. Kim, T. J. O'Leary and N. Winograd, Anal. Chem., **45**, 2214 (1973).
5. K. S. Kim and N. Winograd, J. Catal., **35**, 66 (1974).
6. G. C. Allen, M. T. Curtis, A. J. Hooper and P. M. Tucker, J. Chem. Soc., Dalton, 1675 (1973).
7. A. Zecchina, E. Garrone, G. Ghiotti and S. Coluccia, J. Phys. Chem., **79**, 972 (1975).
8. A. Zecchina, E. Garrone, C. Morterra and S. Collucia, J. Phys. Chem., **79**, 978 (1975).
9. S. A. Best, R. G. Squires and R. A. Walton, J. Catalysis, submitted for publication.
10. J. P. Hogan, J. Polymer Sci., A-1, **8**, 2637 (1970).
11. M. Shelef, K. Otto and H. Gandhi, J. Catalysis, **12**, 361 (1968).
12. A. Zecchina, E. Garrone, G. Chiotti, C. Morterra and E. Borello, J. Phys. Chem., **79**, 966 (1975).
13. F. J. Karol, G. L. Karapinka, C. Wu, A. W. Down, R. N. Johnson and W. L. Carrick, J. Polymer Sci., A-1, **10**, 2621 (1972).
14. G. C. Allen, M. T. Curtis, A. J. Hooper and P. M. Tucker, J. Chem. Soc., Dalton, 1675 (1973).
15. A. Zecchina, E. Garrone, G. Chiotti and S. Coluccia, J. Phys. Chem., **79**, 978 (1975).
16. A. Zecchina, E. Garrone, C. Morterra and S. Collucia, J. Phys. Chem., **79**, 978 (1975).
17. E. L. Kugler, R. J. Kokes and J. W. Gryder, J. Catalysis, **36**, 142 (1975).
18. E. L. Kugler and J. W. Gryder, J. Catalysis, **36**, 152 (1975).
19. M. Shelef, K. Otto and H. Gandhi, J. Catalysis, **12**, 361 (1968).

## Electrode Reaction Studies

### Role of Surface Oxides on Cathode Surfaces

L. F. Albright, School of Chemical Engineering

#### Summary of Results

Considerable new information has been obtained that clarifies and begins to quantify the factors that control the current fluxes in hydrogen-oxygen fuel cells. Extensive information has been obtained for both the cathode and, to a lesser extent, the anode when both solutions of sulfuric acid and of potassium hydroxide were employed as electrolytes. These results can in part be interpreted by means of the relative amounts of platinum oxides present on the platinum electrodes used. The conditions required for obtaining maximum current fluxes vary for the following comparisons:

- (a) Cathode versus anode.
- (b) Submerged portion of electrode versus portion at or near the triple interface (between gas, electrolyte, and electrode).
- (c) Different polarizations (defined as potential difference between electrodes).

#### Experimental Approach

In the fuel cell being used, flat-plate platinum electrodes (cathode or anode) are being used (1,4,6). These electrodes can be partially or completely immersed in the electrolyte. By changing the height of the electrode relative to the electrolyte, the submerged area can be varied; using this technique, any of the following can be investigated: meniscus current, current in the submerged portion of the electrode, or a combination of the above two. By use of a shield positioned around an electrode, transfer of reactant (either oxygen or hydrogen) to the electrode can be made to occur in only a one-directional

manner. (Such one-dimensional transfer is much easier to model mathematically.) In the cell used, current densities in the portion of the electrode near the meniscus (close to where there is a triple interface of electrolyte solution, reactant gas (oxygen or hydrogen), and platinum electrodes) are much greater than in the portions of the electrode that are submerged. A reference electrode is used so the polarization of the electrode being investigated can be measured (and changed if desired by suitable equipment) as the cell is used.

The surfaces of several small test cathodes have also been analyzed for surface oxides using x-ray photoelectron spectroscopy (ESCA or XPS). These test cathodes have been analyzed after specific treatments or use (in the fuel cell).

The range of operating conditions investigated has been as follows:

Temperatures	15 to 80°C
Electrolytes	0.25 to 2.0 N sulfuric acid 0.25 to 4.0 N potassium hydroxide
Polarization	0.1 to 0.8 volts

### Results

ESCA analysis of test cathodes (that measured O 1s/Pt 4f peak area ratios) indicated that the amounts of platinum oxides on the surface changed significantly during the first several seconds after the start-up of the cell. There was a large decrease in the oxygen-to-platinum ratios during the first several seconds of operation of a cathode in the fuel cell (i.e. several seconds after the circuit was closed). The cathodes used were first activated using boiling nitric acid and were then rested (at open circuit) in the potassium hydroxide solutions used as electrolyte. Table 1 shows the results. After the activation and during the rest periods, substantial amounts of platinum oxide were on the

Table 1

Electrode	Treatment	o 1s/Pt 4f Peak Area Ratio
1	Heated in $\text{HNO}_3$ for 2 hrs.	0.18
2	Heated in $\text{HNO}$ for 2 hrs; Soaked in $\text{O}_2$ -sat. 1 N KOH for 20 min.	0.16
1	Heated in $\text{HNO}$ for 2 hrs; Soaked in $\text{O}_2$ -sat. 1 N KOH for 20 min; Cathode in fuel cell $n=0.5$ for 1 sec.	0.074
3	Heated in $\text{HNO}$ for 2 hrs; Soaked in $\text{O}_2$ -sat. 1 N KOH for 20 min; Cathode in fuel cell $n=0.5$ for 10 sec.	0.049
4	Heated in $\text{HNO}$ for 2 hrs; Soaked in $\text{O}_2$ -sat. 1 N KOH for 20 min; Cathode in fuel cell $n=0.5$ for 30 sec.	0.048

surface. As cell operation began, this surface oxygen was depleted to a considerable extent. During the initial start-ups there were large surges of current, and the currents then quickly decayed toward a more-or-less steady-state value during the first several minutes of operation. The ESCA findings confirmed for the first time the direct relationship between adsorbed (or surface) oxygen and the large current fluxes previously noted during start-up by Roher et al. (5,6) and others (1-4). Information was obtained over wide ranges of conditions for the values of these high initial current surges. During the first several seconds of start-up, activation control is important. Then in the time period from about 20 to 120 seconds, diffusion of oxygen through the electrolyte solution is controlling (5,6). Although the ESCA results are preliminary, they indicate conclusively that ESCA is a valuable technique to be used in fuel cell investigations.

For so-called steady-state operation (after seven minutes of operation), the effects of concentration of electrolyte, temperature, and polarization were all investigated for both the platinum cathodes and the platinum anode. After about seven minutes, eddy diffusion currents seem to be important, and they account for most of oxygen transfer to the cathode and for most of the hydrogen transfer to the anode.

Optimum concentrations of electrolyte were found to occur for various operating conditions as shown in Table 2. At low concentrations of electrolyte as the concentration approached zero, the currents decreased toward zero; and as the concentration increased at higher concentrations, the currents also decreased. At an intermediate concentration, defined here as the optimum concentration, the current reached a maximum. These optimum concentrations occurred at higher values for the anode as compared to the cathode, at higher values for meniscus region (region near triple interface of electrolyte,



Table 2 Optimum Electrolyte Concentration at Constant Temperature\* and Indicated Polarizations

	ANODE		CATHODE	
	MENISCUS	SUBMERGED	MENISCUS	SUBMERGED
KOH	2.0 - 3.0 N (n = 0.6v)	0.45 N (n=0.1v) 0.35 N (n=0.8v)	1.5 - 2.0 N (n = 0.8v)	0.25 N (n = 0.8v)
H <sub>2</sub> SO <sub>4</sub>		1.0 N (n=0.4)		(n = 0.6v) 0.25 N (25°C) 0.4 N (80°C)

\* Temperature is 28°C unless otherwise indicated.

reacting gas, and electrode) as compared to submerged portion of electrode (region between electrode and electrolyte and relatively far from the meniscus), at slightly higher values at higher temperatures as compared to lower temperatures, and at slightly higher values at lower polarizations as compared to higher polarizations. Attempts are now in progress to determine which factors are responsible for the optimum concentrations and why these optimum concentrations change as operating conditions are varied. Factors that changed in these investigations included solubility and diffusivity of the reactant gases in the electrolyte, viscosity, surface tension, concentration of ions in the electrolyte, and reaction rate constants.

In a companion investigation (7), similar experimental information are also being determined for an electrolysis cell (to split water into hydrogen and oxygen). The results of this investigation are being employed for comparative purpose with those of the fuel cell. It is thought that available results will provide considerable insight into the mechanism of the fuel cell.

## Recent Results on Electrode Reaction Studies

Additional ESCA results have been obtained on the cathode of the fuel cell. These results are an extension of those in Table I. The objective of the additional work was to determine how the O 1s/Pt 4f peak area ratio varied when the cathode was rested after being used. During a rest period of two minutes, there were no significant changes in the peak area ratio values. Earlier findings had shown that this ratio was high during cell start-up with a recently activated platinum cathode. It is recommended that additional data be obtained in the future especially with longer rest periods. The earlier findings had suggested that oxygen adsorbed on the platinum surface was a reactant during cell start-up when large current fluxes occur.

Preliminary results have been obtained using phosphoric acid as the electrolyte. These results indicate the following optimum concentrations at 26<sup>0</sup> and 60<sup>0</sup>C temperatures.

TABLE III

	<u>Cathode</u>		<u>Anode</u>	
	26 <sup>0</sup> C	60 <sup>0</sup> C	26 <sup>0</sup> C	60 <sup>0</sup> C
Submerged	<0.5	0.5-1.0	0.5	0.5
Meniscus	>4.5	>4.0	>4.0	>4.0

Mr. Charles Bild has correlated his results, written his thesis, and passed his final master's oral examination.

Continued work is being planned to extend and develop suitable correlations and mechanistic models for the low-temperature hydrogen-oxygen fuel cell.

Literature Cited

1. Burton, J. R., "Phenomena in the Meniscus of the Cathode of the Hydrogen-Oxygen Fuel Cell in Potassium Hydroxide Electrolyte", M. S. Thesis, Purdue University (August 1975).
2. Cobb, J. T. and Albright, L. F., "The Effect of Peroxidation and Meniscus Shape of the Hydrogen-Platinum Anode of a Molten Carbonate Fuel Cell," J. Electrochemical Soc., 115, 2 (1968).
3. Davitt, H. J. and Albright, L. F., "Fuel Cell Oxidation of Hydrogen on Movable, Partially Submerged Platinum Anodes," J. Electrochemical Soc., 114, 531 (1967).
4. DeVet, J. O. Barile, R. G., and Albright, L. F., "Unsteady-state Phenomena on Oxygen Cathodes of Hydrogen-Oxygen Fuel Cells," J. Electrochemical Soc., 117, 417 (1970).
5. Rohrer, A. G., "Boundary Layer Replenishment and Unsteady-State Phenomena at the Cathode of a Hydrogen-Oxygen Fuel Cell," M.S. Thesis, Purdue University (August 1973).
6. Rohrer, A. G., Theofanous, T. G., and Albright, L. F., "Boundary Layer Replenishment and Unsteady-State Phenomena at the Cathode of a Hydrogen-Oxygen Fuel Cell", J. Electrochemical Soc. 123, 445 (1976).
7. Schaper, M. A., "Start-up Phenomena for the Cathode of an Electrolysis Cell", M. S. Thesis, Purdue University (December 1975).

## TASK III

ACOUSTIC SURFACE WAVE DEVICES  
FOR VISIBLE AND INFRARED IMAGING

Program Manager: R. L. Gunshor (317)493-9488

Project Scientists: R. F. Pierret (317)493-9487

H. W. Thompson (317)493-9497

R. Bray (317)493-9292



## SUMMARY

The objective of the research program described here is the development of a new group of solid state devices which employ the non-linear interaction between surface acoustic waves (SAW) and photo-generated charge carriers to achieve optical image scanning. Many of the findings of this effort are also directly applicable to the class of SAW non-linear devices employed in signal processing applications.

The objective of this final report is two-fold. Firstly we will present a review of the research performed under this contract; secondly we will present a brief summary of the performance achievements and expectations of the various SAW optical imaging schemes proposed thus far.

Three different types of devices have been studied under this contract. The first results reported employed a separate media configuration where a high-resistivity silicon wafer was separated by an airgap from a lithium niobate substrate. The second type of device reported was a monolithic device in which many of the disadvantages, both mechanical and electrical (biasing) of the separate media configuration were removed by performing all operations directly on a silicon wafer. The necessary piezoelectric activity is provided by a thin rf sputtered zinc oxide layer on the silicon. In the course of research on these monolithic devices a technique was developed for achieving a tremendous enhancement in photon detection sensitivity by using a pulsed bias supply. The third device type studied is a device again in the separate media configuration, but where the semiconductor continuum is replaced by a pn diode array. Optical image scanning has been reported using all three device configurations.

The experiments involving surface acoustic wave optical image scanning have been, in the case of the zinc oxide monolithic device, supplemented by studies of the zinc oxide structure itself. This approach was followed for two reasons. Firstly there was unexplained behavior observed in the course of optical image scanning experiments which could only be explained by a better understanding of the zinc oxide-SiO<sub>2</sub>-silicon sandwich. Secondly it is believed that in general, monolithic configurations for semiconductor interactive SAW devices are extremely promising. An attractive way to implement monolithic concepts is by means of zinc oxide films; therefore a basic study of the zinc oxide silicon configuration is important for a wide range of SAW imaging and signal processing applications.

The final section of this report will give a summary of SAW optical imaging performance to date, and must be interpreted in the light of the fact that new developments are constantly being performed in which a p-n diode array or a Schottky diode array is coupled to a lithium niobate substrate, resulting in optical imaging performance of greater resolution and sensitivity than has heretofore been obtained. Therefore it seems that the ultimate achievement of SAW image scanning has yet to be realized.

## INTRODUCTION

Surface Acoustic Wave (SAW) devices have found a wide range of applications in communications, radar, countermeasures, and electronic warfare systems. In numerous situations a relatively simple and inexpensive SAW device can replace bulky and costly electronic subsystems; in yet other instances heretofore unachievable performance is obtained, with a corresponding upgrading in system performance specifications. An especially attractive feature of SAW components is their ease of fabrication using conventional integrated circuit techniques.

More exotic than bandpass and dispersive filter applications, are the nonlinear signal processing devices resulting from the nonlinear interaction between surface acoustic waves and charge carriers in a semiconductor. System functions such as analog convolution, correlation with memory, and "fast" Fourier transforms are feasible using nonlinear SAW devices.

The work reported here represents an extension of SAW device operation to solid state optical image scanning. The initial work reported employed a separate medium configuration consisting of a silicon wafer mounted in close proximity ( $< 0.5\mu$ ) to a piezoelectric substrate ( $\text{LiNbO}_3$ ). Our subsequent effort has emphasized the elimination of the somewhat uncertain airgap by developing monolithic structures of piezoelectric  $\text{ZnO}$  films on oxidized silicon wafers. Device development has been supplemented by more basic studies of the electrical behavior and stability of the  $\text{ZnO-SiO}_2\text{-Si}$  layered configuration. Additional work has allowed the semiconductor continuum to be replaced by an array of pn diodes.

## A. SUMMARY OF PERFORMANCE CHARACTERISTICS OF SURFACE ACOUSTIC WAVE OPTICAL IMAGE SCANNING DEVICES

### 1. Sensitivity

The first SAW imaging devices envisioned were essentially majority carrier imaging devices. Thus it was envisioned that a device would be constructed to employ an acoustoelectric effect in which semiconductor carriers interact with a surface acoustic wave. Then when the semiconductor is illuminated, the interaction would be modified by the photo enhanced carrier density and this alteration would be detected along a propagation path -- thus a line imager could result. A major feature of such a scheme is the rapid scanning of the image and the lack of the need to fabricate a complex electrode structure. A drawback is that it is inherently less sensitive than other semiconductor imagers. The reason for this lack of sensitivity is because what is detected is an increase in majority carrier density above the equilibrium (dark) level.

There are two means that can be used to increase the sensitivity of SAW imagers. Firstly one can reduce the signal output corresponding to the charge carrier density in the dark. The second method is based upon devising a means for integrating the photogenerated carriers.

The integration scheme is inherent in competing solid state devices which are regarded as more sensitive. There is an obvious disadvantage to integration schemes; optical imaging devices employing integration are inherently slow.

The most recent work on surface acoustic wave optical image scanning has demonstrated techniques for obtaining photon integration and hence greatly enhanced sensitivity. These new techniques can be divided into

two categories. The first type of experiment involves using a semiconductor continuum in which the integration occurs in surface states. A more recent development involves surface acoustic wave devices where the semiconductor continuum is replaced by an array of diodes; the dimensional arrangement of the diodes is identical to those used for silicon videcon arrays.

Experiments employing a semiconductor continuum in a monolithic zinc oxide on silicon SAW device have been reported in previous contract reports. More recently we and other labs have experimented with diode arrays using a separate medium configuration wherein the diode array is separated by an airgap from an adjacent lithium niobate substrate. These imaging schemes that employ integration can achieve photosensitivities comparable to those obtained with competing solid state imaging devices. Of course one of the potential advantages of the SAW imager, that of speed, is sacrificed for increased sensitivity.

## 2. Resolution

The resolution capability of surface acoustic wave optical image scanning devices is basically limited by the same constraints as apply to alternative solid state line or area imaging devices. The primary limiting factors are diffusion of photogenerated carriers, bandwidth, and problems associated with the lateral transfer of charge along the surface.

The critical parameter influencing diffusion length is the carrier lifetime. This is variable from about one to 100 microseconds depending upon material preparation methods. Of course, the lifetime can be significantly reduced by doping with gold. At a lifetime of 10 microseconds the diffusion limited resolution is found to be of the order of 0.1 millimeter. To some extent the resolution problem can be alleviated by recourse to a diode array imaging device where the semiconductor continuum is replaced



by an array of p-n or Schottky diodes. Here a mesa configuration reduces the transverse diffusion effect, and a resolution of 80 microns is easily obtained. It is important to note that this is not the limit however, as the limiting resolution in this case is expected to be determined by the diode periodicity of 12 microns.

The present situation is that most existing surface acoustic wave imaging experiments have the resolution limited by bandwidth. Thus as an example, in the case of the convolver imager, the present resolution limit is due to the actual spatial extent of the "narrow" scanning pulse. For a pulse length of 0.1 mm in lithium niobate the transducer must launch a pulse of  $3 \times 10^{-8}$  seconds; this requires a bandwidth of about 30 MHz. A bandwidth of this order is feasible, but an order of magnitude increase would be difficult to achieve.

An additional factor affecting the resolution becomes important when at the same time one is attempting to optimize the sensitivity. For imaging employing majority carrier perturbation, it was found that the sensitivity was greater when the semiconductor surface was biased toward inversion than when biased just in the beginning of depletion. It was further observed that the resolution suffered when the semiconductor was biased into inversion. This reduction in resolution is believed due to a lateral motion of charge in the inversion layer. When the high sensitivity mode of operation is used, where a pulse bias is used to create a non-equilibrium situation to enhance the sensitivity, it is again found that by setting the constant bias into inversion the greatest sensitivity is obtained. Unfortunately, once again we obtained a blooming of the image due to the lateral transfer of charge in the inversion layer. Thus there seems to consistently be a trade-off between resolution and sensitivity.

### 3. Spectral Response

In the case of the separate medium configuration with the imaging produced by photogeneration on a semiconductor continuum, the spectral response of the imaging device is the same as for alternative semiconductor photo detectors employing silicon. When the separate medium configuration involves lithium niobate, one also must take into account the spectral response of the lithium niobate. Lithium niobate is essentially transparent from  $4\mu$  to  $4,000\text{\AA}$ . In the case of the monolithic surface acoustic wave imaging devices with zinc oxide on silicon, the spectral characteristics have not been measured. It is expected however that the zinc oxide will absorb very little photon radiation in the visible range. On the other hand it is likely that the rather large concentration of defect states will absorb readily in the infra-red.

### 4. Imaging with Diode Arrays

There are several modes of operation for SAW imagers employing semiconductor diode arrays. One of the most recent modes of operation involves means for first charging the diode array uniformly, then illuminating the diode array with a pattern of light such that the photogenerated carriers discharge the diode. A surface acoustic wave interaction then takes place to read out the varying depletion depths corresponding to the varying degrees to which the diode array is charged. This method results in a sensitive imaging device because we have a mechanism for integrating photons in a way analogous to the situation in a vidicon device.

### 5. Long Wavelength Imaging

The majority of work has emphasized the use of silicon because the surface properties of silicon are so well known and can be readily controlled

by standard techniques. However, both for device configurations employing a semiconductor continuum and also those using an array of Schottky diodes, in principle, experiments can be performed using other semiconductor materials. Of special interest would be semiconductors having energy gaps narrower than silicon; the result would be infra-red image scanners.

## B. RESEARCH PROGRAM

### 1. Second Harmonic Generation for Optical Imaging\*

Recently reported ASW optical image devices transform spatial variations in light intensity to a corresponding set of amplitude variations in time on an electrical signal. This is accomplished by coupling rf surface waves propagating on a piezoelectric substrate to an adjacent semiconductor medium; the light-perturbed surface charge density is spatially variant along the path of ASW propagation. Reported devices differ in the wave-particle interaction phenomenon employed to obtain the image. This report concerns ASW conversion of optical images with light enhancement of second harmonic generation as the wave-particle interaction mechanism. Similar in configuration to the device reported by Moll, et al.,<sup>1</sup> the device described here employs two contrapropagating surface waves to form the converted image signal. One pulse serves as the power source for harmonic generation while another higher power pulse imparts image information to the harmonic by local decoupling of the semiconductor-ASW interaction. The second harmonic and its copropagating fundamental source are referred to as reading signals; the higher power contrapropagating signal is termed a decoupling pulse.

The use of harmonic generation for optical imaging makes available the 40 db dynamic range associated with second harmonic generation of ASW in the presence of a semiconductor.<sup>2</sup> This effect portends a large harmonic signal amplitude variation for surface carrier density variations introduced by a given range of light intensity. In addition, unlike a device which is based on light-induced attenuation of the fundamental, output in the dark can approach zero.

\* (This work is reported in Applied Physics Letters, Vol. 25, 688, December 15, 1974.)

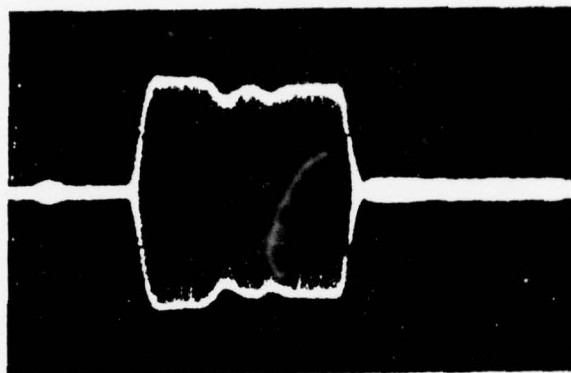


Fig. 1-1 Second harmonic image of two slits.



Figure 1-1 shows the image of two illuminated strips respectively 0.3 mm and 0.6 mm wide separated by 1.0 mm. The display is obtained using the second harmonic output scheme. The dimensions of strip widths and spacing correspond to two, four, and seven wavelengths at the fundamental frequency.

The level of illumination producing unity signal-to-noise ratio in the second harmonic output is found to be about 6 db below 1 mW/cm<sup>2</sup> at 6328 Å.

## 2. Convolution Imaging in a ZnO-SiO<sub>2</sub>-Si SAW Device\*

A monolithic SAW device consisting of an rf sputtered ZnO film on a thermally oxidized silicon substrate has been shown to be useful for several signal processing and optical image scanning applications.

The structure consists of a thermally oxidized silicon wafer onto which a 1.2 μm layer of oriented, polycrystalline ZnO has been deposited by rf sputtering. The transducers and convolver gate electrode are aluminum; the gate is made thin so as to be semi-transparent. The back of the silicon wafer is provided with an ohmic contact so that the dc surface potential of the silicon may be varied by biasing the gate. When the device is biased slightly into depletion, the convolution output, detected on the gate electrode at the second harmonic frequency maximizes. In addition, the applied negative bias causes electrons to be injected into the ZnO resulting in a shift in the effective bias point.

\* (This work is reported in Applied Physics Letters, Vol. 27, p. 179, 1975; Proceedings of the Ultrasonics Symposium, p. 141, 1975; Proceedings of the European Microwave Conference, p.235, 1976.)

Image scanning under dc bias conditions may be achieved by convolution. The convolver mode obtains when a long (essentially CW) pulse is convolved with a short scanning pulse. Imaging in the dc bias case is performed by using the structure with a gate voltage greater (more negative for n-Si) than is required for a maximum dark output. Subsequent illumination causes the local convolution efficiency to increase, allowing the pattern of light to be scanned by convolving a long and a short pulse. The sensitivity to light is based on a large injection situation; that is, a photon induced perturbation in the majority carrier concentration. The result is a very rapid scan imager with low sensitivity. A different mode of operation has been developed in which greater sensitivity is obtained at the sacrifice of speed; here an integration of photons occurs with a corresponding enhancement in sensitivity.

The pulse biasing scheme has been found to considerably enhance the light sensitivity. The device is initially biased with a dc voltage of about the same value as indicated above. Subsequently, a pulse is superposed on the dc voltage so that the bias is periodically pulsed from the dc bias point toward accumulation. The counterpropagating acoustic pulses are timed such that the convolution occurs at a time  $T$  after the bias pulse has turned off. By adjusting the value of  $T$ , the light to dark ratio can approach 40 db for an illumination of  $8 \times 10^{-3} \text{ mW/cm}^2$  of white light (tungsten-halogen lamp). This represents at least a 30 db improvement over the dc bias mode. In addition, it is found that if the initial dc bias is made more negative and  $T$  is made quite large, illumination intensities of  $5 \times 10^{-4} \text{ mW/cm}^2$  are detectable.

### 3. The ZnO-SiO<sub>2</sub>-Si Structure, An Electrical Analysis

The sputtered thin-film piezoelectric ZnO-thermally grown SiO<sub>2</sub>-Si structure provides a convenient and promising monolithic configuration for implementing SAW imaging and signal processing concepts. Results previously reported by our laboratories and other laboratories confirm the potential. It must be recognized, however, that it is the electrical properties of the ZnO-SiO<sub>2</sub>-Si sandwich itself which will ultimately determine the quality of characteristics derived from any SAW device fabricated with the ZnO-SiO<sub>2</sub>-Si sandwich. For this reason we have undertaken a study of the electrical properties of the sandwich.

Our preliminary results indicate:

- (1) The standard MOS-C analysis can be readily extended to include charge injection and thereby predict expected device characteristics.
- (2) As fabricated ZnO-SiO<sub>2</sub>-Si structures contain a relatively high density of fast surface states at the SiO<sub>2</sub>-Si interface.
- (3) It is highly probable that, following in-use fabrication procedures, the thermally grown SiO<sub>2</sub> layer is degraded leading to substrate-to-gate leakage currents through the SiO<sub>2</sub> layer.

### 4. Growth and Evaluation of Zinc Oxide Films

The rf diode sputtering system we have assembled consists primarily of commercially available components. The resulting films are extremely well-oriented and have a resistivity of at least  $10^9 \Omega\text{-cm}$ . The high resistivity is mainly due to the small crystallite size, about 100Å, which allows grain boundary states to compensate for the oxygen vacancies and zinc interstitials present within the individual crystallites. We have fabricated interdigital transducers on films such as these and have

found their performance to be typical of those reported in the literature. However, by improved transducer design and impedance matching, we expect the present efficiency to be greatly enhanced.

#### 5. Optical Image Scanning with a pn Diode Array

Earlier devices reported on this contract have interacted surface acoustic waves with photogenerated carriers in a semiconductor continuum. Later, we reported experiments on a separated medium configuration where the silicon wafer has an array of diffused pn junctions over its surface. These devices possess the ability to integrate photocarriers, and thus are potentially more sensitive than a continuum device operated with constant bias.

Image scanning is achieved using the convolution between a relatively long pulse and a second short pulse; in present experiments the devices have a resolution limited by the minimum spatial extent of the shorter pulse.

The diode array consists of p-type diffusions on 12.5 centers; the substrate is 10 ohm-cm silicon. The diode arrays were supplied by the Westinghouse Research Laboratory.

The resolution, although presently limited by the transducer bandwidth, could ultimately reduce to the order of the diode dimensions. The integration of photons, by the photo-discharging of pn diodes is achievable for enhanced sensitivity.